DESIGN, SIMULATION AND FABRICATION OF A MEMS BASED LEVITATED PLATFORM FOR LASER SCANNER APPLICATIONS

A THESIS SUBMITTED TO
THE GRADUATE SCHOOL OF NATURAL AND APPLIED SCIENCES
OF
MIDDLE EAST TECHNICAL UNIVERSITY

BY

ONURCAN KAYA

IN PARTIAL FULFILLMENT OF THE REQUIREMENTS
FOR
THE DEGREE OF MASTER OF SCIENCE
IN
MECHANICAL ENGINEERING

SEPTEMBER 2017

Approval of the thesis:

DESIGN, SIMULATION AND FABRICATION OF A MEMS BASED LEVITATED PLATFORM FOR LASER SCANNER APPLICATIONS

submitted by **ONURCAN KAYA** in partial fulfillment of the requirements for the degree of **Master of Science in Mechanical Engineering Department, Middle East Technical University** by,

Prof. Dr. Gülbin Dural Ünver
Dean, **Graduate School of Natural and Applied Science** _____

Prof. Dr. Sahir Arıkan
Head of Department, **Mechanical Eng.** _____

Assist. Prof. Dr. Kıvanç Azgın
Supervisor, **Mechanical Eng. Dept., METU** _____

Examining Committee Members:

Prof. Dr. Mehmet Çalışkan
Mechanical Eng. Dept., METU _____

Assist. Prof. Dr. Kıvanç Azgın
Mechanical Eng. Dept., METU _____

Assist. Prof. Dr. Ali Emre Turgut
Mechanical Eng. Dept., METU _____

Assist. Prof. Dr. Ulaş Yaman
Mechanical Eng. Dept., METU _____

Assist. Prof. Dr. Ender Yıldırım
Mechanical Eng. Dept., Çankaya University _____

Date: 22.09.2017

I hereby declare that all information in this document has been obtained and presented in accordance with academic rules and ethical conduct. I also declare that, as required by these rules and conduct, I have fully cited and referenced all material and results that are not original to this work.

Name, Last name : Onurcan Kaya

Signature :

ABSTRACT

DESIGN, SIMULATION AND FABRICATION OF A MEMS BASED LEVITATED PLATFORM FOR LASER SCANNER APPLICATIONS

Kaya, Onurcan

M.Sc., Department of Mechanical Engineering
Supervisor: Assist. Prof. Dr. Kıvanç Azgın

September 2017, 100 pages

This thesis presents design, simulation and fabrication of a MEMS based levitated platform for laser scanner applications. Electrostatic detection and actuation are utilized for levitation of the platform.

There are a number of laser scanners presented in the literature for several applications. All of the scanners in the literature are based on a mechanically suspended structure, which redirects a light source. Mechanical connection of those structures limits the maximum achievable scan range. This work represents a levitated platform for laser scanner applications. The main motivation behind the proposed structure is to achieve 360 degrees of scan range.

Designed structure consists of two stators and a rotor. There are sets of actuation and sense electrode structures defined on each stator. Mathematical models for actuation and detection mechanisms for levitation are derived. Equations of motion of the rotor

are obtained using mass-spring-damper model. Damping and stiffness acting on the rotor are modeled using squeeze film and slide film damping models. A capacitive readout circuitry is designed to convert rotor motion to voltage signals for each 5 axes.

To achieve stable levitation of the rotor, closed loop controllers are designed for each of 5 axes. For controller design, nonlinear and coupled equations of motions of rotor are decoupled and linearized around the nominal position of rotor. Following that, root locus design techniques are utilized to determine controller parameters. Since damping and stiffness acting on the rotor highly depends on ambient pressure, controllers are designed for both in air and in vacuum operation conditions. Robustness of designed controllers are verified by Simulink simulations, which utilizes nonlinear and coupled equations of motions. Noise generated by the controller and sense electronics are modeled. Equivalent voltage noise is calculated and its effect on position of rotor along 5 axes is discussed.

Fabrication of the proposed structure is performed. Stator structures are manufactured from a 6 layer Printed Circuit Board (PCB). Rotor, on the other hand, is fabricated using a SOI wafer. Rotor has a radius of 11300 μm and a thickness of 80 μm. Two stators are aligned with respect to each other by using bearing-balls with a diameter of 0.5 mm.

Keywords: MEMS, Laser Scanner, Electrostatic Levitation, Contactless Suspension, Capacitive Actuation, Capacitive Detection

ÖZ

LAZER TARAYICI UYGULAMARINA YÖNELİK MEMS TABANLI HAVALANDIRILMIŞ PLATFORMUN TASARIMI, SİMÜLASYONU VE ÜRETİMİ

Kaya, Onurcan

Yüksek Lisans, Makina Mühendisliği Bölümü
Tez Yöneticisi: Yrd. Doç. Dr. Kıvanç Azgın

Eylül 2017, 100 sayfa

Bu tezde lazer tarayıcı uygulamaları için MEMS tabanlı bir havalandırılmış platformun tasarımı, simülasyonları ve üretimi sunulmuştur. Platformun havalandırılması için elektrostatik algılama ve eyleme mekanizmaları kullanılmıştır.

Literatürde farklı uygulamalara yönelik çok sayıda lazer tarayıcı bulunmaktadır. Bu tarayıcıların tamamı, mekanik olarak asılmış, ışığa yön veren bir yapının pozisyonun kontrol edilmesine dayanmaktadır. Bu yapıların mekanik olarak bağlı olması tarayıcıların ulaşabildiği maksimum tarama açılarını sınırlandırmaktadır. Bu çalışma lazer tarayıcı uygulamalarına yönelik havalandırılmış bir platformu anlatmaktadır. Önerilen cihazın temelindeki motivasyon 360 derece tarama açısına sahip olmasıdır.

Tasarlanan yapı iki adet stator ve bir adet rotordan oluşmaktadır. Stator üzerinde algılama ve eyleme için tanımlanmış elektrot yapıları bulunmaktadır. Eyleyici ve

algılayıcı mekanizmaların matematiksel modelleri geliştirilmiştir. Rotorun 5 eksen üzerindeki hareketini modelleyen denklemler, kütle-yay-sönümleyici modeli kullanılarak sunulmuştur. Rotor üzerindeki damper ve yay etkileri sıkışan hava ve kayan hava modellerini kullanarak tanımlanmıştır. Rotorun 5 eksendeki hareketlerini voltaja çeviren kapasitif bir okuma devresi tasarlanmıştır.

Rotorun stabil olarak havalandırılması için kapalı döngü kontrolcüler tasarlanmıştır. Kontrolcü tasarlanması için doğrusal olmayan ve birbirleriyle bağımlı olan rotor hareket denklemleri bağımsız hale getirilmiş ve rotorun nominal konumu çevresinde doğrusallaştırılmıştır. Bunu takiben root locus yöntemi ile kontrolcü parametreleri belirlenmiştir. Rotor üzerindeki damper ve yay etkileri dış basınca bağlı olduğu için kontrolcüler hem atmosferik hem de vakum çalışma şartları için tasarlanmıştır. Tasarlanan kontrolcülerin çalışabilirliği, doğrusal olmayan ve bağımlı rotor hareket denklemleri kullanılarak oluşturulan Simulink simülasyonunda gösterilmiştir. Algılama ve kontrolcü devreleri için kullanılan elektronik bileşenlerin oluşturduğu gürültü modellenmiştir. Eşdeğer voltaj gürültüsü hesaplanıp, rotor pozisyonu üzerindeki etkisi sunulmuştur.

Önerilen yapının üretimi tamamlanmıştır. Stator yapıları 6 katmanlı devre kartından üretilmiştir. Rotor ise Silisyum üzeri yalıtkan (SOI) pul kullanılarak üretilmiştir. Rotorun yarıçapı 11300 μm ve rotorun kalınlığı 80 μm'dir. Üst ve alt statorlar birbirlerine 0.5 mm çapında toplar kullanılarak hizalanmıştır. Kapalı devre deneyler atmosferik koşullarda gerçekleştirilmiştir.

Anahtar Sözcükler: MEMS, Lazer Tarayıcı, Elektrostatik Havalandırma, Temassız Yataklama, Kapasitif Eyleme, Kapasitif Algılama

To

My Dear Parents, Sema & Sabır

My Sweet Sister, Öznur

ACKNOWLEDGMENTS

First of all I would like to thank my thesis supervisor Assist. Prof. Dr. Kıvanç Azgın not only for his help, guidance and support but also, for his friendly and optimistic attitude during my graduate studies. It is privilege for me working him.

I would like to thank to Orhan Akar, Dr. Akın Aydemir, Adem Saraç and Levent Abat for their help in Microfabrication processes and clean room trainings. I am also thankful to Serdar Hiçdurmaz not only for sharing his workstation with me for my Simulink simulations but also for his friendship.

Although I know that there is no way to express my gratitude, special thanks goes to Sedat Pala, for being great friend, for being a helpful lab partner and for endless discussions about life.

I also would like to thank all my METU Mechanical Engineering Department colleagues, Musab Çağrı Uğurlu, Uğur Kirazoğlu, Sinan Özgün Demir, Kerem Katılıoğlu, Ozan Kılıçkap, Ata Jafari, Tayfun Efe Ertop, Cihan Yıldırım, Anıl Kündeş and Ertuğ Şimşek for their support.

I would like to thank Scientific Research Projects (BAP) Coordination office by supporting this research.

Last but not least, I am very grateful to my mother, Sema, my father, Sabır and my sweet sister Öznur for their endless love, support and encouragement throughout my life.

TABLE OF CONTENTS

LIST OF TABLES

TABLES

LIST OF FIGURES

FIGURES

CHAPTER 1

INTRODUCTION

In today's technology, key factor, which leads existence of smart devices, that can sense and interact with the environment and transform them to everyday use devices is miniaturization. Thanks to miniaturization, a computer, which takes a full room of space, turned into a device, which can be carried in a pocket. Miniaturization, not only made things smaller but also cheaper and more energy efficient.

Origin of the miniaturization dates back to invention of the first transistor in 1947. Since then, thanks to advances in integrated circuit (IC) fabrication techniques, size of a transistor gets smaller and smaller. As a result density of transistor in a chip has been increasing according to Moore's Law [1].

Experience gained on IC fabrication techniques leads to born of the field of Micro Electro Mechanical Systems (MEMS), which combines the micro-sized mechanical structures and electronics on the same substrate. In 1982, silicon is utilized as a mechanical material [2]. This leads to surface micro machined mechanisms including springs, gear trains and cranks [3]. From that point on, application of MEMS based devices have gained great diversity, ranging from pressure sensors to cancer cell detection, thermal actuators to micro motors, infrared detectors to time keeping devices.

This chapter consists of 3 sections. In section 1.1, mechanisms for contactless suspension are discussed and its application on MEMS based devices is explained with several examples found in literature. Secondly, in section 2.2 laser scanners

found in literature are represented. Finally, objectives of the study and organization of the thesis are represented.

1.1 Contactless Suspension

Human imagination is so deeply acquainted with the phenomenon of gravity that everything which appears in the state of free suspension emanates an air of marvel [4]. Therefore, people have great interest in levitation of objects and suspend them without any contact. For levitation, one should generate forces to overcome gravity and those forces should be transmitted to the body without any physical contact. In nature, there are several invisible force transmission mechanisms, such as electrostatic force transmission and magnetic force transmission etc.

The existence of electrostatic levitation traces back to Millikan's oil droplet suspension in 1910 [5]. In 1959 it is realized levitation of charged particles about several microns without feedback control. Finally, in 1984 an active controlled electrostatic levitator is established and a facility for high temperature containerless materials processing was developed in 1993. Magnetic levitation, on the other hand, is first achieved and patented by Emile Bachalet in 1912 [6].

In literature, electrostatic levitation [7-12], magnetic levitation [13-18] or combinations of them [19, 20] are used in several sensor and actuator applications. Magnetic and electrostatic levitation principles have some advantages and drawbacks with respect to each other. Large forces and displacement can be generated by magnetic actuation compared to electrostatic actuation [3]. Moreover, in magnetic actuation, both attractive and repulsive forces can be generated from a single structure, which reduces the control effort for stabilization. However, for magnetic actuation heat generation due to high current passing from coils might be a problem depending on the application. Electrostatic levitation, on the other hand, stators are typically planar structures, which provides better miniaturization [21].

Performances of MEMS based sensors are improved with the utilization of levitation principles. For example, thanks to levitation micro motors have longer lifetime. In

[22], common failure modes for a micro motor application are listed as, friction, wear, fracture, contamination, stiction and electrostatic interface. As rotor is levitated, two of the factors, which limit the lifetime of micro motors, are eliminated. Another device, whose performance is boasted by levitation, is gyroscope. The gyroscope proposed in [23], which is used in Gravity Probe-B of NASA, has the highest angular resolution and it is based on a levitated rotor. In [17], it is stated for a MEMS based vibrating gyroscope, it is really challenging to improve bias instability beyond sub-degree/hour due to quadrature error caused by device asymmetry and unbalance. However, utilization of contactless suspension in MEMS based gyroscopes, has potential to obtain a resolution value similar to [23]. Due to having such possible applications and providing such improvements levitation becomes an appealing research topic.

1.2 Laser Scanner

Laser scanning is controlling of deflection of laser beam and direct it to desired points. MEMS based laser scanners are utilized in many applications, such optical switching [24], confocal laser scanning microscope [25], retinal scanning display and imagining [26], endoscopic optical coherence tomography [27] and light detection and ranging (LIDAR) [28-30].

Most of the laser scanners found in the literature are micro-mirror based scanners. Some of those scanners are driven electromagnetically [24-26, 29], while some of them are driven electrostatically [27, 28, 30]. In addition to those actuation mechanisms, an electrothermal laser scanner is also found in literature [31]. Among those actuation techniques, scanning range provided by electrostatic actuation is small and requires larger drive voltages. Electrothermal and electromagnetic actuations overcome that problem. Drawbacks of electrothermal and electromagnetic, on the other hand, are nonlinear behavior of mechanical properties and big size due to external magnetic filed, respectively [32]. Other than micro mirror based scanners, micro-lens based scanners are also present [33].

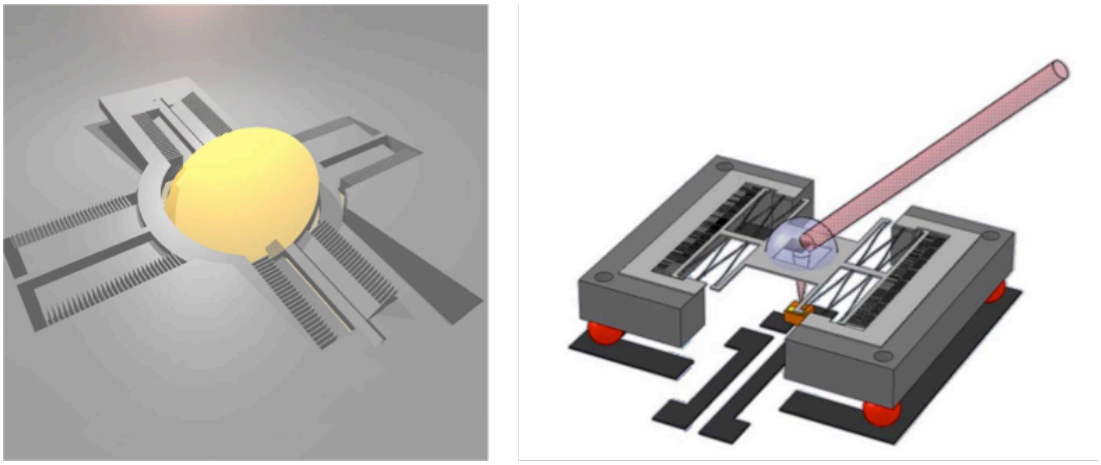

(a) (b)

Figure 1 (a) Micro mirror based laser scanner [30], (b) Micro lens based laser scanner [33]

Available scanners in the literature, provides several scanning ranges with different driving mechanisms. The proposed scanner in [26] is a micro mirror based 2D scanner, which is actuated magnetically. Obtained scanning ranges are reported as 65^{o} and 53^{o} for each axis. Moreover, it is stated that utilization of magnetic actuation, provides sufficiently large forces for non-resonant operation. The proposed scanner in [34], on the other hand is a resonant actuated 2 axis micro-mirror based scanner. Required forces for the rotation of the mirror about two axes are generated by comb fingers, electrostatically. The scanner is hermetically sealed on wafer level and maximum scan amplitude of +/- 27 degrees has been obtained.

As explained above, laser scanners available in literature, have different drive mechanisms and provide several scan range. However, they have one property in common; all of the existing scanners in the literature are mechanically suspended. Therefore, it is not possible to increase the scan range after a point, by using a rotating mirror only. As a solution to that limitation, in [30], an omnidirectional lens is designed around the micro-mirror scanner proposed in [34] and scanning range is increased up 250 degrees.

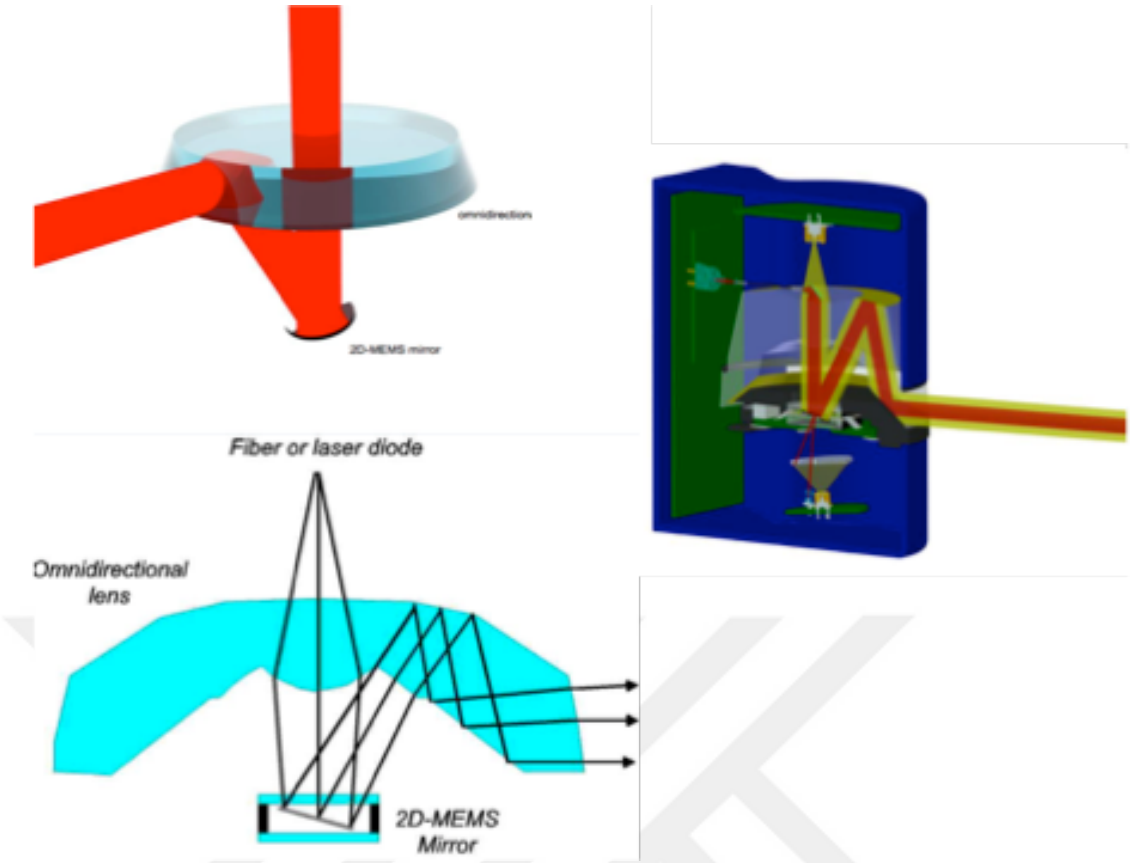

Figure 2 Micro mirror based scanner with an omnidirectional lens

1.3 Research Objectives and Thesis Organization

As explained in Section 1.2, MEMS based laser scanners have several applications. However, due to mechanical constraints, scan range is limited. Researches tried to overcome mechanical limitation by using complex lens structure around a rotating mirror and achieve scan ranges up to 250 degrees. Nevertheless, a full 360 degrees of scan range without any dead zone cannot be achieved in the literature. In the scope of that study, a levitated MEMS based platform for laser scanner applications, which can achieve 360 degrees of scan range is designed. Designed device consists of a rotor that is sandwiched between two stators. Rotor is manufactured from Silicon on Glass (SOI) wafer, while stator structures are manufactured from Printed Circuit Boards (PCBs). Rotor position between stators is sensed and required forces to achieve stable hovering are generated electrostatically. The specific aims of that study are listed below.

- Investigation of voltage of a floating object and required conditions to generate vertical forces. Following that, utilize that condition to design a stator structure.

- Derive analytical expressions that relate rotor motion and change of capacitances, which are created between stator electrodes and rotor. Then utilize those expressions to calculate actuation forces along each axis.

- Design readout circuits that utilize change of stator electrode capacitances to detect the position of rotor along each axis. Following that, derive a transfer function that relates rotor motion and detection signal.

- Design a controller to maintain stability for each axis considering the air and vacuum operation of the device. Following that, perform closed loop simulations to test the designed controllers.

- Perform the fabrication of the device.

Main structure of the thesis is represented below:

In Chapter 2, voltage of a floating object is examined and required electrode configuration in order to generate vertical forces is investigated. Following that, designed device is explained along with its working principle. Then mathematical model for the proposed device, including rotor-stator capacitances, electrostatic actuation and rotor dynamics, which includes squeeze film and slide film damping models are derived. After that in the following subsection, a readout circuitry and its mathematical model are developed in order to detect rotor position between stators.

In Chapter 3, controller design procedure for the motions of the rotor along 5 axes is represented. Controllers are designed for the operations of device in atmospheric and vacuum conditions. Then in the next subsection, closed loop simulations in atmospheric and vacuum conditions are performed using Matlab Simulink and obtained results are represented. Finally, noises induced by sense &

controller electronics are calculated and their effects on the position of the rotor are analyzed.

In Chapter 4, fabrication of the proposed device is explained. Firstly, manufacturing of stator structure from printed circuit board is discussed. Following that, fabrication of rotor structure along with the micro fabrication flow is presented.

Finally in Chapter 5, conclusions derived from the obtained results are represented and future works to improve the proposed device are discussed.

CHAPTER 2

DESIGN AND MODELLING OF MEMS BASED LASER SCANNER

In this chapter, design and modeling of the proposed sensor structure is presented. In Section 2.1, basic concepts in electrostatic levitation are discussed. Starting from definition of parallel plate capacitor, voltage expression for a floating object is derived and necessary electrode structure to ensure levitation is explained. In Section 2.2, proposed levitated platform and its application as a laser scanner is discussed in detail. After that, components of the proposed device, i.e. rotor and stator structures defined. Electrode structures, which are defined on top and bottom stator, are explained in detail. Capacitances formed between rotor and each stator electrode are defined. Then their utilization as a sense and actuator electrode is discussed. Finally in that section geometric parameters of the proposed device is tabulated. In Section 2.3, changes of formed capacitances as a result of motion of the rotor along 5 axes are modeled. Following that, derived capacitance models are utilized to obtain force expressions generated by each electrode, along 5 axes. Then damping and stiffness acting on the rotor is modeled, overall force acting on the rotor on each axis is represented and equations of motion of the rotor along 5 axes are given. In Section 2.3, capacitive detection mechanisms for each axis along with their reading circuit is discussed and modeled. Finally, in section 2.4, summary of the section is presented.

2.1 Basic Concepts in Electrostatic Levitation

In that application an object called rotor, is elevated to air without any mechanical contact and it hovers around an equilibrium point. To hover the rotor one should

overcome gravity and should apply forces on rotor. To maintain rotor stability as it is elevated, position of the rotor in all 6 axis need to be controlled. In the scope of that thesis, all forces are generated and all measurements are done electrostatically, based on parallel plate capacitor. Capacitance of a parallel plate capacitor is simply defined by

$$C = \frac{\varepsilon A}{d} \tag{2.1}$$

where, ε is electric permittivity, A is overlap area between parallel plates and d is distance between parallel plates.

The value of the capacitance given in (2.1), changes either when plates move to each other along their normal directions which corresponds to change of d, or when plates translate with respect to each other, which corresponds to change of A. Both of those mechanisms are used to detect the position of the rotor for levitation.

When a differential voltage is applied between two parallel plates an electrostatic force will develop whose magnitude equals to gradient of the stored electric energy, U, with respect to dimensional variable of interest, η [3]. The expression for the magnitude of the force is

$$F = \left|\frac{\partial U}{\partial \eta}\right| = \frac{1}{2}\left|\frac{\partial C}{\partial \eta}\right| V^2 \tag{2.2}$$

For levitation, rotor is sandwiched between two plates, which contains set of electrodes. If the levitation problem is simplified into movement of rotor along its vertical axis only, rotor can be elevated by applying proper potentials to top and bottom electrodes. Simplified levitation configuration and its electrostatic model are given in Figure 3 below.

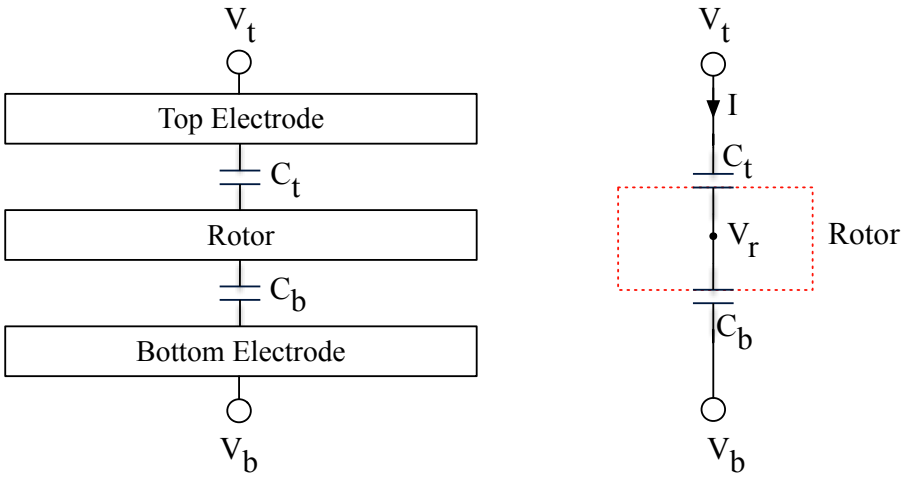

Figure 3 Simplified levitation configuration and its electrostatic model

As mentioned in the previous paragraph, electrostatic force will be generated when a differential voltage is applied between two parallel plates. Therefore, it is crucial to know to potential of each plate. Potential of the top and bottom electrodes can be measured easily. However, since elevated rotor has no mechanical contact, it is not trivial to know the potential of the levitated object. According to [21] and using the electrostatic model given in Figure 3 electric potential of the rotor can be derived as

$$V_t - V_r = \frac{I}{C_t s} \tag{2.3}$$

$$V_r - V_b = \frac{I}{C_b s} \tag{2.4}$$

where, V_t, V_r, V_b are electric potential of top electrode, rotor, bottom electrode respectively, C_t, C_b are capacitance formed between top electrode-rotor, bottom electrode-rotor respectively and I is current flowing through the capacitors By combining (2.3) and (2.4) electric potential of the rotor can be obtained as

$$V_r = \frac{V_t C_t + V_b C_b}{C_t + C_b} \tag{2.5}$$

From equation (2.5), it can be seen that electrical potential of rotor is depends on the both electric potential of electrodes and formed capacitances between rotor and

electrodes, i.e. position of the rotor between electrodes. Moreover, when rotor is at the middle of the electrode pairs, top and bottom capacitances, i.e. C_t and C_b are equal. At that point, according to equation (2.5), potential difference between top electrode & rotor and bottom electrode & rotor are the same and it is,

$$\left|V_t - V_r\right| = \left|V_r - V_b\right| = \frac{V_t - V_b}{2} \tag{2.6}$$

which means, electrostatic forces that are generated by top electrode on rotor and bottom electrode on rotor are equal to each other. Therefore, net electrostatic force acting on the rotor is zero, for that case.

To solve that problem, electrodes that generate force on the rotor divided into two equal pairs and voltage applied to those pairs at different polarity. Related configuration is shown in Figure 4 below.

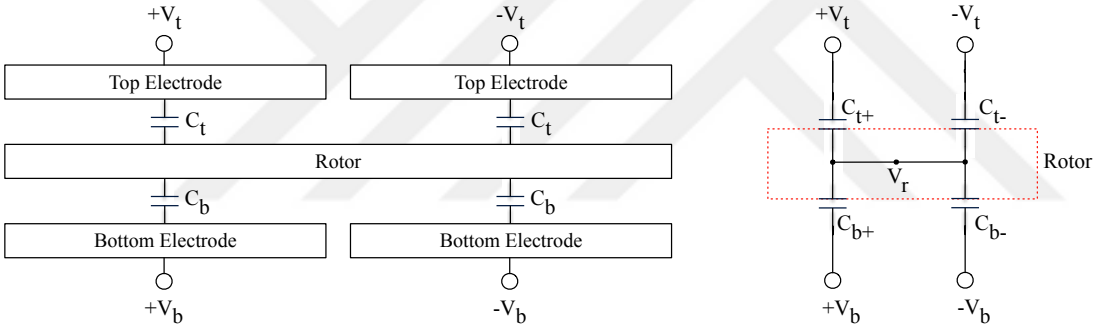

Figure 4 Simplified levitation configuration for paired electrodes and its electrostatic model

Using the same procedure, rotor voltage is obtained as

$$V_r = \frac{V_t\left(C_{t+} - C_{t-}\right) + V_b\left(C_{b+} - C_{b-}\right)}{C_{t+} + C_{t-} + C_{b+} + C_{b-}} \tag{2.7}$$

ßAs long as rotor is parallel with respect to electrodes, C_{t+} & C_{t-} and C_{b+} & C_{b-} are equal to each other. Therefore, from (2.7) it can be concluded that rotor is maintained at 0 V as long as its parallel to electrodes.

2.2 MEMS Based Laser Scanner

As explained in Chapter 1, laser scanners are utilized in several applications. As it is discussed in Section 1.2, due to mechanical constraints it is not possible to increase the scan range after a certain point. Although scan range of 250 degrees is obtained by using an omnidirectional lens, a laser scanner, which offers a scan range of 360 degrees does not present in the literature. In the scope of that thesis, a levitated platform for laser scanner applications, which has 360 degrees of scan range, is developed.

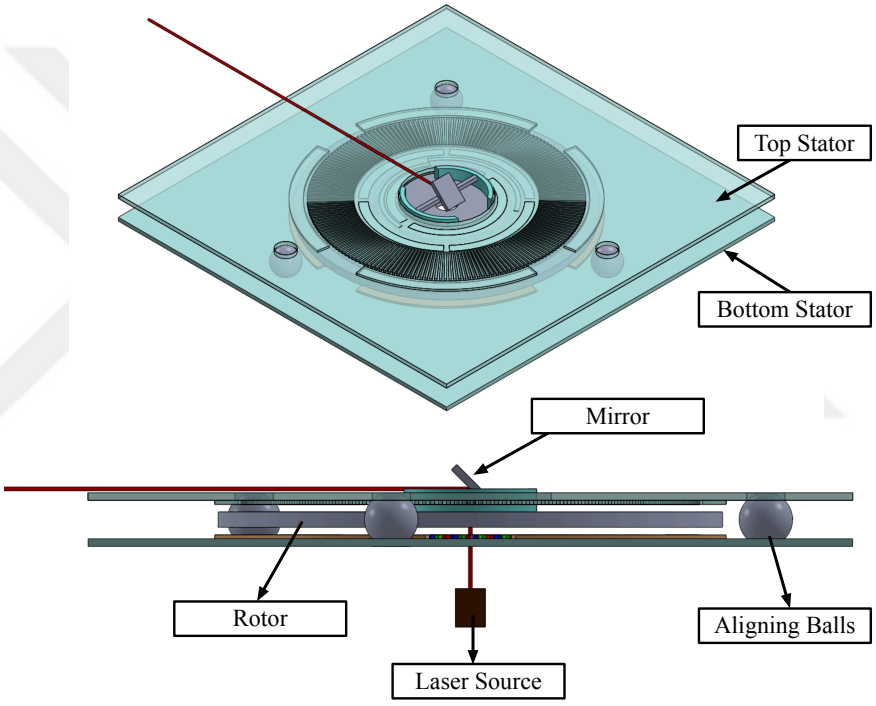

Figure 5 3D model of laser scanner

3D model of the proposed laser scanner is given in the Figure 5. The laser scanner consists of a levitated platform called rotor, and two stators. Rotor, which carries a mirror, is placed between two stators and it is levitated electrostatically. Top and bottom stator structures are aligned to each other from 3 points using balls. Laser is directed to rotor from the bottom of the structure and it is reflected from mirror to the

horizontal plane. As rotor rotates about its normal axis, laser is directed to any angle on horizontal plane, which makes 360^{o} of scanning possible.

2.2.1 Actuation and Sense Mechanisms

As mentioned previously, motion of the rotor on six axes both actuated and sensed, i.e. controlled electrostatically. For control of the motion on each axis, there are dedicated structures both on the rotor and stators.

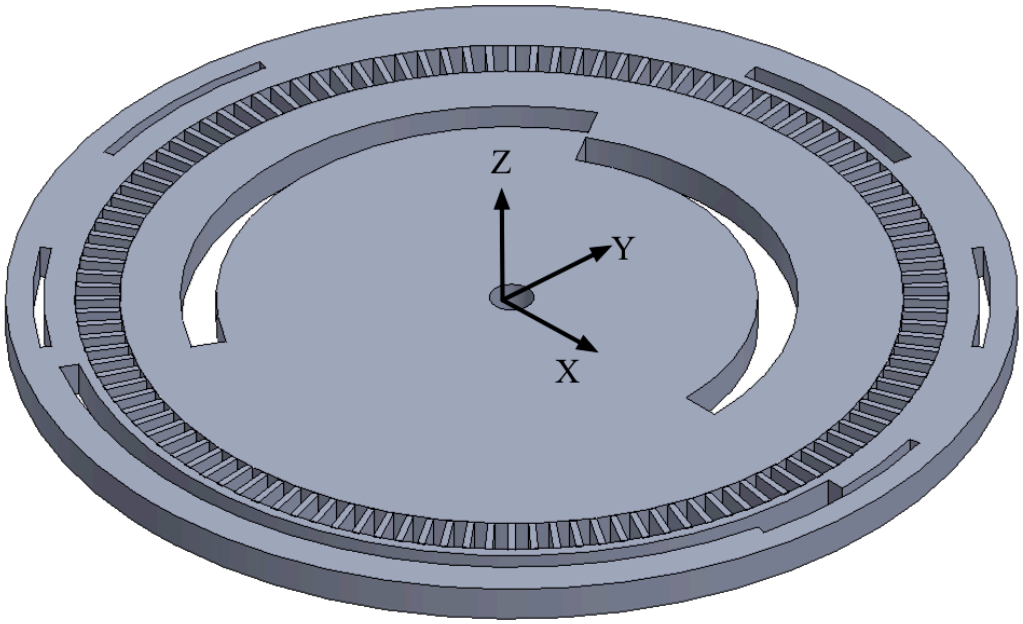

Figure 6 3D Model of rotor and attached coordinate frame

Detailed view of the rotor structure is shown in Figure 6 above. There is a hole at the center of the rotor for laser beam. 120° arc shaped slots around the hole are used to sense the rotational position of the rotor about z-axis. There is a grill structure at the periphery of the rotor. Each pie shaped area in that structure is called as a pole and they are used to generate required torque for rotation of the rotor about z-axis. Finally, there are slots surrounding the rotor poles in order to carry the center of gravity of the rotor to rotor's geometric center and in order to balance the principle moment of inertia of the rotor about x and y axes.

Stator structure on the other hand, consists of set of electrodes to levitate the rotor electrostatically. Detailed view of a stator structure is represented in Figure 7 below. As it can be seen, to ensure the stability of the rotor in 6 degrees of freedom, there are mainly 6 sets of electrodes, namely levitation electrodes, out of plane rotation electrodes, translational motion electrodes, rotational motion actuation, rotational motion sense and carrier electrodes. Among those electrodes, carrier electrode pair is used to generate measurement signals, which are used to detect the position of the rotor.

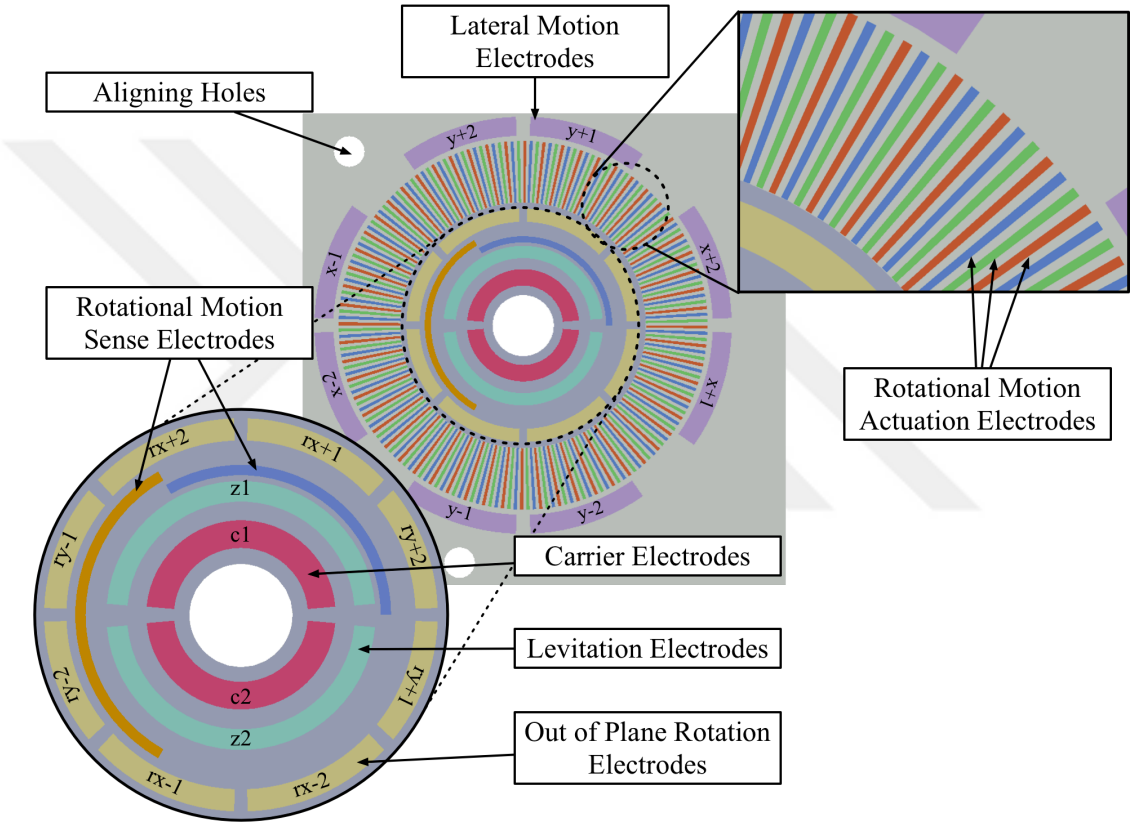

Figure 7 Detailed view of a stator

Capacitances are built up between the rotor and stator electrodes. Formed capacitances between bottom stator and rotor are shown in Figure 8 below. C_{c1b} and C_{c2b} are the capacitances between bottom stator carrier electrodes and rotor. C_{z1b} and C_{z2b} are the capacitances that built up between bottom stator levitation electrodes and rotor. C_{rx+1b}, C_{rx+2b}, C_{rx-1b}, C_{rx-2b}, C_{ry+1b}, C_{ry+2b}, C_{ry-1b} and C_{ry-2b} are the capacitances generated between bottom out of plane rotation electrodes and rotor. Finally, C_{x1+b},

C_{x+2b}, C_{x-1b}, C_{x-2b}, C_{y+1b}, C_{y+2b}, C_{y-1b} and C_{y-2b} are the capacitances between rotor and translational motion electrodes. Those capacitances are coupled with the capacitances formed between top stator electrodes and rotor i.e. C_{c1t}, C_{c2t} (formed between top stator carrier electrodes and rotor), C_{z1t}, C_{z2t} (formed between top stator levitation electrodes and rotor), C_{rx+1t}, C_{rx+2t}, C_{rx-1t}, C_{rx-2t}, C_{ry+1t}, C_{ry+2t}, C_{ry-1t}, C_{ry-2t} (formed between top stator out of plane rotation electrodes and rotor), C_{x1+t}, C_{x+2t}, C_{x-1t}, C_{x-2t}, C_{y+1t}, C_{y+2t}, C_{y-1t} and C_{y-2t} (formed between top stator translational motion electrodes and rotor.)

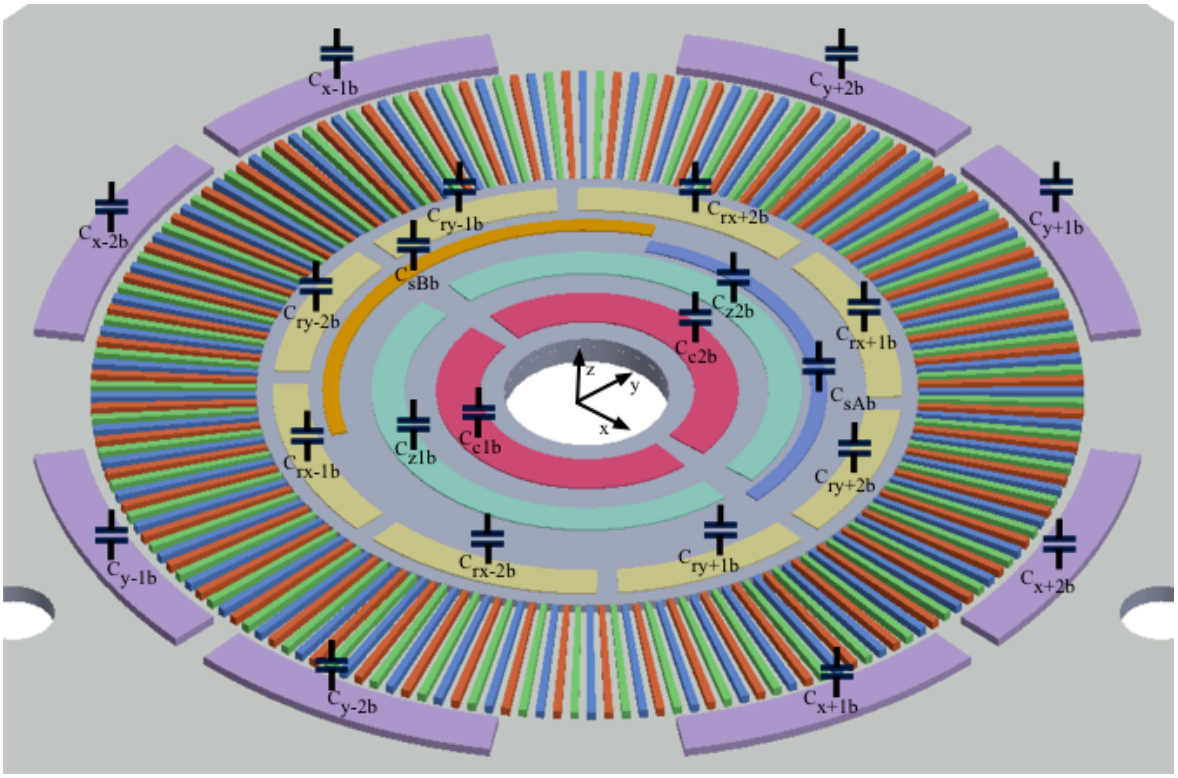

Figure 8 Formed capacitances between bottom stator and rotor

2.2.1.1 Actuation

As given in equation (2.2) when a differential voltage is applied to an electrode an electrostatic force is generated. For that application there are dedicated electrode structures to generate forces for each axes. For motion of the rotor along z axis, there are two levitation electrodes on each stator. In order to generate rotational forces about x and y axes, out of plane rotation electrodes labeled as rx+1, rx+2, rx-1, rx-2

and ry+1, ry+2, ry-1, ry-2 are used respectively. Those electrodes are also used to generate forces along z direction. For lateral motion of rotor along x and y axes, translational motion electrodes labeled as x+1, x+2, x-1, x-2 and y+1, y+2, y-1, y-2 are used respectively. Finally, rotational actuation of the rotor about z axis is assured using rotational actuation electrodes.

In order to generate out of plane forces on rotor, i.e. force along z direction, torque about x and y axes, change of capacitance due to nominal gap is utilized. In plane actuation of rotor, on the other hand, is based on fringing fields existing due to misaligned electrodes.

For rotational actuation of rotor, stator rotational actuation electrodes are divided into three phases each of which contains 60 electrodes. In total there are 180 equally spaced rotational actuation electrodes on each stator, while there are equally spaced 120 poles on rotor. The surface area of each pole and electrode are equal. The actuation mechanism is represented in Figure 9. Each color on the stator (red, green and blue) represents a phase. The orange marker next to stator phase electrode represents the active phase electrode set.

In Figure 9(a), red phase electrodes, which have misaligned rotor poles, are excited. This leads alignment of half of rotor poles with red phase electrodes. At that point remaining half of the rotor poles are misaligned with blue and green stator phase electrodes as represented in Figure 9(b). Depending on desired direction of rotation, one of those stator phase electrodes, i.e. blue or green is activated. For the case given in Figure 9, blue phase electrodes are activated and as a result half of the rotor poles become aligned with blue phase electrodes (See Figure 9(c)). By exciting stator phase electrodes in that manner, rotation of the rotor about z-axis is assured.

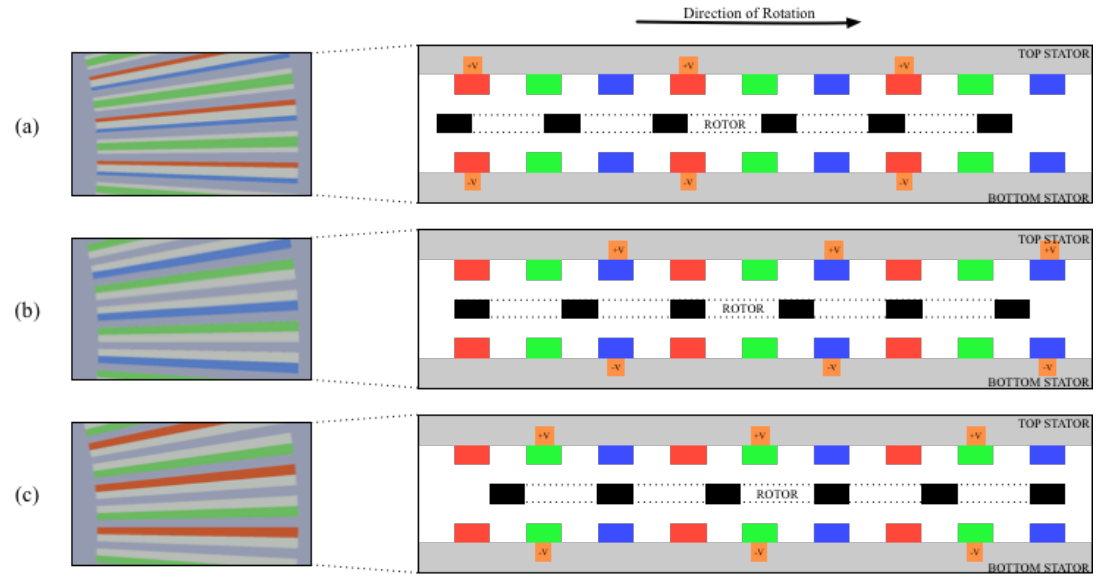

Figure 9 Actuation mechanism of rotation of rotor about z axis

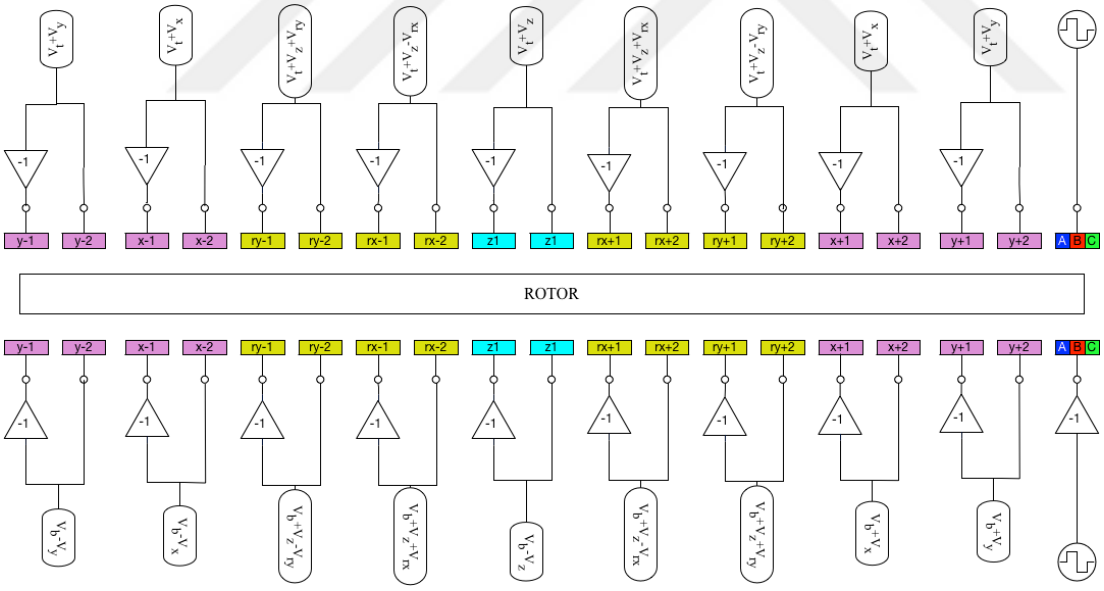

Figure 10 Schematic of electrode configuration for actuation

Figure 10 shows simplified schematics of actuation electrode configuration. V_x, V_y, V_z, V_{rx}, V_{ry} and V_{rz} are controller outputs to control translation of rotor along x, y, z axes and rotation rotor about x, y axes respectively. Those control voltages are

superimposed onto bias voltages, V_b and V_t as shown in Figure 10. For rotation of the rotor about z-axis, on the other hand, a PWM signal is applied to each phase group of rotational motion actuation electrodes. High/low time of the PWM signals are set according to misaligned rotor poles and stator electrodes, as explained in the previous paragraph. As explained in Section 2.1, all control voltages are applied in opposite polarity to electrode pairs in each direction, to keep rotor at 0 V.

2.2.1.2 Sense

In order to sense the position of the rotor, formed capacitances between rotor and stators are utilized. Values of those capacitances changes as rotor moves either due to change of nominal gap or change of overlapped area. By tracking that change position of the rotor on each 6 axes are sensed.

To sense the position of the rotor along z axis, capacitances formed between rotor and levitation electrodes i.e., C_{z1b}, C_{z2b}, C_{z1t} and C_{z2t}, are used. As rotor moves in z direction, gap between stators and rotor changes, which results change in those capacitances. In order to strenghten the sense signal, those capacitances are used in a differential reading configuration as shown below.

$$\Delta C_z = \left(C_{z1b} + C_{z2b}\right) - \left(C_{z1t} + C_{z2t}\right) \tag{2.8}$$

To sense the rotation of rotor about x axis, capacitances formed between x out of plane rotation electrodes and rotor i.e. C_{rx+1b}, C_{rx+2b}, C_{rx-1b}, $C_{rx-2b,}$ C_{rx+1t}, C_{rx+2t}, C_{rx-1t}, C_{rx-2t} are used. As rotor rotates about x axis, values of those capacitances changes due to change of nominal gap. Those capacitances are configured as

$$\Delta C_{rx} = \left(C_{rx-1b} + C_{rx-2b} + C_{rx+1t} + C_{rx+2t}\right) - \left(C_{rx+1b} + C_{rx+2b} + C_{rx-1t} + C_{rx-2t}\right) \tag{2.9}$$

Angular position of rotor with respect to x axis is measured, by monitoring the value of ΔC_{rx}.

For y axis rotational motion, capacitances formed between y out of plane electrodes, namely C_{ry+1b}, C_{ry+2b}, C_{ry-1b}, C_{ry-2b}, C_{ry+1b}, C_{ry+2t}, C_{ry-1t}, and C_{ry-2t} are utilezed in a similar manner as shown in equation (2.10) below.

$$\Delta C_{ry} = \left(C_{ry-1b} + C_{ry-2b} + C_{ry+1t} + C_{ry+2t}\right) - \left(C_{ry+1b} + C_{ry+2b} + C_{ry-1t} + C_{ry-2t}\right) \quad (2.10)$$

For translational motion of rotor along x axis, capacitances bulit up between x translational motion electrodes and rotor, i.e. C_{x+1b}, C_{x+2b}, $C_{x-1b,}$ C_{x-2b}, C_{x+1t}, C_{x+2t}, $C_{x-1t,}$ and C_{x-2t} are used. As rotor moves on x axis, overlap area between x translation electrodes and rotor changes, which results a increase/decrease in those capacitance values. Those capacitances are combined as shown in (2.11) below and a single sense capacitance ΔC_x is obtained.

$$\Delta C_x = \left(C_{x+b} + C_{x+t}\right) - \left(C_{x-b} + C_{x-t}\right) \quad (2.11)$$

To sense the position of the rotor along y axis, capacitances formed between y translational motion electrodes and rotor, namely C_{y+1b}, C_{y+2b}, $C_{y-1b,}$ C_{y-2b}, C_{y+1t}, C_{y+2t}, $C_{y-1t,}$ and C_{y-2t} are used in a similar manner as shown in equation (2.12).

$$\Delta C_y = \left(C_{y+b} + C_{y+t}\right) - \left(C_{y-b} + C_{y-t}\right) \quad (2.12)$$

Up to that point, for actuation and sense, same electrode pairs are used. However, for rotation of the rotor about z axis there are dedicated sense electrodes. To measure the angular position of the rotor about z axis, there are two 120° arc shaped rotational motion sense electrodes. Bottom rotational sense electrodes forms capacitances C_{sAb} and C_{sBb} with rotor as shown in Figure 8. Thanks to asymmetric sense slots on rotor, change of capacitances C_{sAb} and C_{sBb} form unique detection signals, which do not resemble each other during the full rotation of rotor as shown in Figure 11. By using those two signals absolute position of the rotor is determined.

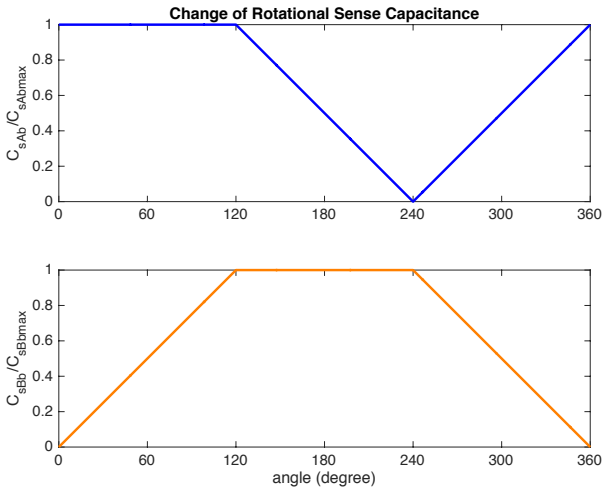

Figure 11 Rotational sense capacitances

2.2.2 Physical Structure of the MEMS based Levitated Platform

As defined previously, there are 2 carrier electrodes, 2 levitation electrodes, 2 rotational motion sense electrodes, 8 out of plane rotation electrodes, 8 translation electrodes and 180 rotational actuation motion electrodes located on each stator. Geometrical dimensions of each electrode are defined by using the convention given in the figure below.

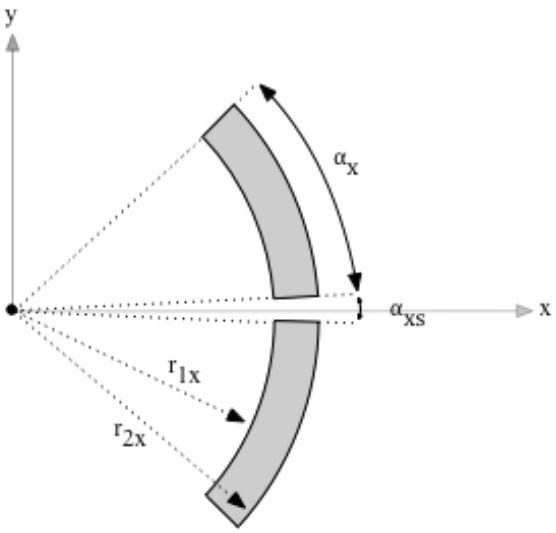

Figure 12 Convention to define geometrical properties of electrodes

In Figure 12, sector angle of an electrode is denoted by α_x and angular spacing between each set of electrode is denoted by α_{xs}. Inner and outer radii of each electrode are denoted by r_{1x} and r_{2x}. The last subscript 'x' in those notions, represents the electrode set in interest. (-c, carrier electrodes, -z, levitation electrodes; -op, out of plane motion electrodes; -l, lateral motion electrodes; -A, rotational sense A electrode; -B, rotational sense B electrode)

Geometric and physical parameters of the proposed device are listed below.

Table 1 Geometric and physical properties of rotor and stator structures

Quantity	**Symbol**	**Value**
Rotor radius	r_r	11300 μm
Rotor thickness	t	80 μm
Mass of the rotor*	m	59.27 μg
Inertia of the rotor about x axis*	I_{xx}	1820.7 μg m^2
Inertia of the rotor about y axis*	I_{yy}	1820.7 μg m^2
Nominal gap between rotor and a stator	d	20 μm
Inner radius of a carrier electrode	r_{1c}	2800 μm
Outer radius of a carrier electrode	r_{2c}	3600 μm
Sector angle of a carrier electrode	α_c	176^o
Angular spacing between carrier electrodes	α_{cs}	4^o
Number of carrier electrodes	–	2
Inner radius of a levitation electrode	r_{1z}	3800 μm
Outer radius of a levitation electrode	r_{2z}	5300 μm
Sector angle of a levitation electrode	α_z	176^o
Angular spacing between levitation electrodes	α_{zs}	4^o
Number of levitation electrodes	–	2

Table 1 (continued)

Quantity	Symbol	Value
Inner radius of a out of plane rotation electrode	r_{1op}	7500 μm
Outer radius of a out of plane rotation electrode	r_{2op}	8300 μm
Sector angle of a out of plane rotation electrode	α_{op}	40^o
Angular spacing between out of plane rotation electrodes	α_{ops}	5^o
Number of out of plane electrodes	–	8
Inner radius of a lateral motion electrode	r_{1l}	10950 μm
Outer radius of a lateral motion electrode	r_{2l}	11700 μm
Sector angle of lateral motion electrode	α_l	39^o
Angular spacing between lateral motion electrodes	α_{ls}	1^o
Number of translational motion electrodes	–	4
Inner radius of a rotational motion actuation electrode	r_{1ract}	8750 μm
Outer radius of a rotational motion actuation electrode	r_{2ract}	9750 μm
Sector angle of a rotational motion actuation electrode	α_{ract}	1^o
Angular spacing between rotational motion actuation electrodes	α_{racts}	1^o
Number of rotational motion actuation electrodes / Number of phases	–	180/3
Inner radius of A rotational motion sense electrode	r_{1A}	5500 μm
Outer radius of A rotational motion sense electrode	r_{2A}	6400 μm
Sector angle of A rotational motion sense electrode	α_{sA}	120^o
Inner radius of B rotational motion sense electrode	r_{1B}	6600 μm
Outer radius of B rotational motion sense electrode	r_{2B}	7400 μm
Sector angle of B rotational motion sense electrode	α_{sB}	120^o
Inner radius of balancing opening#1	$r_{1bal,1}$	10000 μm

Table 1 (continued)

Quantity	Symbol	Value
Outer radius of balancing opening#1	$r_{2bal,1}$	10455.5 μm
Starting angle of balancing opening#1	$\alpha_{1bal,1}$	240.1°
Ending angle of balancing opening#1	$\alpha_{2bal,1}$	359.8 °
Inner radius of balancing opening#2	$r_{1bal,2}$	10000 μm
Outer radius of balancing opening#2	$r_{2bal,2}$	10455.5 μm
Starting angle of balancing opening#2	$\alpha_{1bal,2}$	76.2°
Ending angle of balancing opening#2	$\alpha_{2bal,2}$	103.7 °
Inner radius of balancing opening#3	$r_{1bal,3}$	10455.5 μm
Outer radius of balancing opening#3	$r_{2bal,3}$	10700 μm
Starting angle of balancing opening#1	$\alpha_{1bal,3}$	-13.24°
Ending angle of balancing opening#3	$\alpha_{2bal,3}$	13.24°
Inner radius of balancing opening#4	$r_{1bal,4}$	10455.5 μm
Outer radius of balancing opening#4	$r_{2bal,4}$	10700 μm
Starting angle of balancing opening#4	$\alpha_{1bal,4}$	166.8°
Ending angle of balancing opening#4	$\alpha_{2bal,4}$	193.2°
Inner radius of balancing opening#5	$r_{1bal,5}$	10455.5 μm
Outer radius of balancing opening#5	$r_{2bal,5}$	10700 μm
Starting angle of balancing opening#5	$\alpha_{1bal,5}$	34.17°
Ending angle of balancing opening#5	$\alpha_{2bal,5}$	55.83°
Inner radius of balancing opening#6	$r_{1bal,6}$	10455.5 μm
Outer radius of balancing opening#6	$r_{2bal,6}$	10700 μm
Starting angle of balancing opening#6	$\alpha_{1bal,6}$	214.2°
Ending angle of balancing opening#6	$\alpha_{2bal,6}$	235.8°

2.3 Modeling of MEMS Based Laser Scanner

In that section, physical reality of designed structure and mechanisms of capacitive actuation & detection will be transformed into mathematical models.

2.3.1 Capacitance Model

Formed capacitances between rotor and bottom & top stators are defined in Figure 8. Magnitudes of those capacitances depends position of the rotor relative to stators. Parameters to define rotor position and related coordinate frame are represented in Figure 13 below.

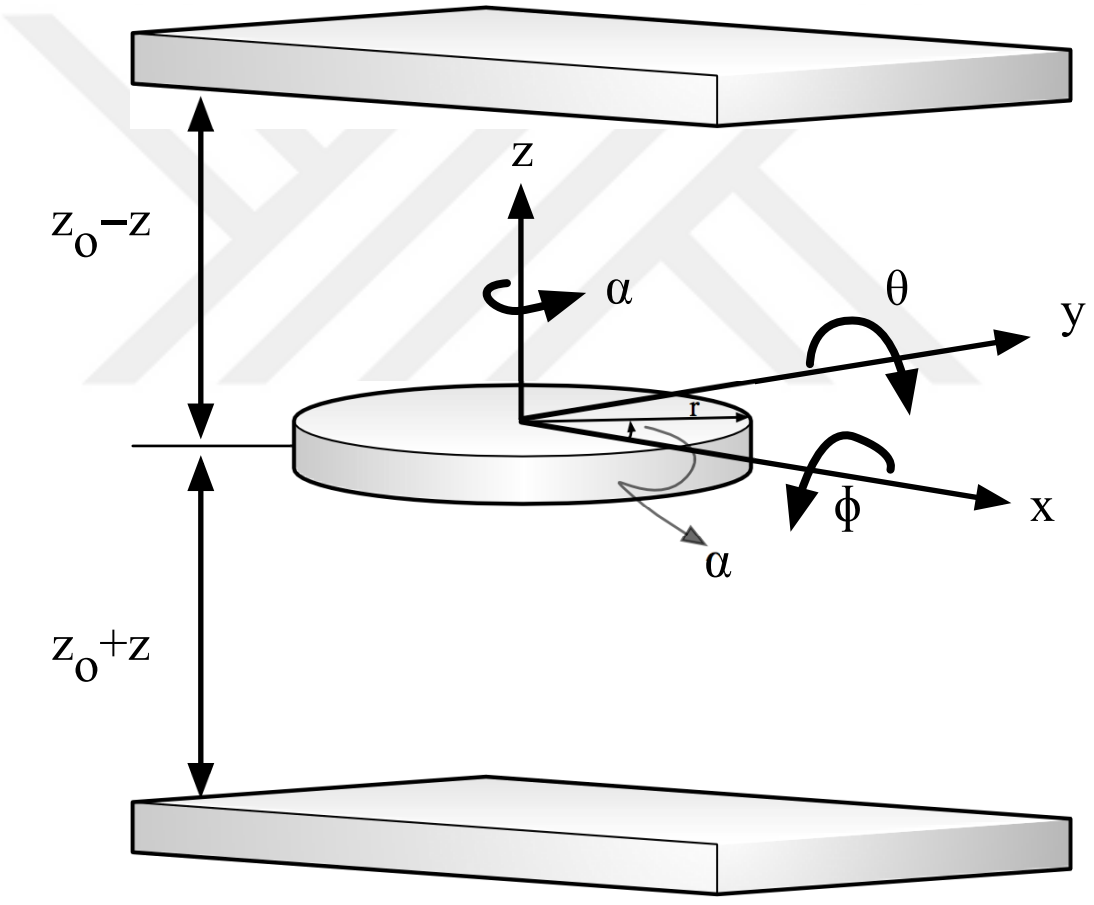

Figure 13 Motions of electrode between stators

Among formed capacitances, capacitances of out of plane motion electrodes, i.e. carrier electrodes, levitation electrodes and out of plane motion electrodes, change

due to change of nominal gap between rotor and stator, while capacitances of lateral motion electrodes changes due to both change of overlap area and nominal gap. In the proceeding two sections related equations for those mechanisms are developed.

2.3.1.1 Capacitance Model of Out of Plane Motion Electrodes

For carrier electrodes, levitation electrodes and out of plane motion electrodes it is assumed that lateral motion of the rotor between stators is kept small so that overlap area between rotor and those electrodes are constant. Therefore, capacitance changes due to change of nominal gap only.

Gap between stator and rotor is a function of z, θ, ϕ, r and α. Related expressions for the gap between bottom stator & rotor and top stator & rotor are given in equations (2.13) and (2.14) respectively below.

$$d_b\left(z,\phi,\theta,r,\alpha\right)=\left(z_o+z\right)+r\left(-\sin\theta+\cos\alpha\right)+\left(\sin\phi\sin\alpha\right) \tag{2.13}$$

$$d_t\left(z,\phi,\theta,r,\alpha\right)=\left(z_o-z\right)+r\left(\sin\theta\cos\alpha\right)+\left(-\sin\phi\sin\alpha\right) \tag{2.14}$$

If the rotations about x and y axes are assumed to be small gap expressions become

$$d_b\left(z,\phi,\theta,r,\alpha\right)=\left(z_o+z\right)+r\left(-\theta+\cos\alpha\right)+\left(\phi\sin\alpha\right) \tag{2.15}$$

$$d_t\left(z,\phi,\theta,r,\alpha\right)=\left(z_o-z\right)+r\left(\theta\cos\alpha\right)+\left(-\phi\sin\alpha\right) \tag{2.16}$$

Then capacitance expressions between an electrode located at bottom stator & rotor and between an electrode on top stator & rotor can be found as

$$\begin{aligned} C_{op,b}\left(z,\phi,\theta,r_1,r_2,\alpha_1,\alpha_2\right) &= \varepsilon\int_{\alpha_1}^{\alpha_2}\int_{r_1}^{r_2}\frac{r}{d_b\left(z,\phi,\theta\right)}dr\,d\alpha \\ &= \varepsilon\int_{\alpha_1}^{\alpha_2}\int_{r_1}^{r_2}\frac{r}{\left(z_o+z\right)+r\left(-\theta\cos\alpha+\phi\sin\alpha\right)}dr\,d\alpha \end{aligned} \tag{2.17}$$

$$C_{op,t}\left(z,\phi,\theta,r_1,r_2,\alpha_1,\alpha_2\right)=\varepsilon\int_{\alpha_1}^{\alpha_2}\int_{r_1}^{r_2}\frac{r}{d_u\left(z,\phi,\theta\right)}dr\,d\alpha$$
$$=\varepsilon\int_{\alpha_1}^{\alpha_2}\int_{r_1}^{r_2}\frac{r}{\left(z_o-z\right)+r\left(\theta\cos\alpha-\phi\sin\alpha\right)}dr\,d\alpha \tag{2.18}$$

For the solutions of above integrals, solution procedure that is outlined in [9] is used. Note that the solution procedures for the integrals given in (2.17) and (2.18) are the same. Therefore, from that point on solution will be given for C_b only. Before proceeding let define

$$\kappa\left(\alpha\right)=-\theta\cos\alpha+\phi\sin\alpha \tag{2.19}$$

$$z_b=z_o+z \tag{2.20}$$

Then integral given in equation (2.17) becomes

$$C_{op,b}\left(z,\phi,\theta,r_1,r_2,\alpha_1,\alpha_2\right)=\varepsilon\int_{\alpha_1}^{\alpha_2}\int_{r_1}^{r_2}\frac{r}{d_b\left(z,\phi,\theta\right)}dr\,d\alpha$$
$$=\varepsilon\int_{\alpha_1}^{\alpha_2}\int_{r_1}^{r_2}\frac{r}{z_b+r\kappa\left(\alpha\right)}dr\,d\alpha \tag{2.21}$$

Eliminating the inner integral equation (2.21) becomes,

$$C_{op,b}\left(z,\phi,\theta\right)=\varepsilon\int_{\alpha_1}^{\alpha_2}\frac{r_2-r_1}{\kappa\left(\alpha\right)}d\alpha+\varepsilon\int_{\alpha_1}^{\alpha_2}\frac{z_b\left(\ln\left(1+\frac{r_2}{z_b}\kappa\left(\alpha\right)\right)+\ln z_b\right)}{\kappa\left(\alpha\right)^2}d\alpha$$
$$+\varepsilon\int_{\alpha_1}^{\alpha_2}\frac{z_b\left(\ln\left(1+\frac{r_1}{z_b}\kappa\left(\alpha\right)\right)+\ln z_b\right)}{\kappa\left(\alpha\right)^2}d\alpha \tag{2.22}$$

In [9], natural logarithm terms in the above equation are approximated by using Taylor series expansion as follows.

$$C_{op,b}\left(z,\phi,\theta,r_1,r_2,\alpha_1,\alpha_2\right)=\varepsilon\int_{\alpha_1}^{\alpha_2}\frac{r_2-r_1}{\kappa\left(\alpha\right)}d\alpha$$
$$-\varepsilon z_b\int_{\alpha_1}^{\alpha_2}\left(\frac{\frac{r_2}{z_b}\kappa\left(\alpha\right)-\frac{1}{2}\left(\frac{r_2}{z_b}\right)^2\kappa\left(\alpha\right)^2}{\kappa\left(\alpha\right)^2}+\frac{\frac{1}{3}\left(\frac{r_2}{z_b}\right)^3\kappa\left(\alpha\right)^3-\frac{1}{4}\left(\frac{r_2}{z_b}\right)^4\kappa\left(\alpha\right)^4}{\kappa\left(\alpha\right)^2}\right)d\alpha \quad (2.23)$$
$$+\varepsilon z_b\int_{\alpha_1}^{\alpha_2}\left(\frac{\frac{r_1}{z_b}\kappa\left(\alpha\right)-\frac{1}{2}\left(\frac{r_1}{z_b}\right)^2\kappa\left(\alpha\right)^2}{\kappa\left(\alpha\right)^2}+\frac{\frac{1}{3}\left(\frac{r_1}{z_b}\right)^3\kappa\left(\alpha\right)^3-\frac{1}{4}\left(\frac{r_1}{z_b}\right)^4\kappa\left(\alpha\right)^4}{\kappa\left(\alpha\right)^2}\right)d\alpha$$

Evaluating above integral, gives C_b as

$$C_{op,b}\left(z,\phi,\theta,r_1,r_2,\alpha_1,\alpha_2\right)=$$
$$\varepsilon\left[\begin{array}{l}\frac{1}{2}\left(\frac{r_2^2-r_1^2}{z_o+z}\right)\left(\alpha_2-\alpha_1\right)-\frac{1}{3}\left(\frac{r_2^3-r_1^3}{\left(z_o+z\right)^2}\right)\left(\begin{array}{l}\theta\left(\sin\alpha_1-\sin\alpha_2\right)\\+\phi\left(\cos\alpha_1-\cos\alpha_2\right)\end{array}\right)\\+\frac{1}{4}\left(\frac{r_2^4-r_1^4}{\left(z_o+z\right)^3}\right)\left(\begin{array}{l}\theta^2\left(\frac{\alpha_2-\alpha_1}{2}+\frac{\sin2\alpha_2-\sin2\alpha_1}{4}\right)\\+\phi^2\left(\frac{\alpha_2-\alpha_1}{2}-\frac{\sin2\alpha_2-\sin2\alpha_1}{4}\right)\\+\frac{\phi\theta}{2}\left(\cos2\alpha_2-\cos2\alpha_1\right)\end{array}\right)\end{array}\right] \quad (2.24)$$

By changing the signs of z, ϕ and θ in equation (2.24) above, capacitance formed between a top stator electrode and rotor can be formulated as

$$C_{op,t}\left(z,\phi,\theta,r_1,r_2,\alpha_1,\alpha_2\right)=$$
$$\varepsilon\left[\begin{array}{l}\frac{1}{2}\left(\frac{r_2^{\,2}-r_1^{\,2}}{z_o-z}\right)\left(\alpha_2-\alpha_1\right)+\frac{1}{3}\left(\frac{r_2^{\,3}-r_1^{\,3}}{\left(z_o-z\right)^2}\right)\left(\begin{array}{l}\theta\left(\sin\alpha_1-\sin\alpha_2\right)\\+\phi\left(\cos\alpha_1-\cos\alpha_2\right)\end{array}\right)\\+\frac{1}{4}\left(\frac{r_2^{\,4}-r_1^{\,4}}{\left(z_o-z\right)^3}\right)\left(\begin{array}{l}\theta^2\left(\frac{\alpha_2-\alpha_1}{2}+\frac{\sin2\alpha_2-\sin2\alpha_1}{4}\right)\\+\phi^2\left(\frac{\alpha_2-\alpha_1}{2}-\frac{\sin2\alpha_2-\sin2\alpha_1}{4}\right)\\+\frac{\phi\theta}{2}\left(\cos2\alpha_2-\cos2\alpha_1\right)\end{array}\right)\end{array}\right] \tag{2.25}$$

where, r_1 and r_2 are the inner and outer diameter of electrode in interest, α_1 and α_2 are start and end angle of pie shaped electrode in interest. Note that r_1, r_2, α_1 and α_2 are fixed for the electrode of interest. Therefore, capacitance expression is function of z, ϕ and θ only.

2.3.1.2 Capacitance Model of Lateral Motion Electrodes

For lateral motion electrodes, capacitance change due to both change of nominal gap and overlap area. Therefore, capacitance expression becomes function of x,y,z,ϕ and θ. As stated in [9], derivation of this capacitance model is quite cumbersome and since rotations of rotor about x and y axes are already assumed to be small, capacitance model can be approximated as,

$$C_{l,b}\left(x,y,z,\phi,\theta,\alpha_1,\alpha_2\right)=\frac{A_{new}\left(x,y\right)}{A_{nom}}C_{op,b}\left(z,\phi,\theta,r_{1t},r_r,\alpha_1,\alpha_2\right) \tag{2.26}$$

where A_{new} is the overlap area as a function of rotor position on x and y axes, A_{nom} is the overlap area between rotor and stators when rotor is at its nominal position i.e., $x=y=z=\phi=\theta=0$ and $C_{op,b}$ is out of plane electrode capacitance model, which already derived in the previous section.

Figure 14 shows overlapped areas between lateral motion electrodes and rotor, when rotor deviates (x,y) from its nominal position. In Figure 14, nominal position of the

rotor is represented by dashed circle while deviated rotor position is shown by solid circle. Orange shaded area shows overlapped area between rotor and a x-translation electrode when rotor deviates from its nominal position by (x,y), i.e. A_{new}. Nominal overlap area (A_{nom}) is the portion of the orange area formed between r_{1t} and r_r.

Polar equation of the deviated rotor is expressed as

$$f_1(x,y,\alpha) = r\cos(\alpha-\phi) + \sqrt{r_r^2 - r^2\sin^2(\alpha-\phi)} \tag{2.27}$$

where,

$$r = \sqrt{x^2+y^2} \text{ and } \gamma = a\tan 2(x,y) \tag{2.28}$$

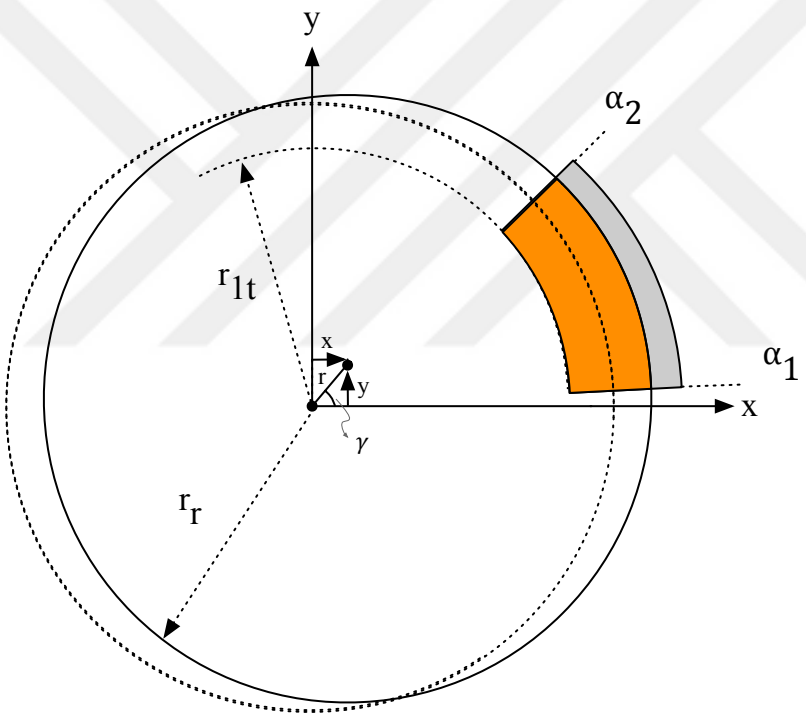

Figure 14 Overlapped area between rotor and a x-translation electrode

Polar equation of inner boundary of the given lateral motion electrode is

$$f_2 = r_{1t} \tag{2.29}$$

Resulting area between those two curves gives overlapped area as

$$A_{new}(x,y)=\frac{1}{2}\int_{\alpha_1}^{\alpha_2}\left(f_1(x,y,alpha)^2-f_2^{\,2}\right)d\alpha$$

$$A_{new}(x,y)=\frac{1}{2}\int_{\alpha_1}^{\alpha_2}\left(\left(r\cos(\alpha-\gamma)+\sqrt{r_r^{\,2}-r^2\sin^2(\alpha-\gamma)}\right)^2-r_{1t}^{\,2}\right)d\alpha \qquad (2.30)$$

Evaluating the integral given in equations (2.30) gives overlapped area as a function of rotor lateral position as

$$\begin{aligned}A_{new}(x,y)&=\left(r_r^{\,2}-r_{1t}^{\,2}\right)\frac{\alpha_2-\alpha_1}{2}+\frac{r^2}{4}\left(\sin 2(\alpha_2-\gamma)-\sin 2(\alpha_1-\gamma)\right)\\&+\frac{r_r^{\,2}}{2}\left(a\tan\left(\frac{r\sin(\alpha_2-\gamma)}{\sqrt{r_r^{\,2}-r^2\sin^2(\alpha_2-\gamma)}}\right)-a\tan\left(\frac{r\sin(\alpha_1-\gamma)}{\sqrt{r_r^{\,2}-r^2\sin^2(\alpha_1-\gamma)}}\right)\right)\\&+\frac{r}{2}\left(\sin(\alpha_2-\gamma)\sqrt{r_r^{\,2}-r^2\sin^2(\alpha_2-\gamma)}-\sin(\alpha_1-\gamma)\sqrt{r_r^{\,2}-r^2\sin^2(\alpha_1-\gamma)}\right)\end{aligned} \qquad (2.31)$$

Nominal overlap area, on the other hand, is

$$A_{nom}=\left(r_r^{\,2}-r_{1t}^{\,2}\right)(\alpha_2-\alpha_1)/2 \qquad (2.32)$$

Finally; capacitance model for lateral motion electrodes located on bottom stator is obtained by substituting (2.24), (2.31) and (2.32) into (2.26). Resulting expression is given in (2.33).

Similarly, capacitance model for lateral motion electrodes located on top stator can be found by using equation (2.25) in (2.26) instead of (2.24). Resulting expression is given in equation (2.34).

$$C_{l,b}\left(x,y,z,\phi,\theta,\alpha_1,\alpha_2\right)=$$

$$\varepsilon\left[\begin{array}{l}\left(\frac{r_r^{\,2}-r_{1t}^{\,2}}{z_o+z}\right)\left(\alpha_2-\alpha_1\right)-\frac{1}{3}\left(\frac{r_r^{\,3}-r_{1t}^{\,3}}{\left(z_o+z\right)^2}\right)\left(\theta\left(\sin\alpha_1-\sin\alpha_2\right)+\phi\left(\cos\alpha_1-\cos\alpha_2\right)\right)\\ +\frac{1}{4}\left(\frac{r_r^{\,4}-r_{1t}^{\,4}}{\left(z_o+z\right)^3}\right)\left(\begin{array}{l}\theta^2\left(\frac{\alpha_2-\alpha_1}{2}+\frac{\sin2\alpha_2-\sin2\alpha_1}{4}\right)\\ +\phi^2\left(\frac{\alpha_2-\alpha_1}{2}-\frac{\sin2\alpha_2-\sin2\alpha_1}{4}\right)+\frac{\phi\theta}{2}\left(\cos2\alpha_2-\cos2\alpha_1\right)\end{array}\right)\end{array}\right] \quad (2.33)$$

$$\left[\begin{array}{l}\left(r_r^{\,2}-r_{1t}^{\,2}\right)\frac{\alpha_2-\alpha_1}{2}+\frac{r^2}{4}\left(\sin2\left(\alpha_2-\gamma\right)-\sin2\left(\alpha_1-\gamma\right)\right)\\ +\frac{r_r^{\,2}}{2}\left(a\tan\left(\frac{r\sin\left(\alpha_2-\gamma\right)}{\sqrt{r_r^{\,2}-r^2\sin^2\left(\alpha_2-\gamma\right)}}\right)-a\tan\left(\frac{r\sin\left(\alpha_1-\gamma\right)}{\sqrt{r_r^{\,2}-r^2\sin^2\left(\alpha_1-\gamma\right)}}\right)\right)\\ +\frac{r}{2}\left(\sin\left(\alpha_2-\gamma\right)\sqrt{r_r^{\,2}-r^2\sin^2\left(\alpha_2-\gamma\right)}-\sin\left(\alpha_1-\gamma\right)\sqrt{r_r^{\,2}-r^2\sin^2\left(\alpha_1-\gamma\right)}\right)\end{array}\right]$$

$$/\left[\left(r_r^{\,2}-r_{1t}^{\,2}\right)\left(\alpha_2-\alpha_1\right)\right]$$

$$C_{l,t}\left(x,y,z,\phi,\theta,\alpha_1,\alpha_2\right)=$$

$$\varepsilon\left[\begin{array}{l}\left(\frac{r_2^{\,2}-r_1^{\,2}}{z_o-z}\right)\left(\alpha_2-\alpha_1\right)+\frac{1}{3}\left(\frac{r_2^{\,3}-r_1^{\,3}}{\left(z_o-z\right)^2}\right)\left(\theta\left(\sin\alpha_1-\sin\alpha_2\right)+\phi\left(\cos\alpha_1-\cos\alpha_2\right)\right)\\ +\frac{1}{4}\left(\frac{r_2^{\,4}-r_1^{\,4}}{\left(z_o-z\right)^3}\right)\left(\begin{array}{l}\theta^2\left(\frac{\alpha_2-\alpha_1}{2}+\frac{\sin2\alpha_2-\sin2\alpha_1}{4}\right)\\ +\phi^2\left(\frac{\alpha_2-\alpha_1}{2}-\frac{\sin2\alpha_2-\sin2\alpha_1}{4}\right)\\ +\frac{\phi\theta}{2}\left(\cos2\alpha_2-\cos2\alpha_1\right)\end{array}\right)\end{array}\right] \quad (2.34)$$

$$\left[\begin{array}{l}\left(r_r^{\,2}-r_{1t}^{\,2}\right)\frac{\alpha_2-\alpha_1}{2}+\frac{r^2}{4}\left(\sin2\left(\alpha_2-\gamma\right)-\sin2\left(\alpha_1-\gamma\right)\right)\\ +\frac{r_r^{\,2}}{2}\left(a\tan\left(\frac{r\sin\left(\alpha_2-\gamma\right)}{\sqrt{r_r^{\,2}-r^2\sin^2\left(\alpha_2-\gamma\right)}}\right)-a\tan\left(\frac{r\sin\left(\alpha_1-\gamma\right)}{\sqrt{r_r^{\,2}-r^2\sin^2\left(\alpha_1-\gamma\right)}}\right)\right)\\ +\frac{r}{2}\left(\sin\left(\alpha_2-\gamma\right)\sqrt{r_r^{\,2}-r^2\sin^2\left(\alpha_2-\gamma\right)}-\sin\left(\alpha_1-\gamma\right)\sqrt{r_r^{\,2}-r^2\sin^2\left(\alpha_1-\gamma\right)}\right)\end{array}\right]$$

$$/\left[\left(r_r^{\,2}-r_{1t}^{\,2}\right)\left(\alpha_2-\alpha_1\right)\right]$$

2.3.2 Capacitive Actuation Model

In that section capacitive actuation models for out of plane motion electrodes and lateral motion electrodes are represented.

2.3.2.1 Actuation Model of Out of Plane Motion Electrodes

For levitation, one should generate force to overcome gravity and balance out of plane rotations of the rotor, while it is hanging in the air. In this application this is achieved by using electrode couples z1&z2, rx+1&rx+2, rx-1&rx-2, ry+1&ry+2 and ry+1&ry+2 located on each stator. All of those electrode pairs are used to generate forces along z direction. However, for out of plane rotational torques, only electrode pairs labeled with `r` are used.

As given in equation (2.2), force generated along z direction and moments generated about x and y axes by a bottom/top out of plane motion electrode are found as

$$F_{op,zb/t}\left(z,\phi,\theta,V,\alpha_1,\alpha_2,r_1,r_2\right)=\frac{1}{2}\frac{\partial C_{op,b/t}\left(z,\phi,\theta,V,\alpha_1,\alpha_2,r_1,r_2\right)}{\partial z}V^2 \tag{2.35}$$

$$M_{op,\phi b/t}\left(z,\phi,\theta,V,\alpha_1,\alpha_2,r_1,r_2\right)=\frac{1}{2}\frac{\partial C_{op,b/t}\left(z,\phi,\theta,V,\alpha_1,\alpha_2,r_1,r_2\right)}{\partial \phi}V^2 \tag{2.36}$$

$$M_{op,\theta b/t}\left(z,\phi,\theta,V,\alpha_1,\alpha_2,r_1,r_2\right)=\frac{1}{2}\frac{\partial C_{op,b/t}\left(z,\phi,\theta,V,\alpha_1,\alpha_2,r_1,r_2\right)}{\partial \theta}V^2 \tag{2.37}$$

where, α_1, α_2, r_1 and r_2 are the geometric properties of the electrode in interest, V is applied potential to electrode in interest as defined in Figure 10. Derivatives in equations (2.35), (2.36) and (2.37) will be evaluated numerically in the Simulink model of the proposed structure.

2.3.2.2 Actuation Model of Lateral Motion Electrodes

As rotor is hovering, it may drift along x and/or y axes. To control that movement, forces need to be generated along those axes, which is achieved by lateral motion electrodes, labeled as x+1 & x+2, x-1 & x-2 and y+1 & y+2, y-1 & y-2.

Applied voltages on lateral motion electrodes not only generate forces along x and/or y direction but also they may generate forces or moments along other axes depending on the position of the rotor. Generated forces along x,y,z direction and generated moments about x and y axes by a lateral motion electrode located on bottom/top stator, are found by evaluating the equations given below.

$$F_{l,xb/t}\left(x,y,z,\phi,\theta,V,\alpha_1,\alpha_2\right)=\frac{1}{2}\frac{\partial C_{l,b/t}\left(x,y,z,\phi,\theta,V,\alpha_1,\alpha_2\right)}{\partial x}V^2 \tag{2.38}$$

$$F_{l,yb/t}\left(x,y,z,\phi,\theta,V,\alpha_1,\alpha_2\right)=\frac{1}{2}\frac{\partial C_{l,b/t}\left(x,y,z,\phi,\theta,V,\alpha_1,\alpha_2\right)}{\partial z}V^2 \tag{2.39}$$

$$F_{l,zb/t}\left(x,y,z,\phi,\theta,V,\alpha_1,\alpha_2\right)=\frac{1}{2}\frac{\partial C_{l,b/t}\left(x,y,z,\phi,\theta,V,\alpha_1,\alpha_2\right)}{\partial z}V^2 \tag{2.40}$$

$$M_{l,\phi b/t}\left(x,y,z,\phi,\theta,V,\alpha_1,\alpha_2\right)=\frac{1}{2}\frac{\partial C_{l,b/t}\left(x,y,z,\phi,\theta,V,\alpha_1,\alpha_2\right)}{\partial \phi}V^2 \tag{2.41}$$

$$M_{l,\theta b/t}\left(x,y,z,\phi,\theta,V,\alpha_1,\alpha_2\right)=\frac{1}{2}\frac{\partial C_{l,b/t}\left(x,y,z,\phi,\theta,V,\alpha_1,\alpha_2\right)}{\partial \theta}V^2 \tag{2.42}$$

where, α_1, α_2, r_1 and r_2 are the geometric properties of the electrode in interest, V is applied potential to electrode in interest as defined in Figure 10. Above equations will be evaluated numerically in Simulink simulations.

2.3.3 Rotor Dynamics

Rotor moves under the effects of the generated forces by top and bottom stator electrodes and air damping. Moreover, spring effect is generated along the axes, where air is squeezed. In the following subsections, electrostatic forces acting on the

rotor and damping & stiffness models are explained. After that equation of motion of the rotor is represented. Note that to define the motion of the rotor and direction of the forces, coordinate frame that is represented in Figure 13 in Section 2.3.1 is used.

2.3.3.1 Forces and Moments Acting on Rotor

As shown in Figure 10, feedback voltages are applied to each electrode to control the motion of the rotor at 6 degrees of freedom. Although feedback voltages are specific to each axis and applied to dedicated motion control electrodes only, they may generate unintended forces and/or moments on the other axes depending on the position of rotor. In the following sub-sections, generated forces and moments on the rotor are represented for each axis. Note that for that application it is assumed that rotor is rotated about z axis only if it is balanced along 5 remaining axes. Therefore, forces generated by rotation electrodes along x, y, z axes and moments about generated about x and y axes on rotor are neglected.

2.3.3.1.1 Forces Acting on Rotor Along x-direction

Since it is assumed that lateral motion of the rotor is kept small enough to prevent overlap area change between rotor and out of plane motion electrodes, only lateral motion electrodes generates force along x direction and overall force expression in that direction is given in equation (2.43) below.

$$\begin{aligned} F_x(x,y,z,\phi,\theta,V) = &\sum_{n=1}^{n=8} F_{l,xb}\left(x,y,z,\phi,\theta,V_{l,bn},\frac{2n-1}{2}\alpha_{ls}+n\alpha_l,\frac{2n-1}{2}\alpha_{ls}+(n+1)\alpha_l\right) \\ &+\sum_{n=1}^{n=8} F_{l,xt}\left(x,y,z,\phi,\theta,V_{l,tn},\frac{2n-1}{2}\alpha_{ls}+n\alpha_l,\frac{2n-1}{2}\alpha_{ls}+(n+1)\alpha_l\right) \end{aligned} \quad (2.43)$$

2.3.3.1.2 Forces Acting on Rotor Along y-direction

Similar to x-axis forces, only lateral motion electrodes generate force along y-direction and its expression is represented in equation (2.44).

$$F_y\left(x,y,z,\phi,\theta,V\right)=\sum_{n=1}^{n=8}F_{l,yb}\left(x,y,z,\phi,\theta,V_{l,bn},\frac{2n-1}{2}\alpha_{ls}+n\alpha_l,\frac{2n-1}{2}\alpha_{ls}+(n+1)\alpha_l\right)$$
$$+\sum_{n=1}^{n=8}F_{l,yt}\left(x,y,z,\phi,\theta,V_{l,tn},\frac{2n-1}{2}\alpha_{ls}+n\alpha_l,\frac{2n-1}{2}\alpha_{ls}+(n+1)\alpha_l\right) \quad (2.44)$$

2.3.3.1.3 Force Acting on Rotor Along z-direction

All of the stator electrodes other than rotation electrodes generates forces on rotor along z-axis according to equations (2.35) and (2.40). Overall force acting on rotor along z direction is given in (2.45) below.

$$\begin{aligned}
&F_z\left(x,y,z,\phi,\theta,V\right)=\\
&\sum_{n=1}^{n=2}F_{op,zb}\left(x,y,z,\phi,\theta,r_{1z},r_{2z},\frac{(-1)^n}{2}\alpha_z+(n-1)\alpha_{zs},\frac{2n-1}{2}\alpha_z+(n-1)\alpha_{zs},V_{z,bn}\right)\\
&+\sum_{n=1}^{n=2}F_{op,zt}\left(x,y,z,\phi,\theta,r_{1z},r_{2z},\frac{(-1)^n}{2}\alpha_z+(n-1)\alpha_{zs},\frac{2n-1}{2}\alpha_z+(n-1)\alpha_{zs},V_{z,tn}\right)\\
&+\sum_{n=1}^{n=8}F_{op,zb}\left(x,y,z,\phi,\theta,r_{1op},r_{2op},\frac{2n-1}{2}\alpha_{ops}+n\alpha_{op},\frac{2n-1}{2}\alpha_{ops}+(n+1)\alpha_{op},V_{op,bn}\right)\\
&+\sum_{n=1}^{n=8}F_{op,zt}\left(x,y,z,\phi,\theta,r_{1op},r_{2op},\frac{2n-1}{2}\alpha_{ops}+n\alpha_{op},\frac{2n-1}{2}\alpha_{ops}+(n+1)\alpha_{op},V_{op,tn}\right)\\
&+\sum_{n=1}^{n=8}F_{l,zb}\left(x,y,z,\phi,\theta,\frac{2n-1}{2}\alpha_{ls}+n\alpha_l,\frac{2n-1}{2}\alpha_{ls}+(n+1)\alpha_z,V_{l,bn}\right)\\
&+\sum_{n=1}^{n=8}F_{l,zt}\left(x,y,z,\phi,\theta,\frac{2n-1}{2}\alpha_{ls}+n\alpha_l,\frac{2n-1}{2}\alpha_{ls}+(n+1)\alpha_z,V_{l,tn}\right)
\end{aligned} \quad (2.45)$$

2.3.3.1.4 Moment Acting on Rotor About x-axis

All of the electrodes generate moment about x axis based on equations (2.36) and (2.41). Overall moment acting on rotor is given in equation (2.46) below.

$$
\begin{aligned}
&M_{\phi}\left(x,y,z,\phi,\theta,V\right)= \\
&\sum_{n=1}^{n=2} M_{op,\phi b}\left(x,y,z,\phi,\theta,r_{1z},r_{2z},\frac{(-1)^{n}}{2}\alpha_{z}+(n-1)\alpha_{zs},\frac{2n-1}{2}\alpha_{z}+(n-1)\alpha_{zs},V_{z,bn}\right) \\
&+\sum_{n=1}^{n=2} M_{op,\phi t}\left(x,y,z,\phi,\theta,r_{1z},r_{2z},\frac{(-1)^{n}}{2}\alpha_{z}+(n-1)\alpha_{zs},\frac{2n-1}{2}\alpha_{z}+(n-1)\alpha_{zs},V_{z,tn}\right) \\
&+\sum_{n=1}^{n=8} M_{op,\phi b}\left(x,y,z,\phi,\theta,r_{1op},r_{2op},\frac{2n-1}{2}\alpha_{ops}+n\alpha_{op},\frac{2n-1}{2}\alpha_{ops}+(n+1)\alpha_{op},V_{op,bn}\right) \\
&+\sum_{n=1}^{n=8} M_{op,\phi t}\left(x,y,z,\phi,\theta,r_{1op},r_{2op},\frac{2n-1}{2}\alpha_{ops}+n\alpha_{op},\frac{2n-1}{2}\alpha_{ops}+(n+1)\alpha_{op},V_{op,tn}\right) \\
&+\sum_{n=1}^{n=8} M_{l,\phi b}\left(x,y,z,\phi,\theta,\frac{2n-1}{2}\alpha_{ls}+n\alpha_{l},\frac{2n-1}{2}\alpha_{ls}+(n+1)\alpha_{z},V_{l,bn}\right) \\
&+\sum_{n=1}^{n=8} M_{l,\phi t}\left(x,y,z,\phi,\theta,\frac{2n-1}{2}\alpha_{ls}+n\alpha_{l},\frac{2n-1}{2}\alpha_{ls}+(n+1)\alpha_{z},V_{l,tn}\right)
\end{aligned}
\tag{2.46}
$$

2.3.3.1.5 Moment Acting on Rotor About y-axis

Similarly, all of the electrodes generate moment on rotor about y axis. Overall moment acting on the rotor is given in equation (2.47).

$$
\begin{aligned}
&M_{\theta}\left(x,y,z,\phi,\theta,V\right)= \\
&\sum_{n=1}^{n=2} M_{op,\theta b}\left(x,y,z,\phi,\theta,r_{1z},r_{2z},\frac{(-1)^{n}}{2}\alpha_{z}+(n-1)\alpha_{zs},\frac{2n-1}{2}\alpha_{z}+(n-1)\alpha_{zs},V_{z,bn}\right) \\
&+\sum_{n=1}^{n=2} M_{op,\theta t}\left(x,y,z,\phi,\theta,r_{1z},r_{2z},\frac{(-1)^{n}}{2}\alpha_{z}+(n-1)\alpha_{zs},\frac{2n-1}{2}\alpha_{z}+(n-1)\alpha_{zs},V_{z,tn}\right) \\
&+\sum_{n=1}^{n=8} M_{op,\theta b}\left(x,y,z,\phi,\theta,r_{1op},r_{2op},\frac{2n-1}{2}\alpha_{ops}+n\alpha_{op},\frac{2n-1}{2}\alpha_{ops}+(n+1)\alpha_{op},V_{op,bn}\right) \\
&+\sum_{n=1}^{n=8} M_{op,\theta t}\left(x,y,z,\phi,\theta,r_{1op},r_{2op},\frac{2n-1}{2}\alpha_{ops}+n\alpha_{op},\frac{2n-1}{2}\alpha_{ops}+(n+1)\alpha_{op},V_{op,tn}\right) \\
&+\sum_{n=1}^{n=8} M_{l,\theta b}\left(x,y,z,\phi,\theta,\frac{2n-1}{2}\alpha_{ls}+n\alpha_{l},\frac{2n-1}{2}\alpha_{ls}+(n+1)\alpha_{z},V_{l,bn}\right) \\
&+\sum_{n=1}^{n=8} M_{l,\theta t}\left(x,y,z,\phi,\theta,\frac{2n-1}{2}\alpha_{ls}+n\alpha_{l},\frac{2n-1}{2}\alpha_{ls}+(n+1)\alpha_{z},V_{l,tn}\right)
\end{aligned}
\tag{2.47}
$$

2.3.3.2 Damping and Stiffness Acting Rotor

Air generates damping on the motion on the rotor along 5 axes. As stated in [35], air between small gaps can behave as a spring and damper depending on the operation pressure. Therefore, for the translational motion of the rotor along z-axis and rotational motion of the rotor about x & y axes, squeezed air creates spring effect in addition to damping. On the other hand, for the translational motion of rotor along x and y axes, i.e. lateral motion, sliding air on the surface of rotor generates damping effect only. Before proceeding further, note that for the estimation of damping and stiffness coefficients, rotor is taken as disc without any holes.

Squeezed film model for a circular plate in parallel motion, which involves Kelvin functions, given in [36, 37] as;

$$f_{c0} = -\sqrt{\frac{2}{\sigma}}\left[A_c\left(ber_1\sqrt{\sigma} - bei_1\sqrt{\sigma}\right) + B_c\left(ber_1\sqrt{\sigma} + bei_1\sqrt{\sigma}\right)\right] \tag{2.48}$$

$$f_{c1} = 1 + \sqrt{\frac{2}{\sigma}}\left[A_c\left(ber_1\sqrt{\sigma} - bei_1\sqrt{\sigma}\right) - B_c\left(ber_1\sqrt{\sigma} + bei_1\sqrt{\sigma}\right)\right] \tag{2.49}$$

where, f_{c0} and f_{c1} are nondimensional damping and spring forces respectively. Squeeze number σ and constants A_c and B_c are defined as

$$\sigma = \frac{12\mu R^2}{P_a z_o^{\,2}}\omega \tag{2.50}$$

$$A_c = \frac{bei\sqrt{\sigma}}{\left(ber^2\sqrt{\sigma} + bei^2\sqrt{\sigma}\right)} \tag{2.51}$$

$$B_c = -\frac{ber\sqrt{\sigma}}{\left(ber^2\sqrt{\sigma} + bei^2\sqrt{\sigma}\right)} \tag{2.52}$$

where, μ is viscosity of air, P_a is ambient pressure, ω is operational frequency, R is radius of rotor and z_o is nominal gap between rotor and stator. Then using equations (2.48) and (2.49) damping and stiffness coefficients acting on the rotor for translational motion along z axis is found as

$$k_z = 2\frac{AP_a}{\omega z_o} f_{c0} \tag{2.53}$$

$$b_z = 2\frac{AP_a}{z_o} f_{c1} \tag{2.54}$$

where, A is area of rotor.

In order to find torsional damping and stiffness acting on the rotor, damping and stiffness found for z axis are assumed constant along the surface of the rotor. Then using z-axis damping and stiffness, equivalent torsional damping and stiffness values are found as follows.

For equivalent damping,

$$\int_0^{2\pi}\int_0^{R} (r\dot{\theta})^2 \frac{b_z}{\pi R^2} r\,dr\,d\alpha = b_\theta \dot{\theta}^2 \rightarrow b_\theta = b_\phi = \frac{b_z R^2}{2} \tag{2.55}$$

For equivalent stiffness

$$\frac{1}{2}\int_0^{2\pi}\int_0^{R} (r\theta)^2 \frac{k_z}{\pi R^2} r\,dr\,d\alpha = \frac{1}{2} k_\theta \theta^2 \rightarrow k_\theta = k_\phi = \frac{k_z R^2}{2} \tag{2.56}$$

For lateral motion, on the other hand, only slide film damping is present. Damping coefficient can be estimated as [38]

$$b_x = b_y = 2\frac{\eta A}{z_o} \tag{2.57}$$

where, A is area of rotor, η is dynamic viscosity of air and z_o is nominal gap.

2.3.3.3 Equation of Motion of Rotor

Equation of motion of rotor is defined by using the simple mass spring damper equation. Using the force expressions represented from equations (2.43) to (2.47) and damping & stiffness coefficients given between equations (2.53) to (2.57), motion models of the rotor along 5 axes in Laplace domain are represented as follows,

$$ms^2X + b_x sX = F_x \tag{2.58}$$

$$ms^2Y + b_y sY = F_y \tag{2.59}$$

$$ms^2Z + b_z sZ + k_z Z = F_z \tag{2.60}$$

$$I_{xx}s^2\Phi + b_\phi s\Phi + k_\phi \Phi = M_\phi \tag{2.61}$$

$$I_{yy}s^2\Theta + b_\theta s\Theta + k_\theta \Theta = M_\theta \tag{2.62}$$

2.3.4 Capacitive Detection Model

Position of the rotor is measured electrostatically, by using electrodes as described in Section 2.2.1.2. In the following sub-sections, capacitive detection models, including their readout circuitry is represented for each axis.

2.3.4.1 Capacitive Detection Model for Lateral Movement

As given in equation (2.8), to detect lateral motion of the rotor, electrode pairs are combined in a differential reading configuration. This reading configuration together with the reading circuit is represented in the Figure 15. Note that measuring mechanisms for the x and y direction are the same. Therefore, only x direction mechanism is discussed in that section.

The reading circuitry is based on [39]. As represented in Figure 15, movement of rotor in x direction generates currents (i_{x+} and i_{x-}) and they are converted to voltages (V_{x+} and V_{x-}) by using trans-impedance amplifiers (TIA). Converted voltages are fed to an instrumentation amplifier and differential reading signal (DV_x) is created. Finally that signal is demodulated then low pass filtered and x position measuring signal (V_x) is generated.

Recall that for lateral motion same set of electrodes are used for both actuation and sensing. Electrode voltages ($V_{x+1t/b}$, $V_{x+2t/b}$, $V_{x-1t/b}$, $V_{x-2t/b}$) are applied to related electrodes through a RC high pass filter with a resistance R_h and a capacitor C_h.

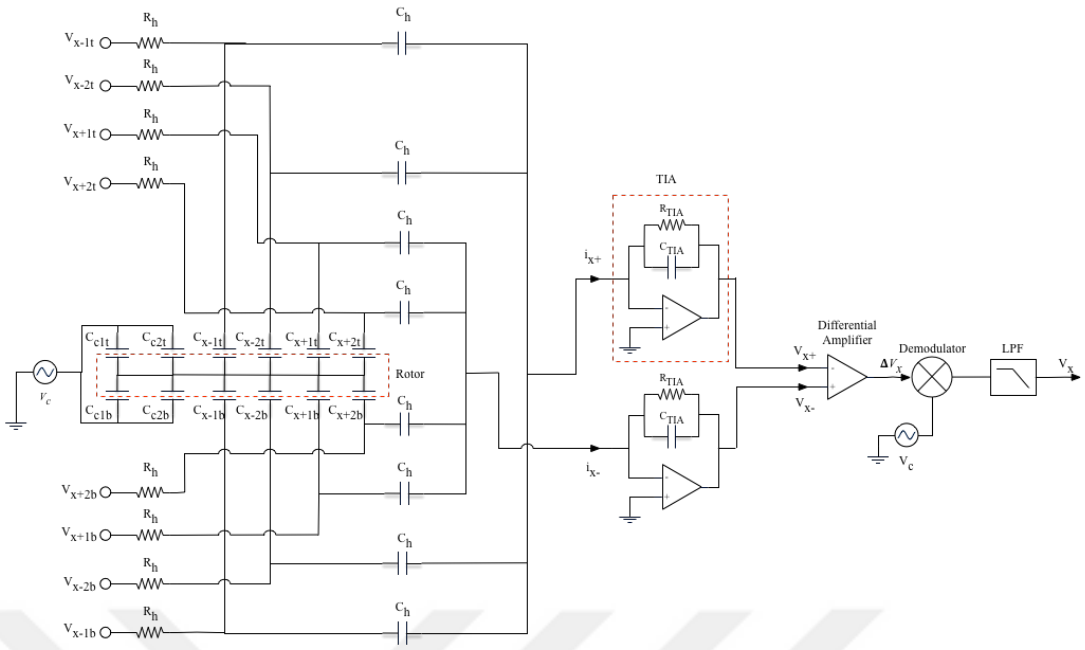

Figure 15 Electrode configuration for x axis translational motion detection and its reading circuit

Assuming $R_h >> (1/\omega_{carrier} C_h)$ capacitance model given in Figure 15 can be approximated as shown in Figure 16 (a).

The capacitance model in Figure 16 (a) is further simplified into a more compact version as shown in Figure 16 (b) where,

$$C_c = C_{c1t} + C_{c2t} + C_{c1b} + C_{c2b} \tag{2.63}$$

$$C_{x+} = \frac{C_{x+1t} C_h}{C_{x+1t} + C_h} + \frac{C_{x+2t} C_h}{C_{x+2t} + C_h} + \frac{C_{x+1b} C_h}{C_{x+1b} + C_h} + \frac{C_{x+1b} C_h}{C_{x+1b} + C_h} \tag{2.64}$$

$$C_{x-} = \frac{C_{x-1t} C_h}{C_{x-1t} + C_h} + \frac{C_{x-2t} C_h}{C_{x-2t} + C_h} + \frac{C_{x-1b} C_h}{C_{x-1b} + C_h} + \frac{C_{x-1b} C_h}{C_{x-1b} + C_h} \tag{2.65}$$

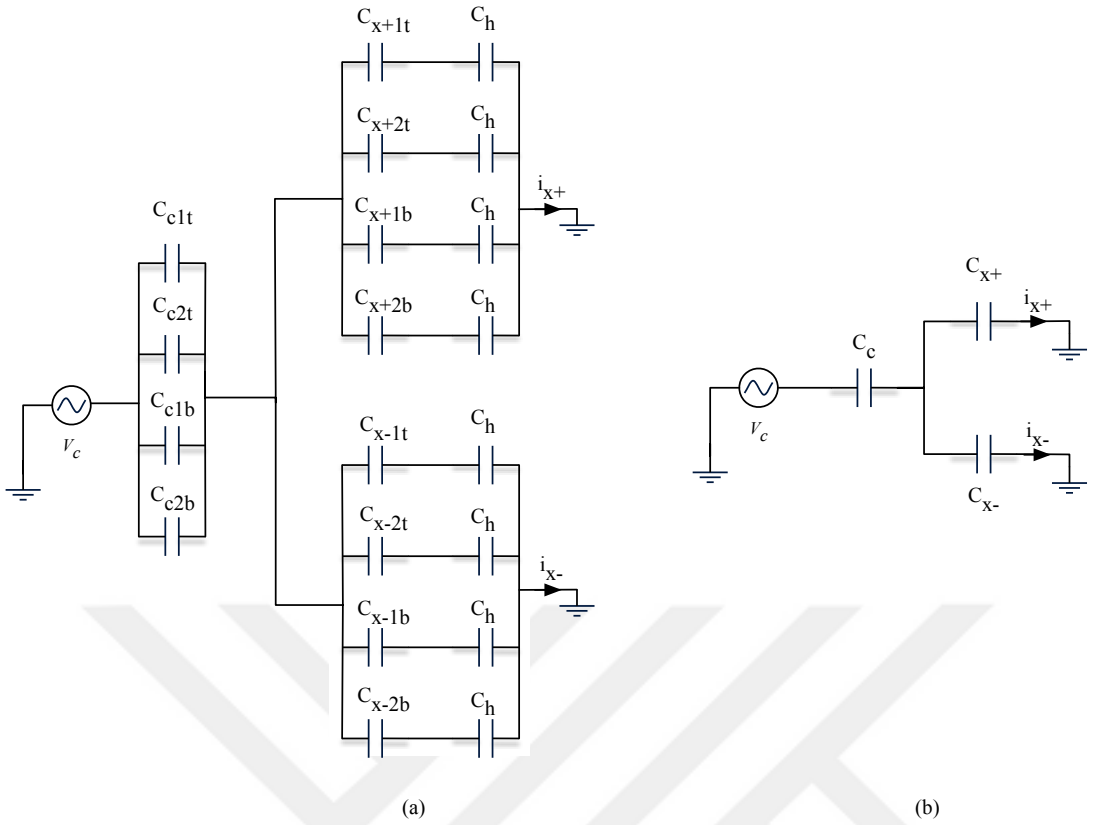

Figure 16 (a) Approximated x-lateral motion capacitance reading model. (b) Compact representation of approximated model

Using the simplified capacitance model in Figure 16 (b) expressions for generated current i_{x+} and i_{x-} are obtained as

$$I_{x-} = \frac{C_c C_{x-}}{C_{x+} + C_{x-} + C_c} \frac{dV_c}{dt} \tag{2.66}$$

$$I_{x+} = \frac{C_c C_{x+}}{C_{x+} + C_{x-} + C_c} \frac{dV_c}{dt} \tag{2.67}$$

Transfer function of a TIA in Laplace Domain is

$$G_{TIA}(s) = -\frac{R_{TIA}}{1 + R_{TIA} C_{TIA} s} \tag{2.68}$$

If R_{TIA} is chosen in the order of mega ohms, equation (2.68) can be approximated as

$$G_{TIA}(s) = -\frac{1}{C_{TIA}s} \tag{2.69}$$

Taking Laplace transforms of equations (2.66), (2.67) and using the transfer functions of TIA given in (2.69), obtained expressions for V_{x+} and V_{x-} are given in equations (2.70) and (2.71) below.

$$V_{x-} = I_{x-}\left(-\frac{1}{C_{TIA}s}\right) = -\frac{C_c C_{x-}}{\left(C_{x+} + C_{x-} + C_c\right)\left(C_{TIA}\right)} V_c \tag{2.70}$$

$$V_{x+} = I_{x+}\left(-\frac{1}{C_{TIA}s}\right) = -\frac{C_c C_{x+} R_z}{\left(C_{x+} + C_{x-} + C_c\right)\left(C_{TIA}\right)} V_c \tag{2.71}$$

Then at the instrumentation amplifier stage differential reading voltage is obtained as

$$\Delta V_x = V_{x-} - V_{x+} = \left(\frac{C_c R_z V_c}{\left(C_{x+} + C_{x-} + C_c\right)\left(C_{TIA}\right)}\right)\left(C_{x+} - C_{x-}\right) \tag{2.72}$$

Finally, applying modulation to differential reading signal and feeding the resulting signal low pass filter, position measuring signal along x axis (V_x) is obtained as

$$V_x = V_{x-} - V_{x+} = \frac{1}{2}\left(\frac{C_c V_c}{\left(C_{x+} + C_{x-} + C_c\right)\left(C_{TIA}\right)}\right)\left(C_{x+} - C_{x-}\right) \tag{2.73}$$

2.3.4.2 Capacitive Detection Model for z-axis Movement

As explained in section 2.2.1.2 and given in equation (2.8), z- axis motion detection electrode pairs are used in a differential reading configuration. This capacitance configuration together with its front-end circuit is given in Figure 17 below.

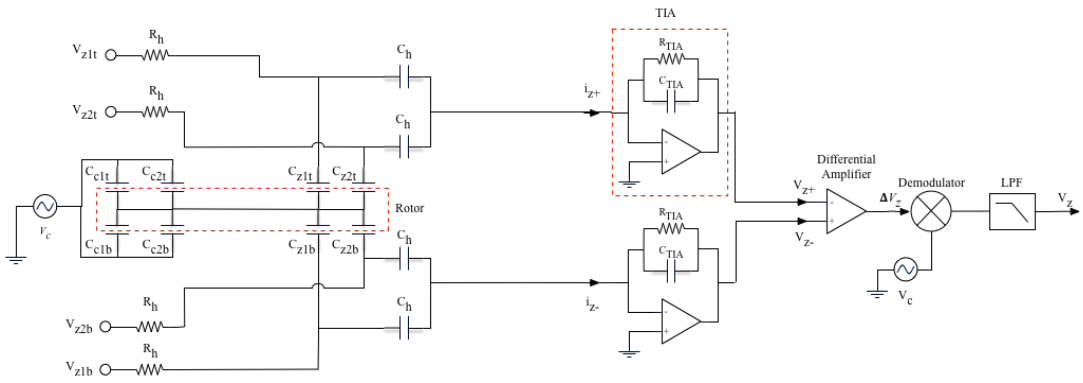

Figure 17 Electrode configuration for z axis translational motion detection and its reading circuit

Operation principle of the detection mechanism is same as x-axis translational motion detection mechanism, explained in section 2.3.4.1. Similarly, assuming $R_h >> (1/\omega_{carrier} C_h)$, approximated capacitance model and its compact form is given in Figure 18 below.

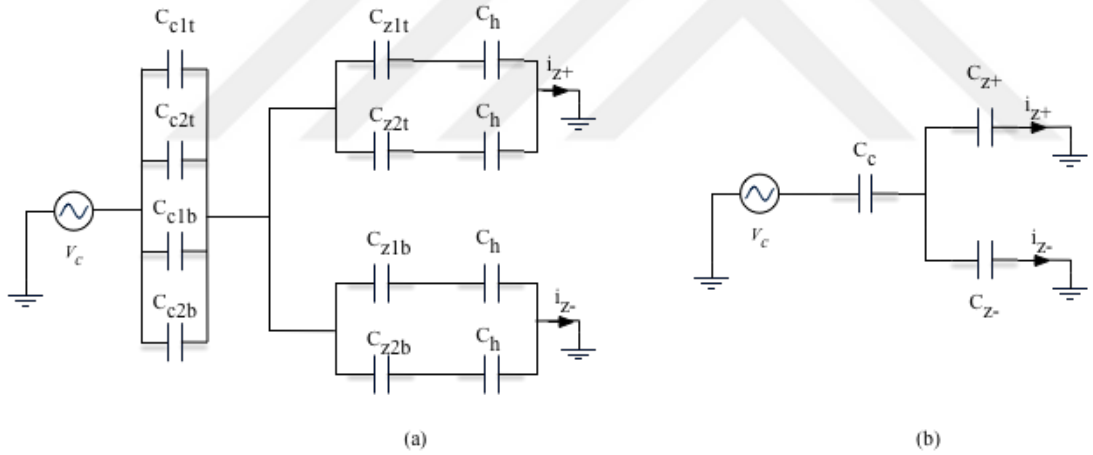

Figure 18 Approximated z-lateral motion capacitance reading model. (b) Compact representation of approximated model

For the capacitance model of z-axis translational motion detection, equations (2.64) and (2.65) change as

$$C_{z+} = \frac{C_{z1t} C_h}{C_{z1t} + C_h} + \frac{C_{z2t} C_h}{C_{z2t} + C_h} \tag{2.74}$$

$$C_{z-} = \frac{C_{z1b}C_h}{C_{z1b}+C_h} + \frac{C_{z2b}C_h}{C_{z2b}+C_h} \tag{2.75}$$

The rest of the model is exactly the same as x-axis translational model. Applying the same procedure, z-axis translational position detection signal is found as

$$V_z = \frac{1}{2}\left(\frac{C_c V_c}{\left(C_{z+}+C_{z-}+C_c\right)\left(C_{TIA}\right)}\right)\left(C_{z+}-C_{z-}\right) \tag{2.76}$$

2.3.4.3 Capacitive Detection Model for Out of Plane Rotations

Capacitive detection mechanism is exactly same for x-axis out of plane rotations and y-axis out of plane rotations. Therefore, in that section capacitance detection model only for x-axis rotation is presented. Capacitance configurations of x-out of plane rotation electrodes are given in (2.9). This detection configuration along with its readout circuitry are represented in Figure 19.

Using the similar assumptions utilized in sections 2.3.4.1 and 2.3.4.2 approximated capacitance model and its compact representation is shown in Figure 20 above.

For the detection model of that motion, equations (2.64) and (2.65) become

$$C_{rx+} = \frac{C_{rx-1t}C_h}{C_{rx-1t}+C_h} + \frac{C_{rx-2t}C_h}{C_{rx-2t}+C_h} + \frac{C_{rx+1b}C_h}{C_{rx+1b}+C_h} + \frac{C_{rx+2b}C_h}{C_{rx+2b}+C_h} \tag{2.77}$$

$$C_{rx-} = \frac{C_{rx+1t}C_h}{C_{rx+1t}+C_h} + \frac{C_{rx+2t}C_h}{C_{rx+2t}+C_h} + \frac{C_{rx-1b}C_h}{C_{rx-1b}+C_h} + \frac{C_{rx-2b}C_h}{C_{rx-2b}+C_h} \tag{2.78}$$

The rest of the model is exactly the same as x-axis translational model. Applying the same procedure, x-axis rotational position detection signal is found as

$$V_{rx} = \frac{1}{2}\left(\frac{C_c V_c}{\left(C_{rx+}+C_{rx-}+C_c\right)\left(C_{TIA}\right)}\right)\left(C_{rx+}-C_{rx-}\right) \tag{2.79}$$

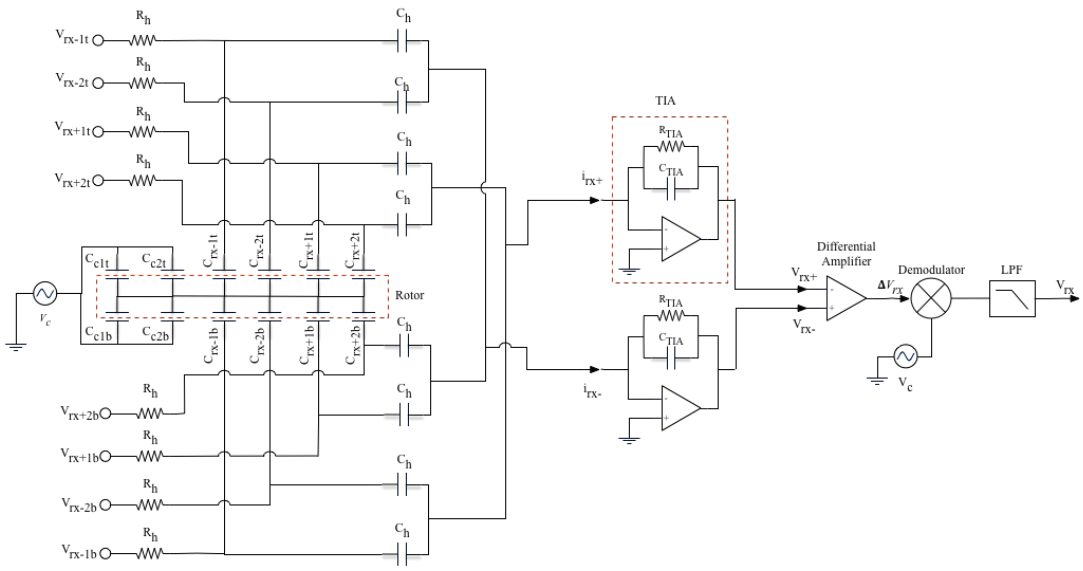

Figure 19 Electrode configuration for x axis rotational motion detection and its reading circuit

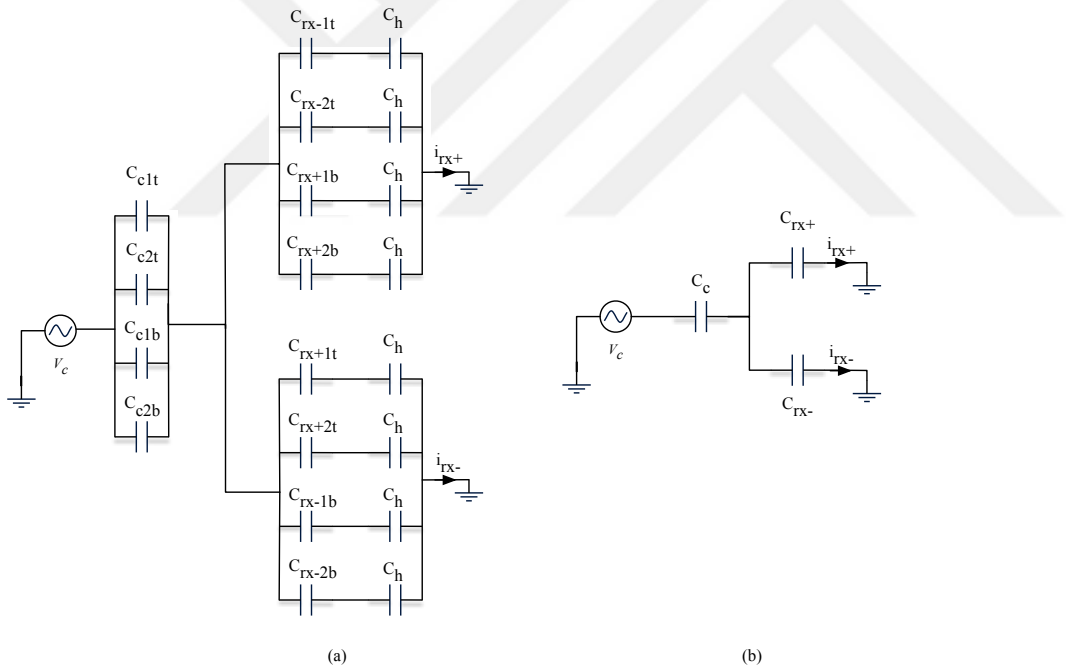

Figure 20 (a) Approximated x-axis rotational motion capacitance reading model. (b) Compact representation of approximated model

2.4 Summary

In this chapter, required electrode configuration for levitation is explained in Section 2.1. After that in Section 2.2, electrodes on bottom and top stator defined and their utilization as an actuator and a position detector for each axis are explained. Starting from Section 2.3 mathematical models for the proposed device are derived. Firstly in Section 2.3.1 change of capacitances due to rotor motion are described. Following that in Section 2.3.2, mathematical models for actuation mechanisms are found. After that dynamics equations of motion of the rotor along 5 axes are obtained in Section 2.3.3. Finally, in Section 2.3.4, capacitive detection models for each 5 axis are discussed.

CHAPTER 3

CONTROLLER DESIGN AND SIMULATIONS

In this chapter, controller design to ensure stable levitation and closed loop Simulink simulation of the proposed device are presented. As discussed in Section 2.3.3.2, air between small gaps behaves as spring and damper. Those effects change the behavior of the dynamic system depending on the ambient pressure. Therefore, behavior of the device both in atmospheric and in vacuum conditions are represented. For that purpose, firstly in Section 3.1, system parameters (mass, inertia, damping and stiffness) are calculated for controller design. Following that controllers for the motion of the rotor along 5 axes are designed for both atmospheric and vacuum operating conditions, in Section 3.2. Thirdly in Section 3.3, closed loop Simulink simulations both in air and vacuum are given. Finally in Section 3.4, summary of the chapter is presented.

3.1 System Parameters

In order to design controllers, system parameters need to be calculated. In that section mass and inertia of the rotor is found using the geometrical parameters listed in Table 1, in Section 2.2.2. Moreover, damping and stiffness acting on the system need to be calculated using the models explained in Section 2.3.3.2.

Volume of the rotor can be calculated as

$$V_r = t\left[\pi r_r^{\,2} - \left(\begin{array}{l} \frac{\pi}{3}\left(r_{2A}^{\,2} - r_{1A}^{\,2}\right) + \frac{\pi}{3}\left(r_{2B}^{\,2} - r_{1B}^{\,2}\right) + 180\frac{\pi}{360}\left(r_{2act}^{\,2} - r_{1act}^{\,2}\right) \\ \sum_{n=1}^{6}\left(\frac{\alpha_{2bal,n} - \alpha_{1bal,n}}{2}\right)\left(r_{2bal,n}^{\,2} - r_{1bal,n}^{\,2}\right) \end{array}\right)\right] \tag{3.1}$$

Then using the density of silicon, mass of the rotor is found as

$$m = \rho V_r = 59.27 \cdot 10^{-6}\, kg \tag{3.2}$$

Secondly, in order to find inertia of rotor, let write general expression, which gives inertia of a circular sector, which has inner/outer radius of r_1/r_2 and starting/ending angle of θ_1/θ_2.

$$\begin{aligned} I_{xx}\left(r_1, r_2, \theta_1, \theta_2\right) &= \int y^2\, dm = \rho t \int_{\theta_1}^{\theta_2}\int_{r_1}^{r_2} (r\sin\theta)^2\, r\, dr\, d\theta \\ &= \rho t\left(\frac{r_2^{\,4} - r_1^{\,4}}{4}\right)\left(\frac{\theta_2 - \theta_1}{2} - \frac{\sin 2\theta_2 - \sin 2\theta_1}{4}\right) \end{aligned} \tag{3.3}$$

$$\begin{aligned} I_{yy}\left(r_1, r_2, \theta_1, \theta_2\right) &= \int x^2\, dm = \rho t \int_{\theta_1}^{\theta_2}\int_{r_1}^{r_2} (r\cos\theta)^2\, r\, dr\, d\theta \\ &= \left(\frac{r_2^{\,4} - r_1^{\,4}}{4}\right)\left(\frac{\theta_2 - \theta_1}{2} + \frac{\sin 2\theta_2 - \sin 2\theta_1}{4}\right) \end{aligned} \tag{3.4}$$

Then using equations (3.3) and (3.4) inertia of the disk about x and y axis is found as

$$I_{xx/yy} = I_{xx/yy}\left(0, r_r, 0, 2\pi\right) - \left(\begin{array}{l} I_{xx/yy}\left(r_{1A}, r_{2A}, 0, \frac{2\pi}{3}\right) + I_{xx/yy}\left(r_{1B}, r_{2B}, \frac{2\pi}{3}, \frac{4\pi}{3}\right) \\ + \sum_{n=1}^{180} I_{xx/yy}\left(r_{1act}, r_{2act}, \frac{(n-1)\pi}{180}, \frac{n\pi}{180}\right) \\ + \sum_{n=1}^{6} I_{xx/yy}\left(r_{1bal,n}, r_{2bal,n}, \alpha_{1bal,n}, \alpha_{2bal,n}\right) \end{array}\right) \tag{3.5}$$

Inserting numerical values gives,

$$I_{xx} = I_{yy} = 1820.7\, \mu g \cdot m^2 \tag{3.6}$$

Finally, let us calculate damping and stiffness parameters. As mentioned at the beginning of the chapter, behavior of the system changes significantly depending on operation pressure. Firstly, for operation in atmospheric conditions, i.e. P=1 atm (101 kPa) stiffness and damping coefficients are found using equations (2.53), (2.54), (2.55), (2.56) and (2.57). Note that rotor is assumed to be oscillating about its nominal position at 20 Hz. Air properties are taken from [40]. Results are represented below.

$$k_{z,air} = 607.5\, N/m \tag{3.7}$$

$$b_{z,air} = 342.4\, N \cdot s/m \tag{3.8}$$

$$k_{\phi,air} = k_{\theta,air} = 3.88 \cdot 10^{-2}\, N/rad \tag{3.9}$$

$$b_{\phi,air} = b_{\theta,air} = 2.19 \cdot 10^{-2}\, N/rad \tag{3.10}$$

$$b_{x,air} = b_{y,air} = 2.92 \cdot 10^{-4}\, N \cdot s/m \tag{3.11}$$

Secondly, for operation in vacuum at level of P=0.5 Pa, it is assumed that all the surrounding air molecules are pumped out. Therefore, for vacuum conditions damping and stiffness coefficients are taken as zero.

3.2 Controller Design

In order to achieve stable hovering of the rotor, motion of the rotor in 5 axes should be controlled utilizing a closed loop controller strategy. As explained previously in section 2.2, there are dedicated electrode structures to control the motion of the rotor along each axis. However, those specific motion control electrodes may generate unintended forces/moments along other axes depending on the position of the rotor as stated in section 2.3. For controller design, it is assumed that rotor motion is restricted along all axes other than axis of interest. Therefore, it is assumed that dedicated motion control electrodes generate forces only along the axis of interest. Moreover, system assumed to be linear time invariant (LTI). Nonlinear equations derived in section 2.3 are linearized by taking the linear terms of its Taylor series

expansion. To determine the controller parameters, root locus techniques with following analytical design equations, from [41] are used.

$$K_p = \frac{-\sin(\beta+\psi)}{\left|G_p(s_1)H(s_1)\right|\sin\beta} - \frac{2K_i\cos\beta}{|s_1|} \tag{3.12}$$

$$K_d = \frac{\sin\psi}{|s_1|\left|G_p(s_1)H(s_1)\right|sin\beta} + \frac{K_i}{|s_1|^2} \tag{3.13}$$

where, s_1 is the desired closed loop pole location, $G_p(s)H(s)$ is the open loop transfer function of the system, and angles β & ψ are defined as

$$s_1 = |s_1|e^{j\beta}$$

$$G_p(s_1)H(s_1) = \left|G_p(s_1)H(s_1)\right|e^{j\psi}$$

In the design procedure, K_i is selected depending on the steady state requirement. Desired closed loop pole location is selected by trial & error such that system has fast response with minimum possible oscillations while resulting controller parameters can be implemented by using on the shelf analog electronic components.

3.2.1 Controller Design for Lateral Motion

System dynamics for translational motion of rotor along x and y direction are the same. Therefore, in that section controller design procedure for x axis lateral motion is represented only. Designed controller is also valid for y-axis translational motion control.

As stated in Section 2.2.1, lateral motion electrodes labeled as x+1 & x+2 and x-1 & x-2 are used for both actuation and detection of x-axis translational motion of rotor. Represented overlap area expression in equation (2.31) in section 2.3.1.2, is quite nonlinear even if the motion of the rotor along y axis is assumed to be zero. Therefore, for controller design overlap area expression will be further simplified by

assuming overlap area between rotor and stator increases radially as shown in the figure below.

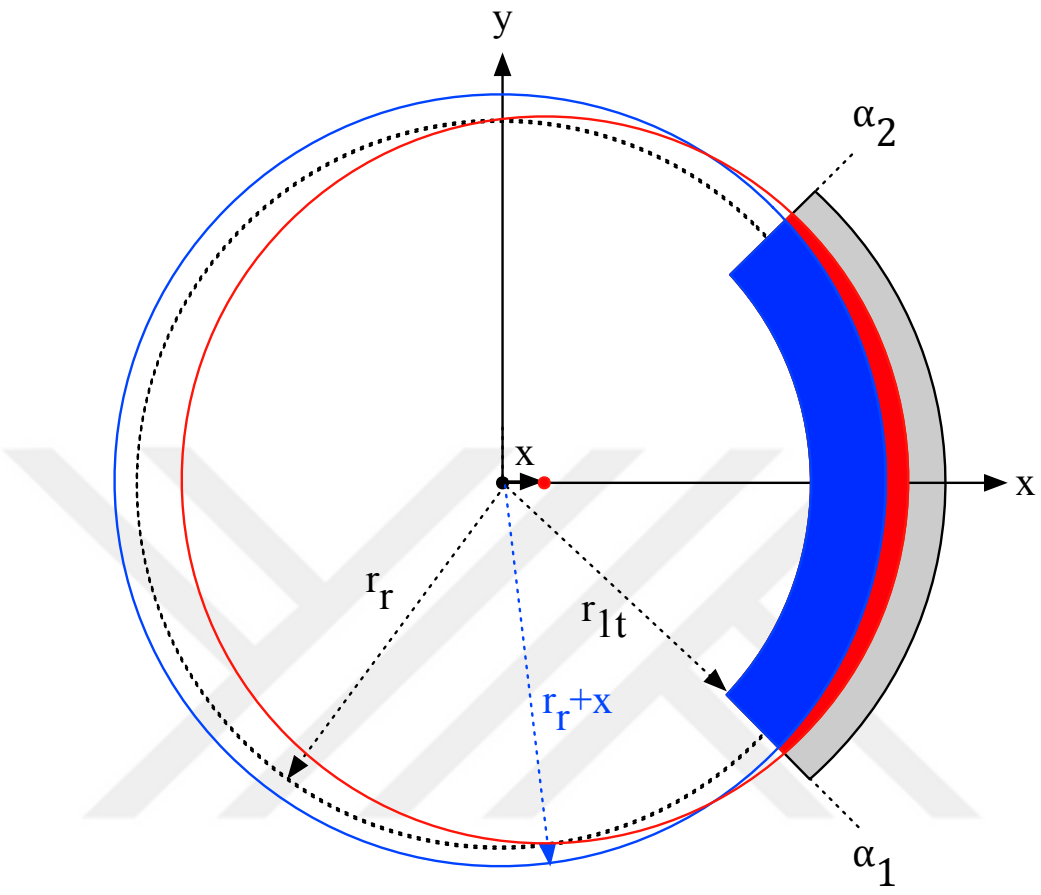

Figure 21 Simplified overlap area vs actual overlap area

In Figure 21, blue shaded area shows the simplified overlap area, while red shaded areas neglected portions of the overlap area due to the simplification explained above. Using that simplification on the overlap area, capacitance expression for a bottom/top lateral motion electrode located on +x direction reduces to

$$\tilde{C}_{l+,b/t}(x) = \varepsilon \frac{\alpha_l \left(\left(r_r + x \right)^2 - r_{1l}^{\ 2} \right)}{2 z_o} \tag{3.14}$$

Similarly capacitance expression for bottom/top lateral motion electrode located on –x direction reduces to

$$\tilde{C}_{l-,b/t}(x)=\varepsilon\frac{\alpha_l\left(\left(r_r-x\right)^2-{r_{1l}}^2\right)}{2z_o} \tag{3.15}$$

Using above equations in equation (2.2), electrostatic force generated by a bottom/top stator lateral motion electrode is found as

$$\tilde{F}_{l+,xb/t}(x,V)=\frac{1}{2}\frac{\partial\tilde{C}_{l,xb/t}}{\partial x}V^2=\frac{\varepsilon\alpha_l\left(r_r+x\right)}{2d}V^2 \tag{3.16}$$

$$\tilde{F}_{l-,xb/t}(x,V)=\frac{1}{2}\frac{\partial\tilde{C}_{l,xb/t}}{\partial x}V^2=-\frac{\varepsilon\alpha_l\left(r_r-x\right)}{2d}V^2 \tag{3.17}$$

In total, there are 4 lateral motion electrodes on each stator, which are dedicated to control the position of rotor along x-axis as explained section 2.2.1.1. Total control force along x-axis acting on the rotor by those electrodes is found by using equation (3.16) and electrode voltage configuration given in Figure 10 as

$$\begin{aligned}\tilde{F}_{x,fb}(x)=&2\tilde{F}_{l+,xb}\left(x,V_b+V_{fb,x}\right)+2\tilde{F}_{l+,xt}\left(x,V_b+V_{fb,x}\right)\\&+2\tilde{F}_{l-,xb}\left(x,V_b-V_{fb,x}\right)+2\tilde{F}_{l-,xt}\left(x,V_b-V_{fb,x}\right)\end{aligned} \tag{3.18}$$

Inserting the numerical values of geometric parameters of related electrodes into equation (3.18),

$$\tilde{F}_{x,fb}\left(x,V_{fb,x}\right)=\frac{26\pi}{3}\varepsilon\left(113V_bV_{fb,x}+5000{V_b}^2x+5000{V_{fb,x}}^2x\right) \tag{3.19}$$

Above expression is linearized by taking the linear terms of its Taylor series expansion around rotor nominal position, i.e. x=0, $V_{fb,x}$=0.

$$\bar{F}_{x,fb}\left(x,V_{fb,x}\right)=\frac{26\pi}{3}\varepsilon\left(113V_bV_{fb,x}+5000{V_b}^2x\right) \tag{3.20}$$

Let denote the equation (3.20) as

$$\bar{F}_{x,fb}\left(x,V_{fb,x}\right)=k_{Vfb,x}V_{fb,x}+k_{el,x}x \tag{3.21}$$

Then equation of motion of the rotor along x-axis can be written as

$$ms^2X + bsX = k_{Vfb,x}V_{fb,x} + k_{el,x}X$$

$$\left(ms^2 + bs - k_{el,x}\right)X = k_{Vfb,x}V_{fb,x} \tag{3.22}$$

Note that value of b change depending on the operation conditions as explained in Section 3.1.

Secondly, let find a linear expression for capacitive detection function, which is obtained in section 2.3.4.1. Since it is assumed that all of the motions other than x-axis are restricted, capacitance between a carrier electrode and rotor is constant and when the rotor is at equilibrium it is equal to

$$\tilde{C}_{c1t} = \tilde{C}_{c2t} = \tilde{C}_{c1b} = \tilde{C}_{c2b} = \varepsilon\frac{\alpha_c\left(r_{2c}{}^2 - r_{1c}{}^2\right)}{2z_o} \tag{3.23}$$

Then equation (2.63) becomes

$$\tilde{C}_c = 4\varepsilon\frac{\alpha_c\left(r_{2c}{}^2 - r_{1c}{}^2\right)}{2z_o} \tag{3.24}$$

If C_h is large compered to lateral motion sense capacitances, equations (2.64) and (2.65) can be approximated as

$$C_{x+} = C_{x+1t} + C_{x+2t} + C_{x+1b} + C_{x+1b} \tag{3.25}$$

$$C_{x-} = C_{x-1t} + C_{x-2t} + C_{x-1b} + C_{x-1b} \tag{3.26}$$

Using simplified capacitance model obtained in equation (3.15) in equations (3.25) and (3.26)

$$\tilde{C}_{x+}(x) = 4\varepsilon\frac{\alpha_l\left(\left(r_r + x\right)^2 - r_{1l}{}^2\right)}{2z_o} \tag{3.27}$$

$$\tilde{C}_{x-}(x) = 4\varepsilon\frac{\alpha_l\left(\left(r_r - x\right)^2 - r_{1l}{}^2\right)}{2z_o} \tag{3.28}$$

Substituting equations (3.24), (3.27) and (3.28) and numerical values of geometric parameters of electrodes into equation (2.73) simplified version for ΔV_x is obtained as

$$\tilde{V}_x = \varepsilon \frac{17.7721 \cdot 10^{-3} V_c x}{C_{TIA}\left(x^2 + 19.3403 \cdot 10^{-6}\right)} \tag{3.29}$$

Similarly this equation is linearized taking the linear terms of its Taylor series expansion about the nominal position of rotor.

$$\bar{V}_x = \frac{17.7721 \cdot 10^{-3} V_c \varepsilon}{19.3403 \cdot 10^{-6} C_{TIA}} x \tag{3.30}$$

Let denote equation (3.30) as

$$\Delta \bar{V}_x = H_x x \tag{3.31}$$

Using equations (3.22) and (3.31) resulting closed loop block diagram of the system is represented in Figure 22 below.

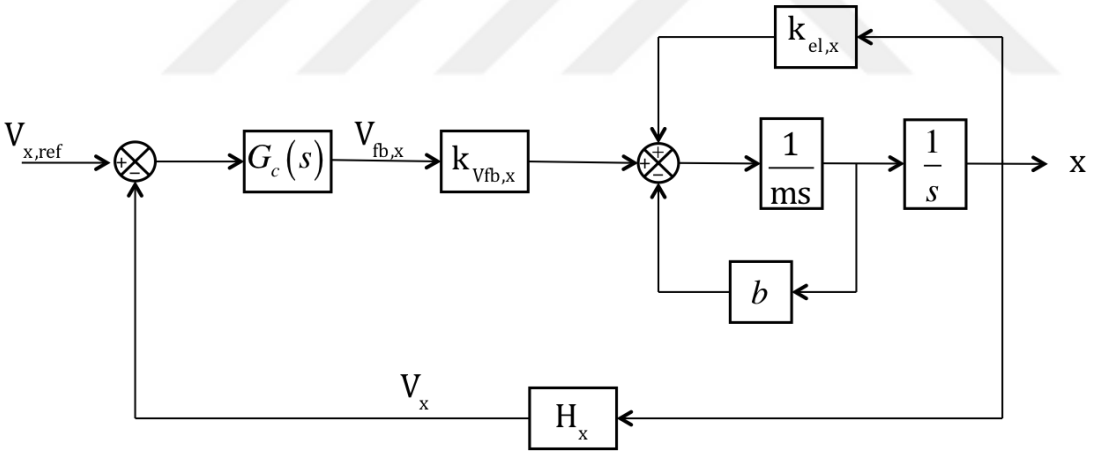

Figure 22 Block Diagram of the system for x axis lateral motion control

For a proportional control strategy, i.e. $G_c(s)=K_p$, root locus of the system, for air and vacuum operating conditions are drawn by using Matlab and it is represented in Figure 23 below.

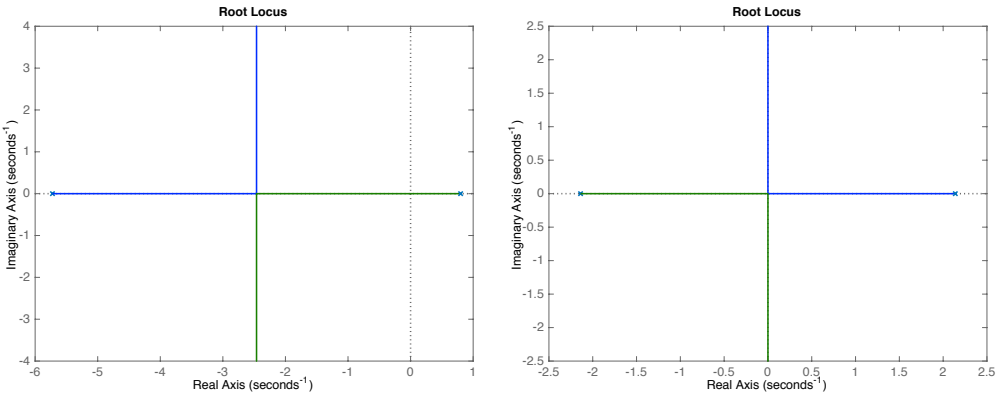

(a) (b)

Figure 23 Root locus of P-Controlled x-lateral motion systems. (a) operation in air, (b) operation in vacuum

As it can be seen in Figure 23 (a) above, when the system is operated in air, system can be stabilized with a P controller only. However, in order to have faster response, root locus of the system need to bend towards to left. A PD controller is enough for that purpose. Using the controller design procedure outlined in Section 3.1, dominant closed loop position is set as -200. Designed controller and reshaped root locus with the controller are represented in equation (3.32) and Figure 24, respectively.

For operation in vacuum on the other hand, closed loop system is marginally stable. Therefore, a proper controller needs to be designed. Similarly, in order to bend root locus towards left a PD controller is enough. Then using the procedure outlined in section 3.1 dominant closed loop pole location is set as -70. Resulting controller parameters and reshaped root locus with designed PID controller of the system is represented in equation (3.33) and Figure 25 respectively.

$$G_{c,x,air}(s) = 9.51 \cdot 10^3 + 93.9s = 9.51 \cdot 10^3 (1 + 9.88 \cdot 10^{-3} s) \tag{3.32}$$

$$G_{c,x,vac}(s) = 9.51 \cdot 10^3 + 95.1s = 9.51 \cdot 10^3 (1 + 1.00 \cdot 10^{-2} s) \tag{3.33}$$

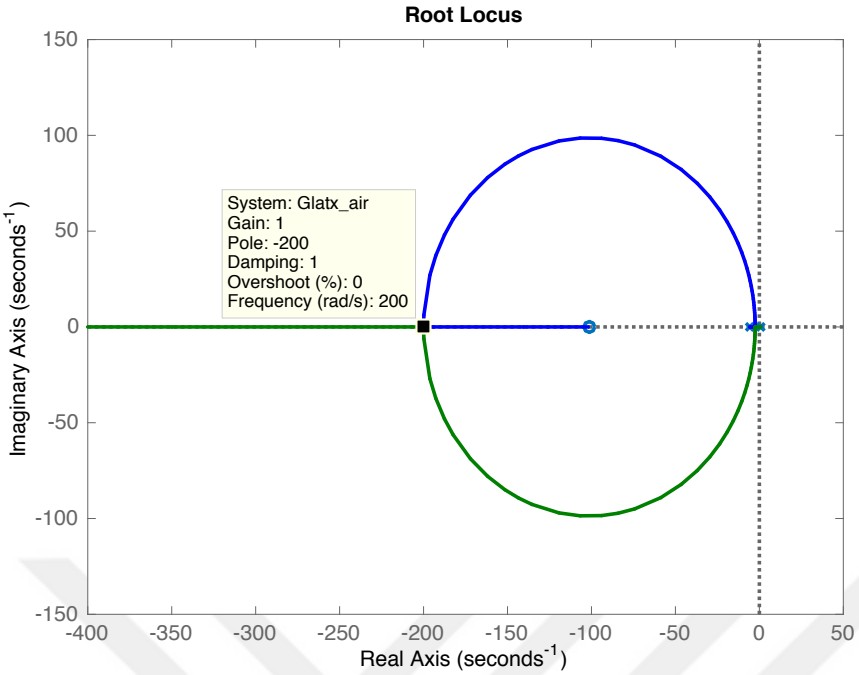

Figure 24 Root locus of PD-Controlled x-lateral motion system operated in air

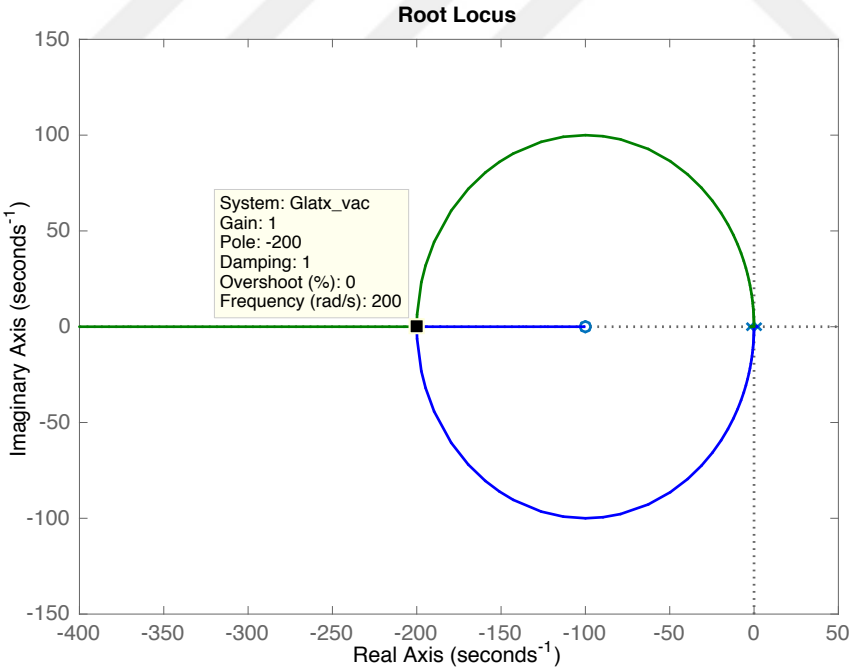

Figure 25 Root locus of PD-Controlled x-lateral motion system operated in vacuum

Notice that, since damping induced by the air is small for lateral motion, resulting control parameters and root loci for both systems are almost equal.

3.2.2 Controller Design for Levitation

In order to control motion of the rotor along z-axis, i.e. for levitation, levitation electrodes and out of plane rotation electrodes are utilized together as explained in section 2.2.1. If the motion of the rotor is assumed to be restricted other than z axis, capacitance expression for those electrodes given in equations (2.24) and (2.25) reduces to

$$\tilde{C}_{op,b}\left(z,r_1,r_2,\alpha_s\right)=\varepsilon\frac{\alpha_s\left(r_2^{\,2}-r_1^{\,2}\right)}{2\left(z_o+z\right)} \tag{3.34}$$

$$\tilde{C}_{op,t}\left(z,r_1,r_2,\alpha_s\right)=\varepsilon\frac{\alpha_s\left(r_2^{\,2}-r_1^{\,2}\right)}{2\left(z_o-z\right)} \tag{3.35}$$

where, r_1 is inner diameter, r_2 is outer diameter and α_s is sector angle of electrode in interest. Similarly, using equations (3.34) and (3.35) in equation (2.2), electrostatic force along z direction, generated by a electrode located on bottom and top stator is found as

$$\tilde{F}_{op,zb}\left(x,V\right)=\frac{1}{2}\frac{\partial\tilde{C}_{op,b}}{\partial z}V^2=-\frac{\varepsilon\alpha_s\left(r_2^{\,2}-r_1^{\,2}\right)}{4\left(z_o+z\right)^2}V^2 \tag{3.36}$$

$$\tilde{F}_{op,zt}\left(z,V,\alpha_s,r_1,r_2\right)=\frac{1}{2}\frac{\partial\tilde{C}_{op,t}}{\partial z}V^2=\frac{\varepsilon\alpha_s\left(r_2^{\,2}-r_1^{\,2}\right)}{4\left(z_o-z\right)^2}V^2 \tag{3.37}$$

For control of rotor position along z-axis, there are 2 levitation electrodes and 8 out of plane rotational motion electrodes on each stator. Total electrostatic force generated along z direction is obtained using the geometric parameters of those electrodes and electrode voltage configuration given in Figure 10, in equations (3.36) and (3.37) as

$$\tilde{F}_{z,el}(x) = 2\tilde{F}_{op,zb}\left(z, V_b - V_{fb,z}, \alpha_z, r_{1z}, r_{2z}\right) + 8\tilde{F}_{op,zb}\left(z, V_b - V_{fb,z}, \alpha_{opr}, r_{1opr}, r_{2opr}\right)$$
$$+2\tilde{F}_{op,zt}\left(z, V_t + V_{fb,z}, \alpha_z, r_{1z}, r_{2z}\right) + 8\tilde{F}_{op,zt}\left(z, V_t + V_{fb,z}, \alpha_{opr}, r_{1opr}, r_{2opr}\right) \quad (3.38)$$

Inserting numerical values of geometrical parameters of related electrodes into equation (3.38),

$$\tilde{F}_{z,fb}\left(z, V_{fb,z}\right) = \frac{5531\varepsilon\pi}{45\cdot 10^7}\left(\left(\frac{V_t + V_{fb,z}}{z_o - z}\right)^2 - \left(\frac{V_b - V_{fb,z}}{z_o + z}\right)^2\right) \quad (3.39)$$

Above expression is linearized by taking the linear terms of its Taylor series expansion around rotor nominal position, i.e. z=0, $V_{fb,z}$=0.

$$\overline{F}_{z,fb}\left(z, V_{fb,z}\right) = \frac{5531\varepsilon\pi}{45\cdot 10^7}\left(\frac{V_t^2 - V_b^2}{z_o^2} + \frac{2\left(V_t + V_b\right)}{z_o^2}V_{fb,z} + \frac{2\left(V_t^2 + V_b^2\right)}{z_o^3}z\right) \quad (3.40)$$

Using above expression, net force on the rotor given in equation (2.45) reduces to

$$\overline{F}_{z,net}\left(z, V_{fb,z}\right) = \frac{5531\varepsilon\pi}{45\cdot 10^7}\left(\frac{V_t^2 - V_b^2}{z_o^2} + \frac{2\left(V_t + V_b\right)}{z_o^2}V_{fb,z} + \frac{2\left(V_t^2 + V_b^2\right)}{z_o^3}z\right) - mg \quad (3.41)$$

Top stator bias voltage (V_t) and bottom stator bias voltage (V_b) are set such that first term of equation (3.41) eliminates weight of rotor (*mg*), when the rotor is at its nominal position. Then equation (3.41) reduces to

$$\overline{F}_{z,net} = \frac{11062\varepsilon\pi}{45\cdot 10^7}\frac{\left(V_t + V_b\right)}{\left(20\cdot 10^{-6}\right)^2}V_{fb,z} + \frac{11062\varepsilon\pi}{45\cdot 10^7}\frac{\left(V_t^2 + V_b^2\right)}{\left(20\cdot 10^{-6}\right)^3}z \quad (3.42)$$

Let denote equation (3.42) as

$$\overline{F}_{z,net}\left(z, V_{fb,z}\right) = k_{Vfb,z}V_{fb,z} + k_{el,z}z \quad (3.43)$$

Then equation of motion of the rotor along z axis can be written as

$$ms^2Z + bsZ + kZ = k_{Vfb,z}V_{fb,z} + k_{el,z}Z$$

$$\left(ms^2 + bs + k - k_{el,z}\right)Z = k_{Vfb,z}V_{fb,z} \quad (3.44)$$

Note that values of b and k change depending on operating conditions as explained in Section 3.1

After that let find a linear expression for capacitive detection transfer function. A nonlinear expression for that function is already obtained in Section 2.3.4.2 and represented in equation (2.76). Similarly, using reduced capacitance model given in equations (3.34) and (3.35) in equation (2.63), capacitances of carrier electrodes can be simplified as

$$\tilde{C}_c = \frac{2\alpha_c \varepsilon \left({r_{2c}}^2 - {r_{1c}}^2 \right) z_o}{{z_o}^2 - z^2} \tag{3.45}$$

Similarly, choosing a large C_h compered to levitation sense capacitances, equations (2.74) and (2.75) can be approximated as

$$C_{z+} = C_{z1t} + C_{z2t} \tag{3.46}$$

$$C_{z-} = C_{z1b} + C_{z2b} \tag{3.47}$$

Then using restricted capacitance model obtained in equations (3.34) and (3.35), in above equations

$$\tilde{C}_{z+} = \varepsilon \frac{\alpha_z \left({r_{2z}}^2 - {r_{1z}}^2 \right)}{\left(z_o - z \right)} \tag{3.48}$$

$$\tilde{C}_{z-} = \varepsilon \frac{\alpha_z \left({r_{2z}}^2 - {r_{1z}}^2 \right)}{\left(z_o + z \right)} \tag{3.49}$$

Finally, substituting equations (3.45), (3.48) and (3.49) and geometrical values of geometric parameters of electrodes into equation (2.76), simplified version for z-axis translational motion detection signal is found as

$$\tilde{V}_z = \varepsilon \frac{28593.6z}{C_{TIA}\left(1 - 2.5 \cdot 10^9 z^2\right)} \tag{3.50}$$

Then equation (3.50) is linearized around the nominal position of the rotor, i.e. z=0, by taking the linear terms of its Taylor series expansion around z=0. Resulting expression is given in equation (3.51) below.

$$\bar{V}_z = \frac{28593.6 V_c \varepsilon}{C_{TIA}} z = H_z z \tag{3.51}$$

Using equations (3.44) and (3.51) closed loop block diagram of z-axis translation control is represented in Figure 26 below.

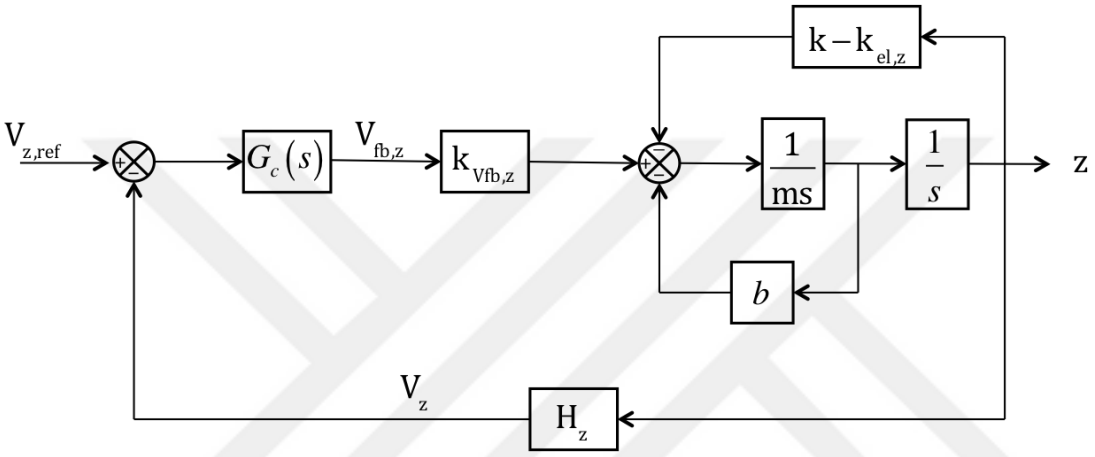

Figure 26 Block Diagram of the system for z-axis lateral motion control

For a proportional control strategy, i.e. $G_c(s)=K_p$ root loci of the system for both air and vacuum conditions are drawn by using Matlab and they are represented in Figure 27.

As it can be seen in Figure 27 (a), when the system operates in air system has stable closed loop poles. Therefore, P controller with a gain of 10000 is used as a controller. Note that similar to lateral motion control, transient response characteristics of the system can further be improved by adding a differentiator to the system. However, for that case required gains to reshape root locus are so high that it cannot be implemented using on the shelf analog components.

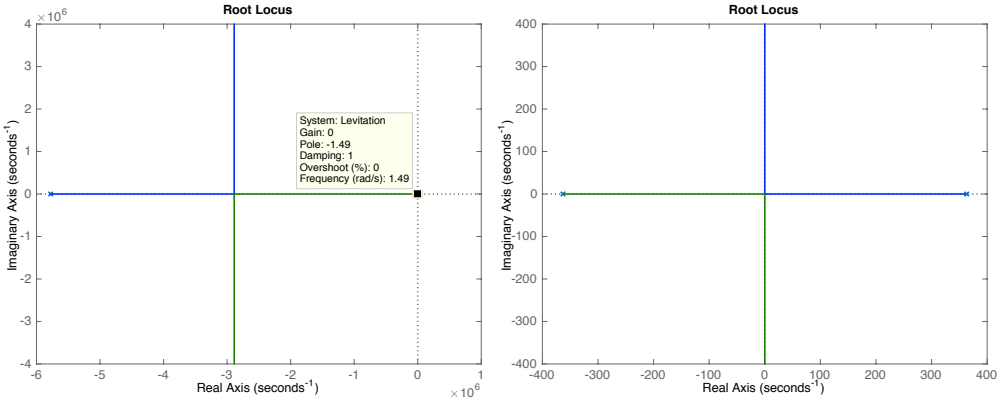

(a) (b)

Figure 27 Root locus of P-Controlled levitation control system. (a) Operated in air, (b) operated in vacuum

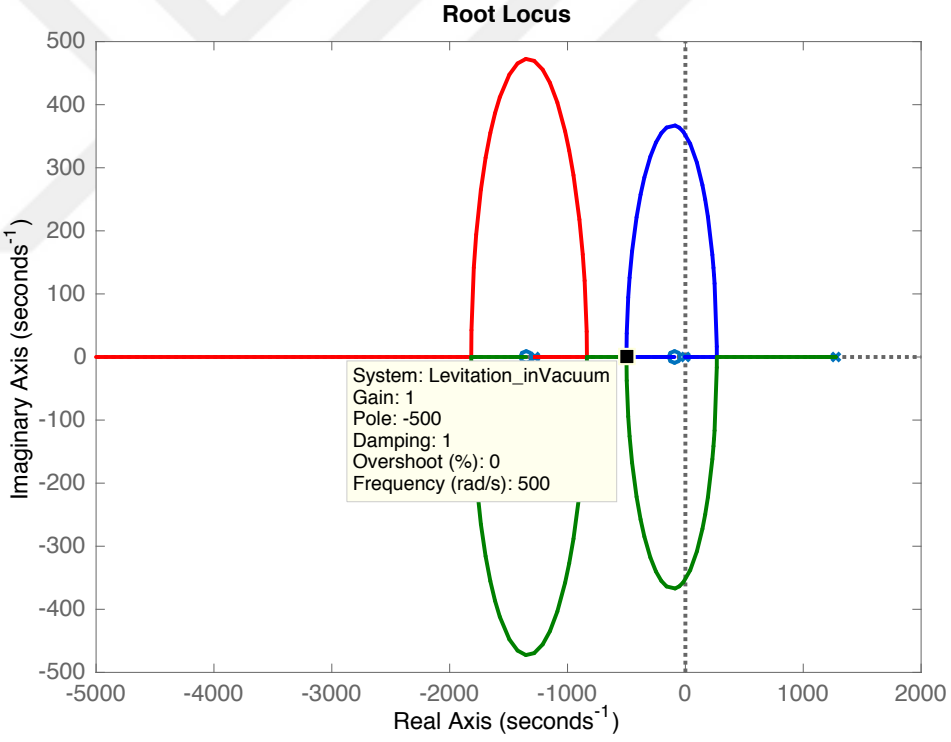

Figure 28 Root locus of PID-Controlled levitation control system in vacuum

For vacuum conditions, on the other hand, closed loop system is marginally stable, as it can be seen from Figure 27 (b). In order to bend root locus towards left, PD controller is enough. Moreover, to improve the steady state error characteristics of the closed loop system; an integrator can be added to controller. Therefore, a PID controller is designed. Similarly, applying the procedure outlined in Section 3.1, dominant closed loop is set as -500. Resulting controller parameters and root locus of the system in vacuum, reshaped by the PID controller are represented below.

$$G_{c,z,vac}(s) = 116.14 + \frac{10000}{s} + 8.05 \cdot 10^{-2} s = 116.14\left(1 + \frac{86.1}{s} + 6.93 \cdot 10^{-4}\right) \quad (3.52)$$

3.2.3 Controller Design for Out of Plane Rotational Motion

Similar to lateral motion dynamics, out of plane rotational dynamics about x and y axes are the same. Therefore, in that section controller design procedure for x axis rotational motion of rotor is represented, only. Designed controller is also valid for y-axis rotational motion control.

As explained in Section 2.2.1, x-axis rotational motion of the rotor is controlled using the electrodes labeled as rx+1 & rx+2 and rx-1 & rx-2 located on each stator. Similarly, assuming motion of the rotor is restricted other than x-axis rotation, capacitance expression of those electrodes given in equations (2.24) and (2.25) reduces to

$$\tilde{C}_{op,b}(\phi, r_1, r_2, \alpha_1, \alpha_2) = \varepsilon\left[\begin{array}{l} \frac{1}{2}\left(\frac{r_2^2 - r_1^2}{z_o}\right)(\alpha_2 - \alpha_1) - \frac{1}{3}\left(\frac{r_2^3 - r_1^3}{z_o^2}\right)(\cos\alpha_1 - \cos\alpha_2)\phi \\ + \frac{1}{4}\left(\frac{r_2^4 - r_1^4}{z_o^3}\right)\left(\frac{\alpha_2 - \alpha_1}{2} + \frac{\sin 2\alpha_2 - \sin 2\alpha_1}{4}\right)\phi^2 \end{array}\right] \quad (3.53)$$

$$\tilde{C}_{op,t}\left(\phi,r_1,r_2,\alpha_1,\alpha_2\right)= \varepsilon\left[\begin{array}{l}\frac{1}{2}\left(\frac{r_2^{\,2}-r_1^{\,2}}{z_o}\right)\left(\alpha_2-\alpha_1\right)+\frac{1}{3}\left(\frac{r_2^{\,3}-r_1^{\,3}}{z_o^{\,2}}\right)\left(\cos\alpha_1-\cos\alpha_2\right)\phi \\ +\frac{1}{4}\left(\frac{r_2^{\,4}-r_1^{\,4}}{z_o^{\,3}}\right)\left(\frac{\alpha_2-\alpha_1}{2}+\frac{\sin 2\alpha_2-\sin 2\alpha_1}{4}\right)\phi^2\end{array}\right] \tag{3.54}$$

where, r_1 is inner diameter, r_2 is outer diameter, α_1 and α_2 are starting and finishing angle of electrode in interest. After that, moment generated about x-axis is found substituting restricted capacitance expression given above in equation (2.36).

$$\tilde{M}_{op,\phi b}\left(z,\phi,\theta,r_1,r_2,\alpha_1,\alpha_2,V\right)= \frac{\varepsilon}{2}\left[\begin{array}{l}-\frac{1}{3}\left(\frac{r_2^{\,3}-r_1^{\,3}}{z_o^{\,2}}\right)\left(\cos\alpha_1-\cos\alpha_2\right)\phi \\ +\frac{1}{2}\left(\frac{r_2^{\,4}-r_1^{\,4}}{z_o^{\,3}}\right)\left(\frac{\alpha_2-\alpha_1}{2}+\frac{\sin 2\alpha_2-\sin 2\alpha_1}{4}\right)\phi\end{array}\right]V^2 \tag{3.55}$$

$$\tilde{M}_{op,\phi t}\left(\phi r_1,r_2,\alpha_1,\alpha_2,V\right)= \frac{\varepsilon}{2}\left[\begin{array}{l}\frac{1}{3}\left(\frac{r_2^{\,3}-r_1^{\,3}}{z_o^{\,2}}\right)\left(\cos\alpha_1-\cos\alpha_2\right) \\ +\frac{1}{2}\left(\frac{r_2^{\,4}-r_1^{\,4}}{z_o^{\,3}}\right)\left(\frac{\alpha_2-\alpha_1}{2}+\frac{\sin 2\alpha_2-\sin 2\alpha_1}{4}\right)\phi\end{array}\right]V^2 \tag{3.56}$$

Substituting geometrical parameters of each x-axis rotational motion control electrodes to equations (3.55) and (3.56), x-axis rotational motion control moment acting on the rotor is obtained as

$$\tilde{M}_{fb,\phi}\left(\phi,V_{fb,rx}\right)=113952\cdot\varepsilon\cdot\phi\left(\mathrm{V_b}^{\,2}+2\mathrm{V_{fb,rx}}^{\,2}+\mathrm{V_t}^{\,2}\right)+315.8\cdot\varepsilon\cdot\mathrm{V_{fb,rx}}\left(\mathrm{V_b}+\mathrm{V_t}\right) \tag{3.57}$$

Let linearize above expression by taking the linear terms of its Taylor series expansion around rotor nominal position, i.e. $\theta=0$, $V_{fb,rx}=0$. Resulting expression is given in equation (3.58) below.

$$\bar{M}_{fb,\phi}\left(\phi,V_{fb,rx}\right)=113952\cdot\varepsilon\left(\mathrm{V_b}^{\,2}+\mathrm{V_t}^{\,2}\right)\phi+315.8\cdot\varepsilon\left(\mathrm{V_b}+\mathrm{V_t}\right)V_{fb,rx} \tag{3.58}$$

Let denote above equation as

$$\bar{M}_{fb,\phi}\left(\phi, V_{fb,rx}\right) = k_{el,\phi}\phi + k_{Vfb,\phi}V_{fb,rx} \tag{3.59}$$

Then equation of motion of the rotor rotation about x-axis can be written as

$$ms^2\Phi + bs\Phi + k\Phi = k_{Vfb,rx}V_{fb,rx} + k_{el,\phi}\Phi$$

$$\left(ms^2 + bs + k - k_{el,\phi}\right)\Phi = k_{Vfb,rx}V_{fb,rx} \tag{3.60}$$

Note that values of b and k change depending on operating conditions as explained in Section 3.1

Secondly, let find a linear expression for capacitive detection transfer function, which is already obtained in Section 2.3.4.3 and represented in equation (2.79). For that purpose, firstly, let use the reduced capacitance model obtained in equations (3.53) and (3.54), in equation (2.63).

$$\tilde{C}_c = 2\left(\frac{r_{2c}^{\ 2} - r_{1c}^{\ 2}}{z_o}\right)\alpha_c + \left(\frac{r_{2c}^{\ 4} - r_{1c}^{\ 4}}{z_o^{\ 3}}\right)\left(\frac{\alpha_c}{2} + 3\sin\left(\alpha_{cs}\right) - \sin\left(2\alpha_c + \alpha_{cs}\right)\right) \tag{3.61}$$

Similarly, if C_h in equations (2.77) and (2.78), is chosen large compered to x axis rotational motion sense capacitances, those equations can be approximated as

$$C_{rx+} = C_{rx-1t} + C_{rx-2t} + C_{rx+1b} + C_{rx+2b} \tag{3.62}$$

$$C_{rx-} = C_{rx+1t} + C_{rx+2t} + C_{rx-1b} + C_{rx-2b} \tag{3.63}$$

Then using restricted capacitance model obtained in equations (3.53) and (3.54) in above equations

$$\tilde{C}_{rx+} = 2\left(\frac{r_{2op}^{\ 2} - r_{1op}^{\ 2}}{z_o}\right)\alpha_{op} + \frac{1}{3}\left(\frac{r_2^{\ 3} - r_1^{\ 3}}{z_o^{\ 2}}\right)\left(4\sin\left(\alpha_{ops}\right) - \sin\left(\alpha_{op} + \alpha_{ops}\right)\right)\phi \tag{3.64}$$

$$\tilde{C}_{rx-} = 2\left(\frac{r_{2op}^{\ 2} - r_{1op}^{\ 2}}{z_o}\right)\alpha_{op} + \frac{1}{3}\left(\frac{r_2^{\ 3} - r_1^{\ 3}}{z_o^{\ 2}}\right)\left(-4\sin\left(\alpha_{ops}\right) + \sin\left(\alpha_{op} + \alpha_{ops}\right)\right)\phi \tag{3.65}$$

Finally, substituting equations (3.61), (3.64), (3.65) and geometrical values of geometric parameters of control electrodes into equation (2.79), restricted version of x-axis rotational motion detection signal is obtained as

$$\tilde{V}_{rx} = \frac{26.5395 \cdot \varepsilon \cdot \phi \left(\phi^2 + 75.215 \cdot 10^{-6} \right) V_c}{\left(\phi^2 + 13.4142 \cdot 10^{-6} \right) C_{TIA}} \tag{3.66}$$

Linearizing above expression around nominal operation of the rotor,

$$\bar{V}_{rx} = \frac{148.81 \cdot \varepsilon \cdot V_c}{C_{TIA}} \phi = H_{rx} \phi \tag{3.67}$$

Using equations (3.59) and (3.67), closed loop block diagram of the system is given in Figure 29 below.

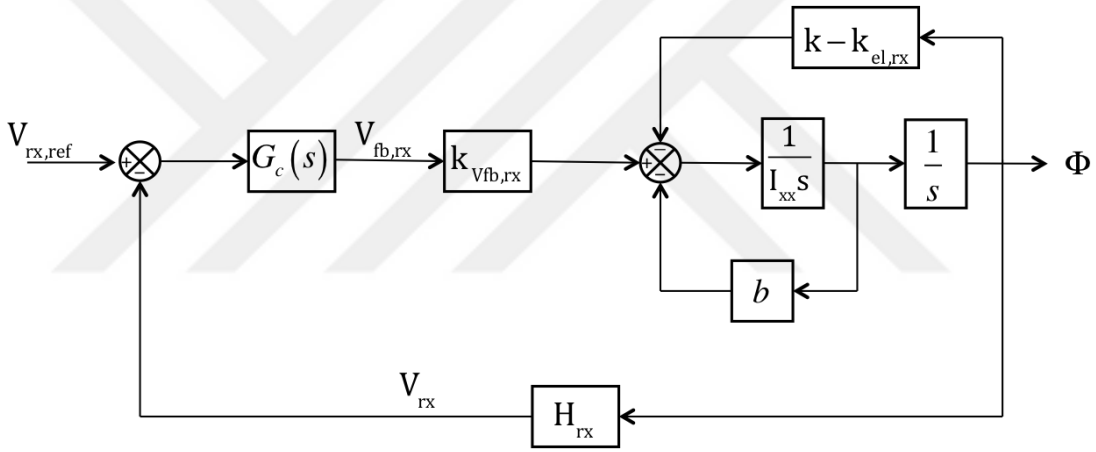

Figure 29 Block Diagram of the system for x-axis rotational motion control

For a proportional control strategy, i.e. $G_c(s)=K_p$ root loci of the air and vacuum operated systems are drawn by using Matlab and they are represented in Figure 30 below.

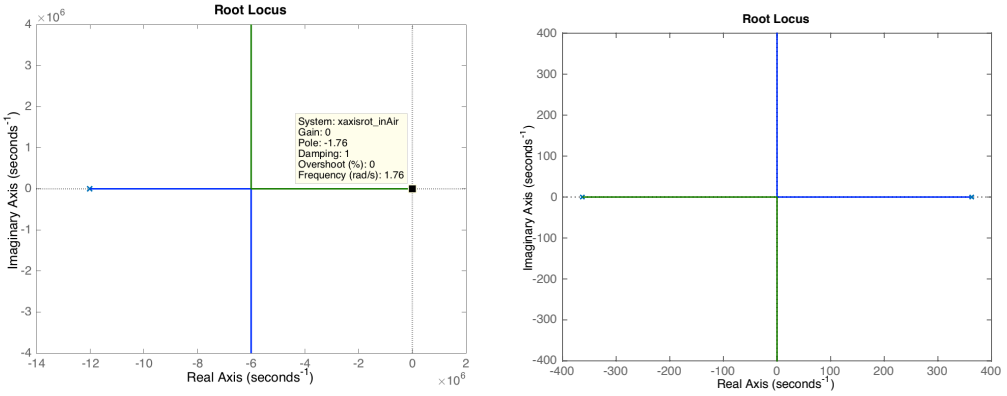

(a) (b)

Figure 30 Root locus of P-Controlled x-axis rotational motion control systems. (a) Operated in air, (b) Operated in vacuum

As it can be seen above in Figure 30 (a), when the system is operated in air, closed loop system can be stabilized without any oscillations by using a P controller only. Therefore, a proportional controller with a gain of 10000 is used as a controller. Similar to levitation controller system that operates in air, required gains to further improve transient characteristics of the system is too large to implement them using on the shelf analog components.

However, when the system is operated in vacuum, P-controlled system is marginally stable as it can be seen from Figure 30 (b). In order the bend root locus towards left, a PD control is required. Similarly, in order improve the steady state error characteristic at the same time a PID controller is designed. Implemented controller and reshaped root locus of the vacuum operated system are represented below in equation (3.68) and Figure 31 respectively.

$$G_{c,rx,vac}(s) = 2.28 \cdot 10^2 + \frac{10^4}{s} + 0.488s = 2.28 \cdot 10^2 \left(1 + \frac{43.88}{s} + 2.14 \cdot 10^{-3} s \right) \quad (3.68)$$

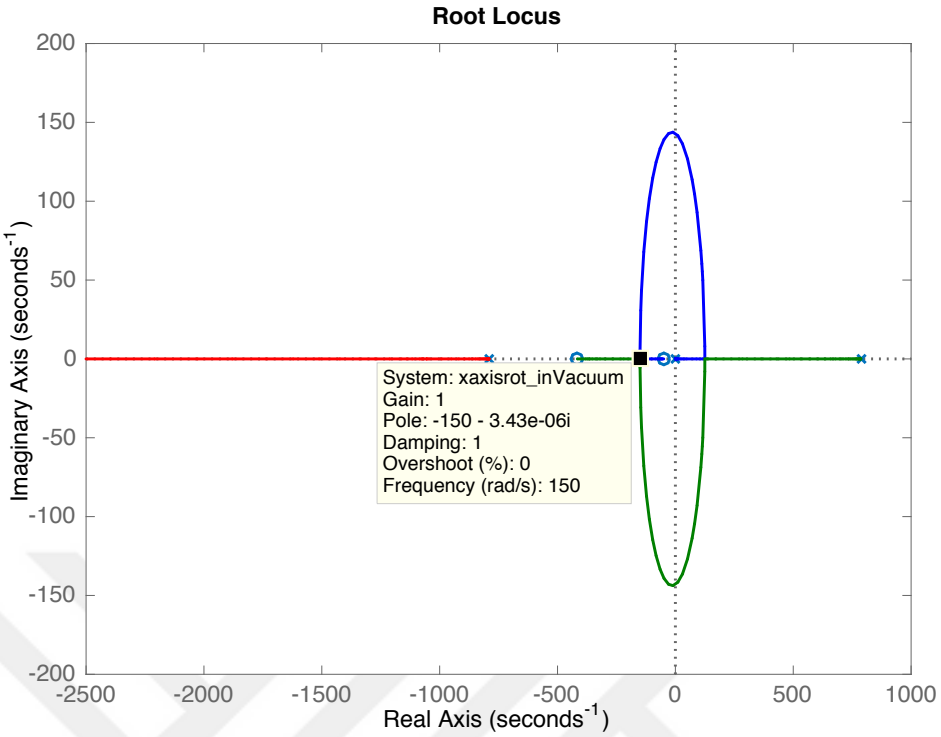

Figure 31 Root locus of PID controlled x axis rotational motion system, operated in vacuum.

3.3 Simulations

In the previous section, all the controllers are designed using the linearized system of equations. Moreover, in order to design a controller for a specific axis, it is assumed that all the motions along other axes are restricted. However, as represented in Section 2.2, all of the system equations are coupled and highly nonlinear. Therefore, designed controllers need to be tested using the nonlinear and coupled equations of motions. In that section, nonlinear simulation of the device is performed using Matlab Simulink.

Simulink block diagrams to implement the simulation are represented starting from Figure 32 to Figure 37. In the block shown in Figure 32, using the positions of rotor along 5 axes, capacitances between top stator out of plane motion electrodes and rotor are calculated. Moreover, actuation voltages represented in Figure 10, in

Section 2.2.1.1 are fed to same block to calculate generated forces by top stator out of plane motion electrodes. Notice that, input voltages fed to that block are saturated considering the maximum voltage that can be supplied by an OPAMP. Note that there is a similar block for bottom stator electrode in the simulation. Capacitances formed between top stator lateral motion electrodes and rotor, along with forces generated by top stator lateral motion electrodes are calculated in a similar manner, using the Simulink block shown in Figure 33. Carrier electrode capacitances, on the other hand, are calculated in a separate block as represented in Figure 35. Secondly, calculated forces in the blocks given in Figure 32 and in Figure 33 are used to calculate rotor positions, as represented in Figure 34. After that rotor position in each axis are converted to voltages using the readout circuitry as explained in Section 2.3.4. Related block diagram to achieve that transformation for a single axis (x-axis) is represented in Figure 36. Following that resulting voltage outputs are fed into related controllers and feedback control voltages are calculated, as represented in Figure 37. Note that, there are 4 similar blocks for the motion of the rotor along four remaining axes. Those blocks are not represented here. Finally, feedback voltages are supplied back to top/bottom stator out of plane motion electrodes block and top/bottom stator lateral motion electrodes block to calculate generated forces.

Simulation is performed both in air and in vacuum conditions. A 100 kHz Sine with peak-to-peak amplitude of 15 V is used as a carrier signal. Capacitance and resistor used in trans-impedance amplifier are 100 pF and 10 MOhms respectively. For the simulations initial deviations from the nominal positions are defined and responses of air and vacuum operated system are compared. Simulation results are represented between Figure 38 and Figure 47.

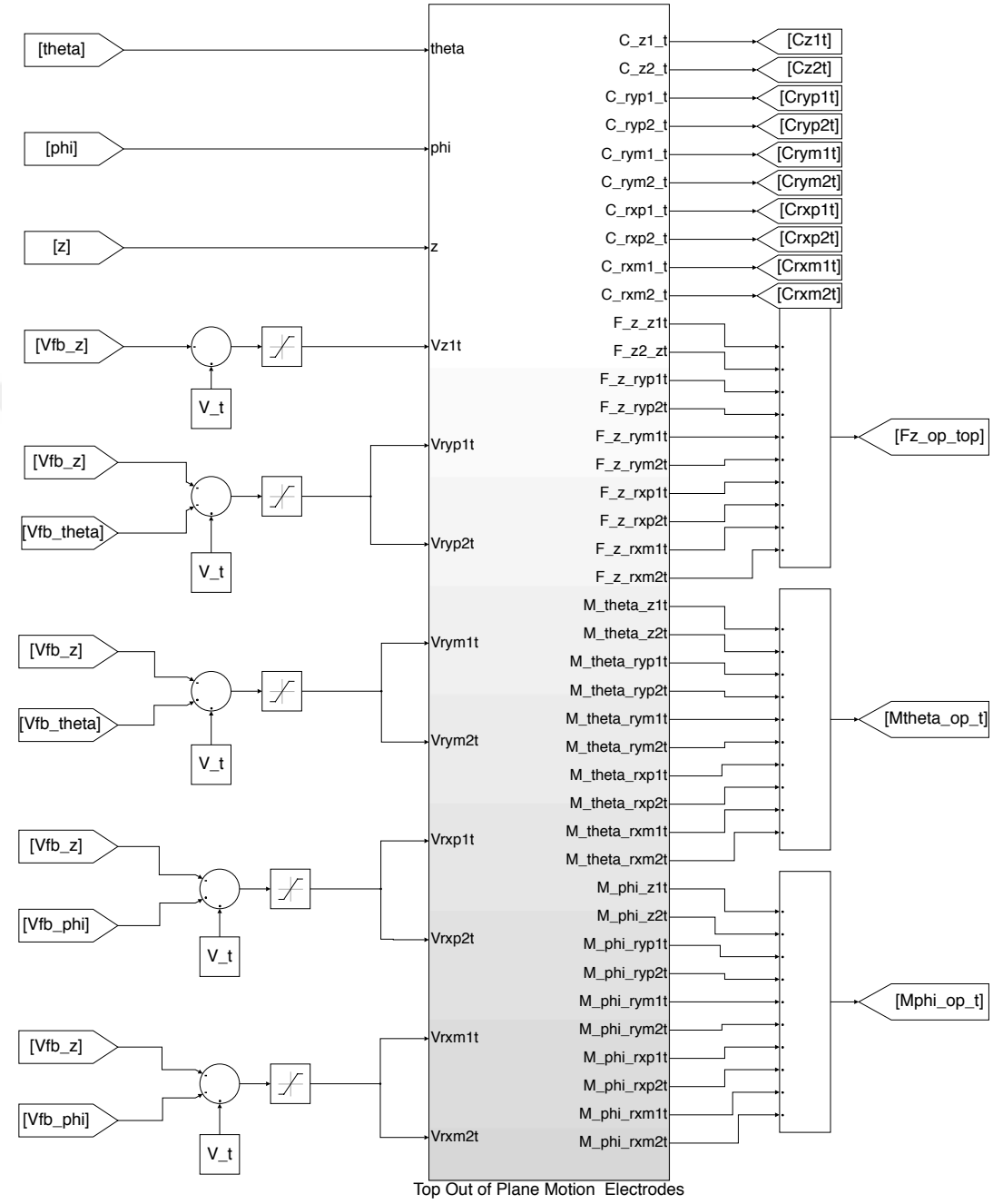

Figure 32 Simulink block diagram of top stator, out of plane motion electrodes

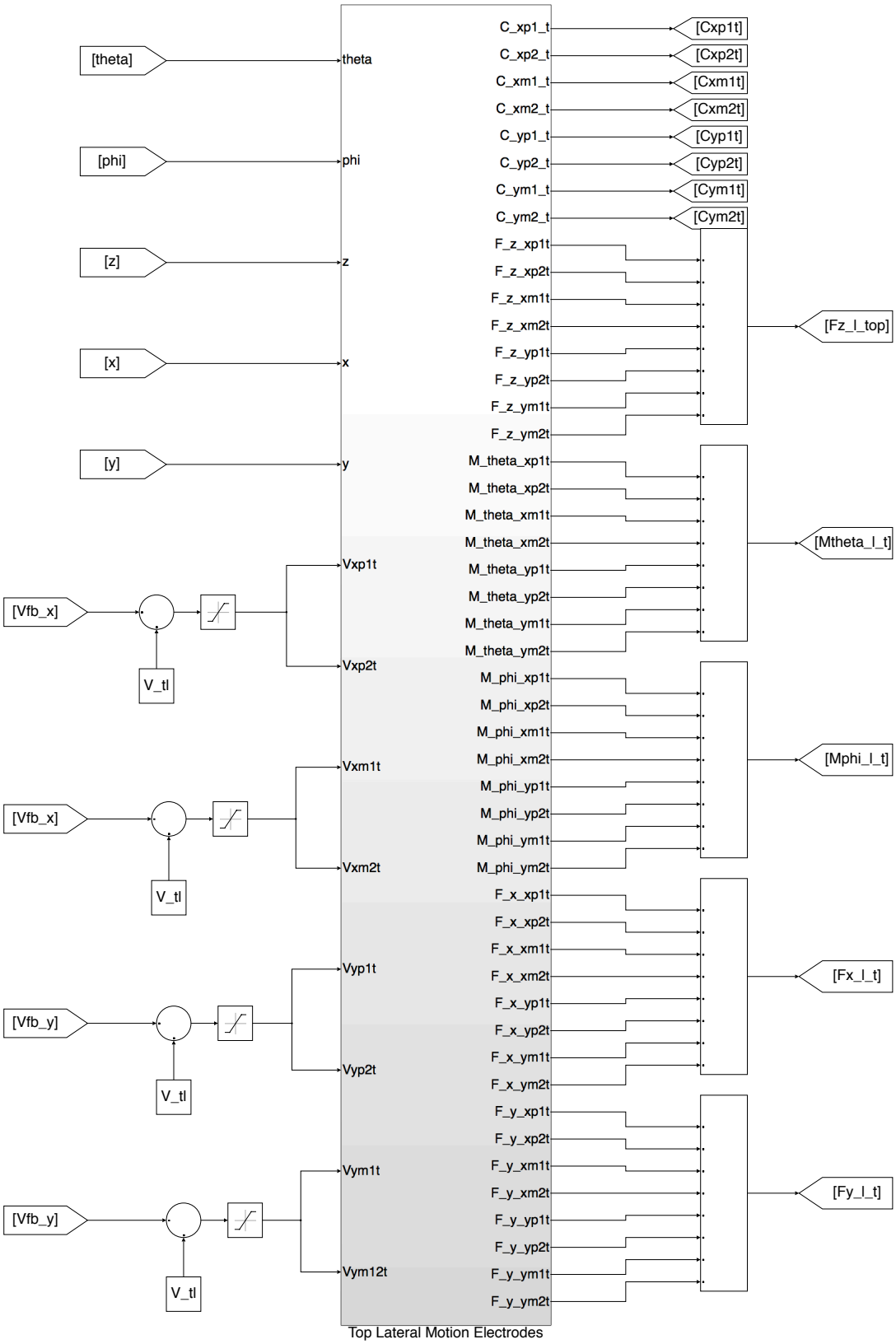

Figure 33 Simulink block diagram of top stator, lateral motion electrodes

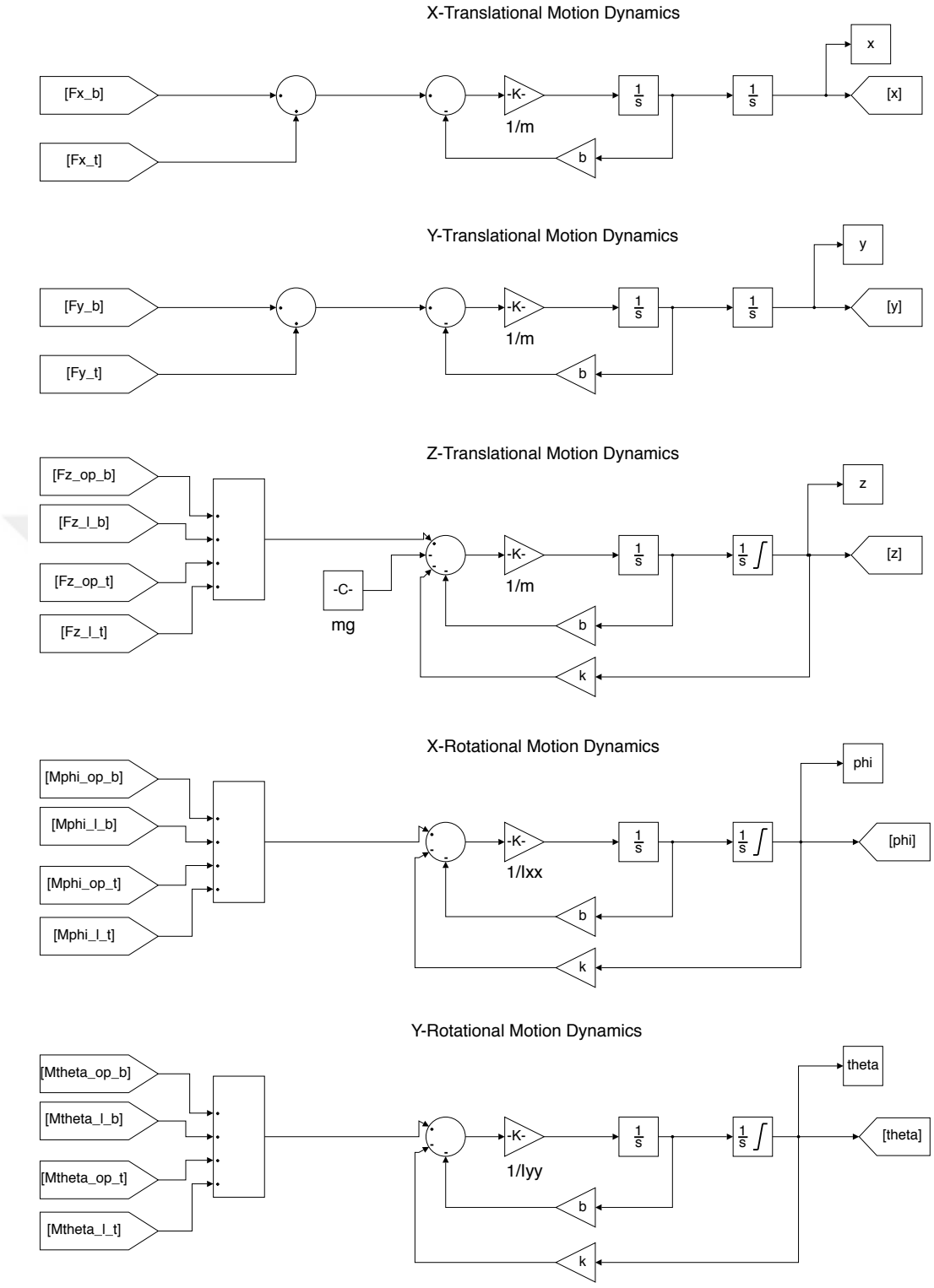

Figure 34 Simulink diagram of rotor dynamics along 5 axes

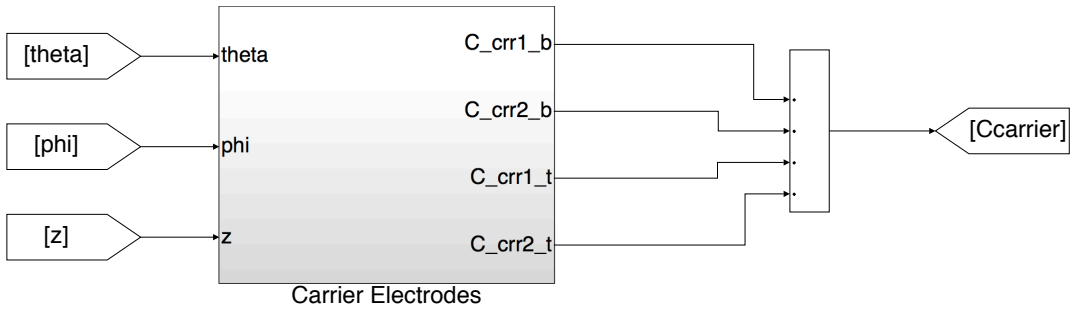

Figure 35 Simulink diagram of carrier electrodes

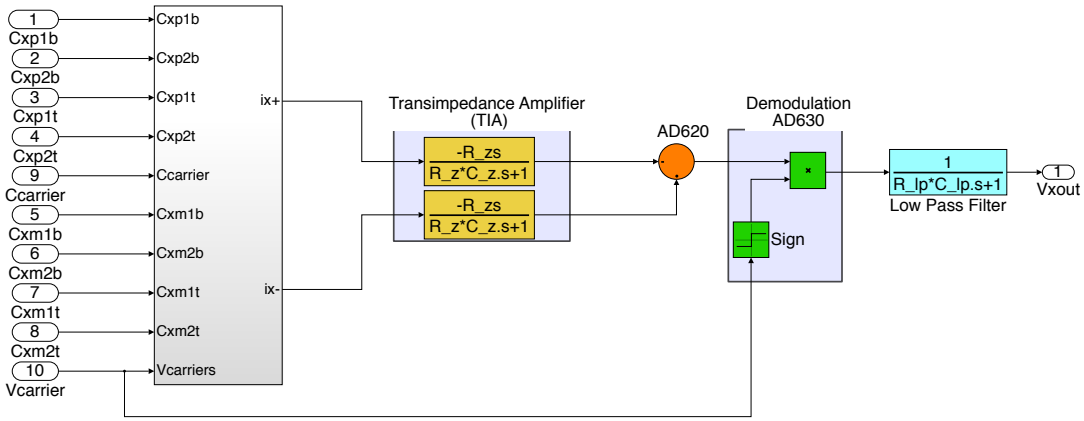

Figure 36 Simulink diagram of reading circuit of a single axis

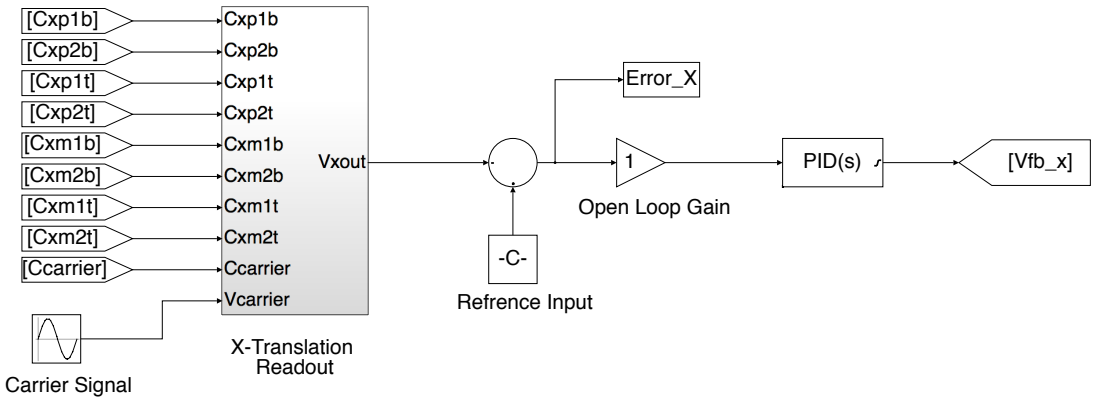

Figure 37 Simulink diagram of x-axis lateral motion control loop

As it can be seen from the results below, motions of rotor along x and y axes have similar response. It is assumed that damping mechanism acting on the system is slide film damping for those axes. This mechanism introduces relatively small damping and no stiffness. Therefore, behaviors of the system along those axes are similar for air and vacuum conditions. However, for out of plane motions squeeze film damping introduces relatively high damping and stiffness on the system, which results smaller response for air operated system. Existence of damping and stiffness eliminates oscillations in the motion of the rotor for those axes.

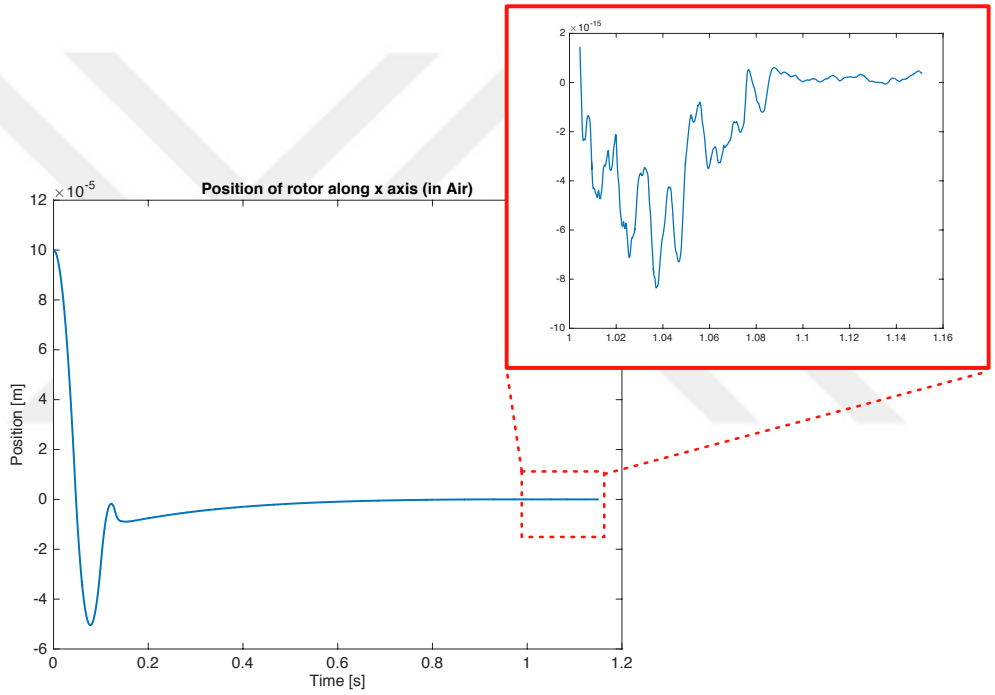

Figure 38 Response of rotor along x-axis, in air

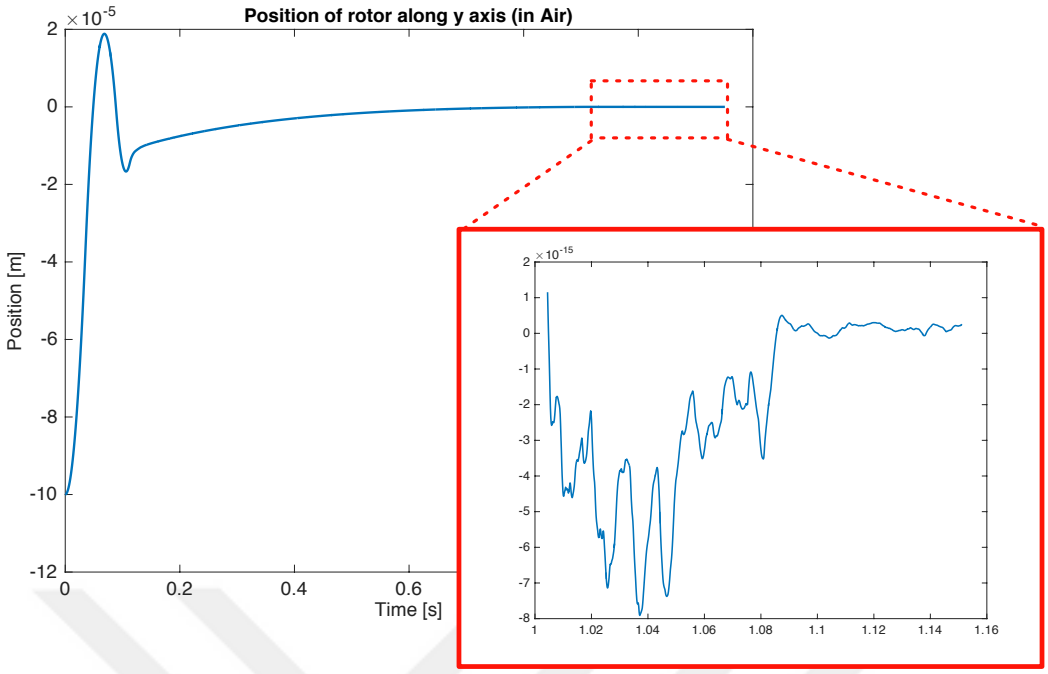

Figure 39 Response of rotor along y-axis, in air

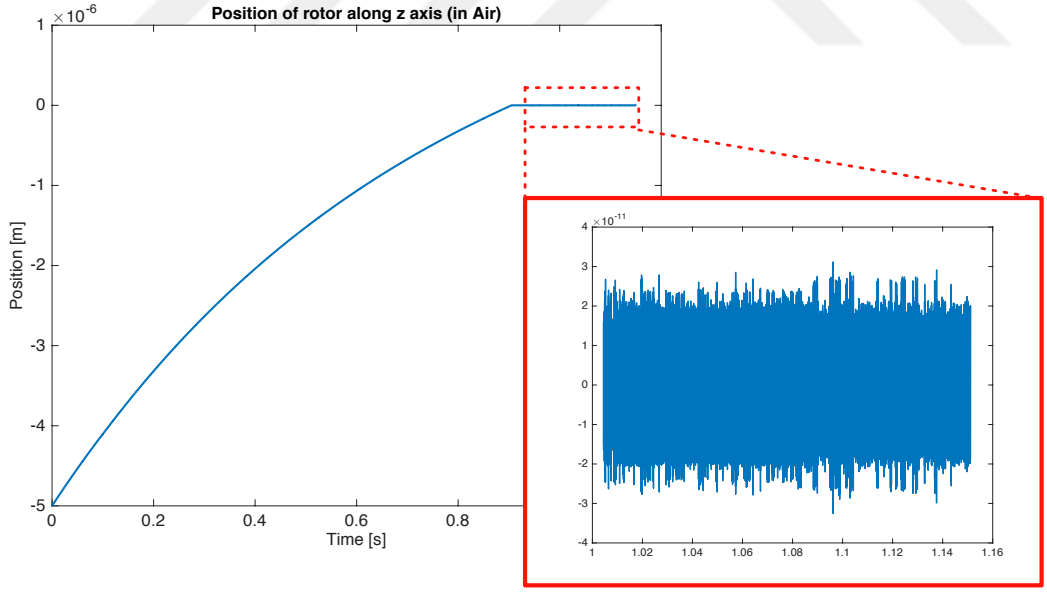

Figure 40 Response of rotor along z-axis, in air

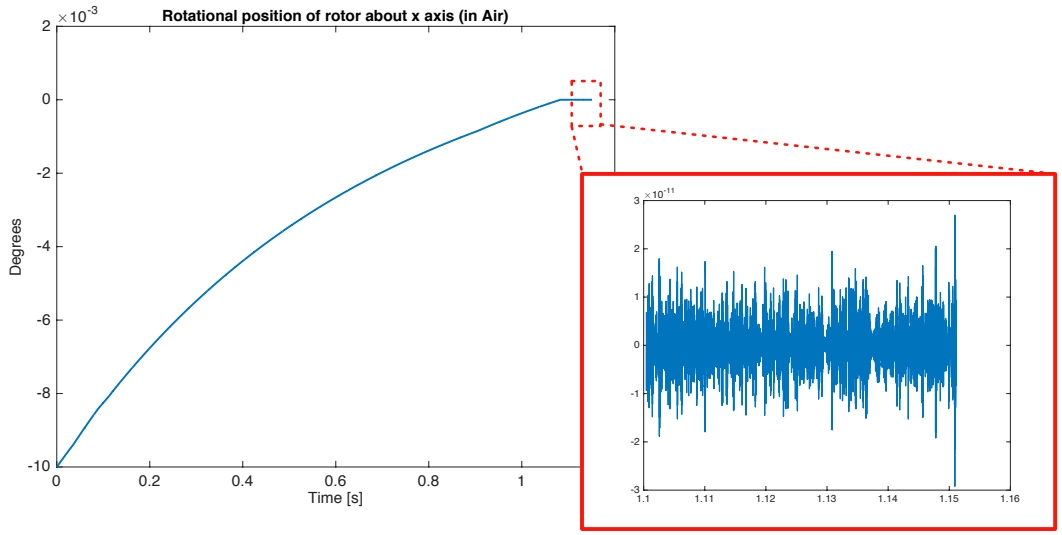

Figure 41 Response of rotor about x-axis, in air

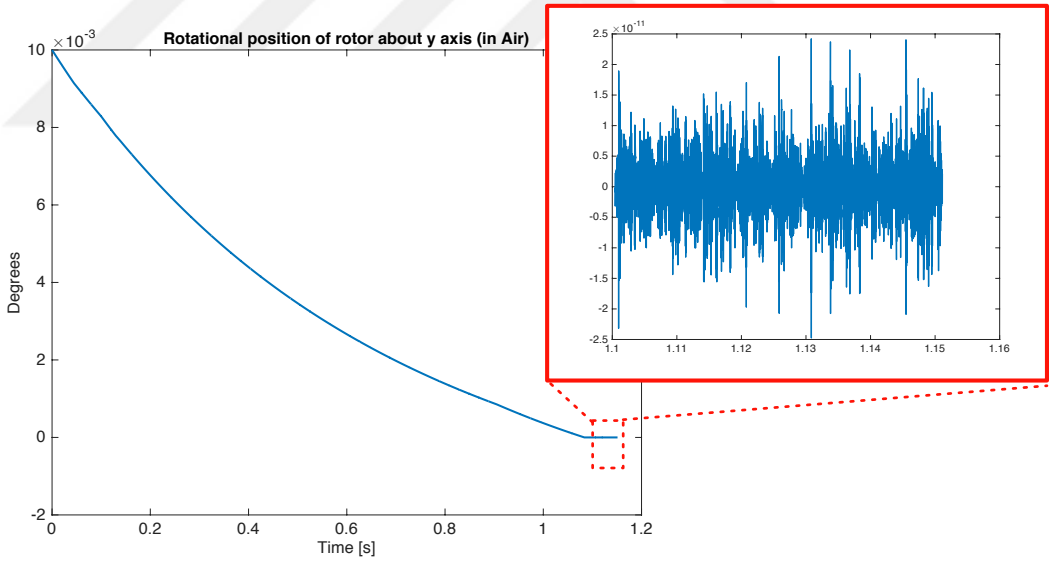

Figure 42 Response of rotor about y-axis, in air

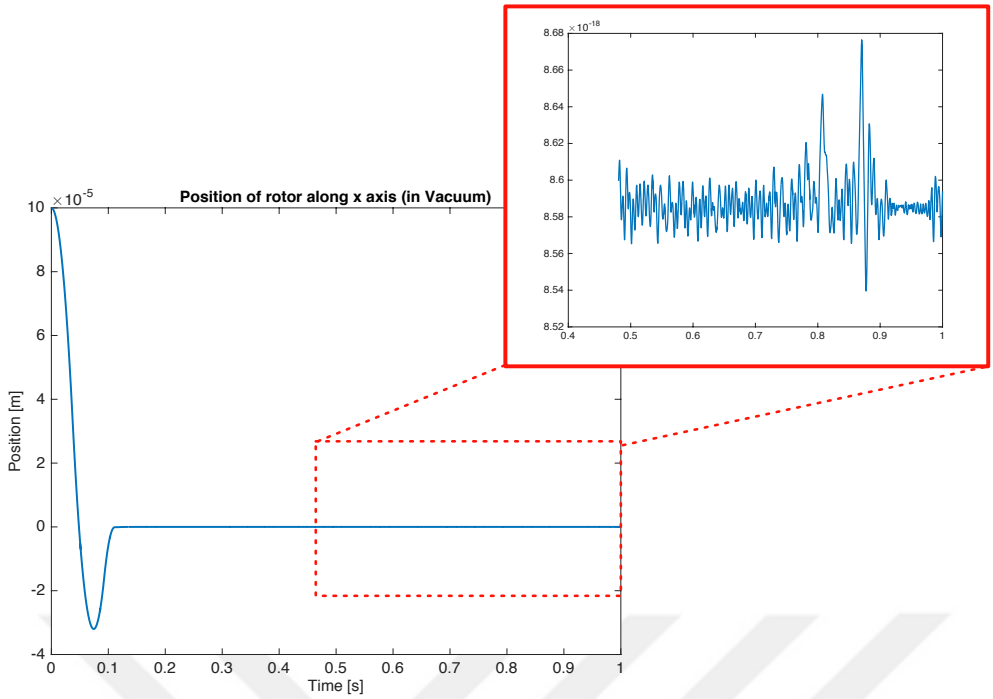

Figure 43 Response of rotor along x-axis, in vacuum

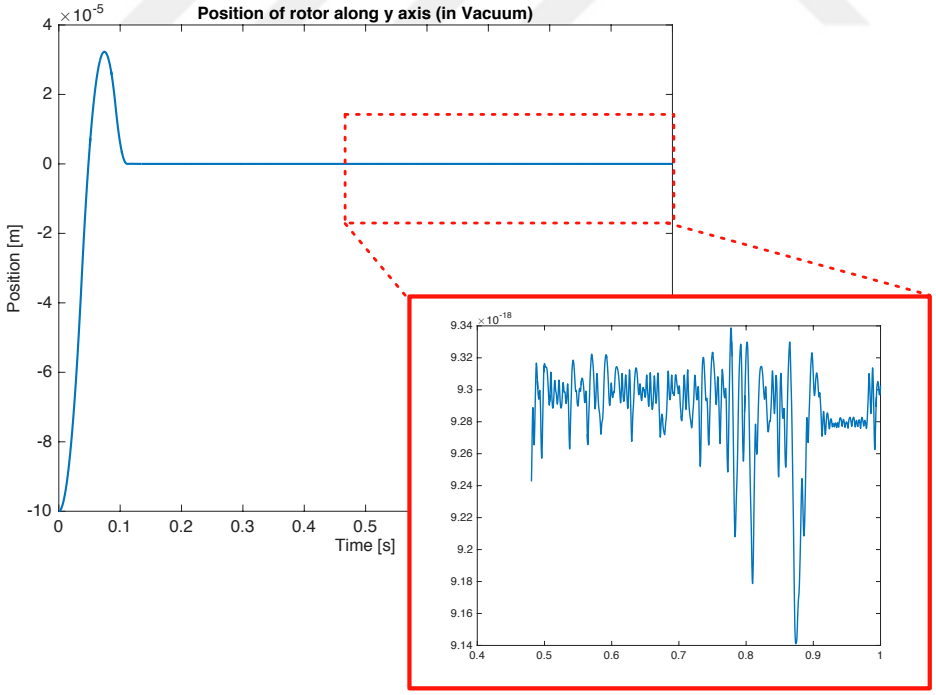

Figure 44 Response of rotor along y axis, in vacuum

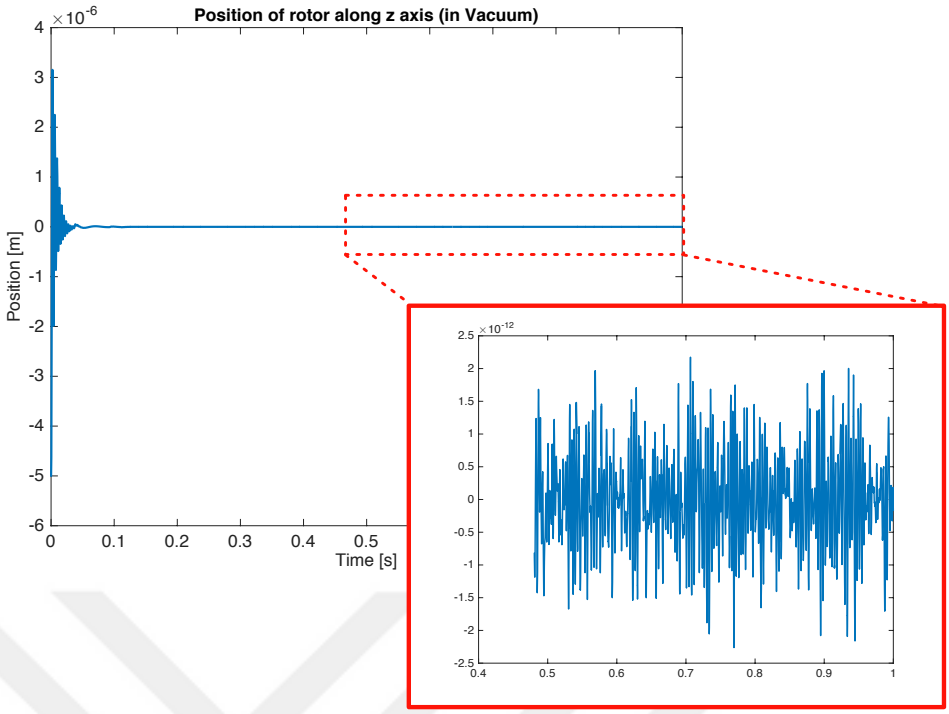

Figure 45 Response of rotor along z-axis, in vacuum

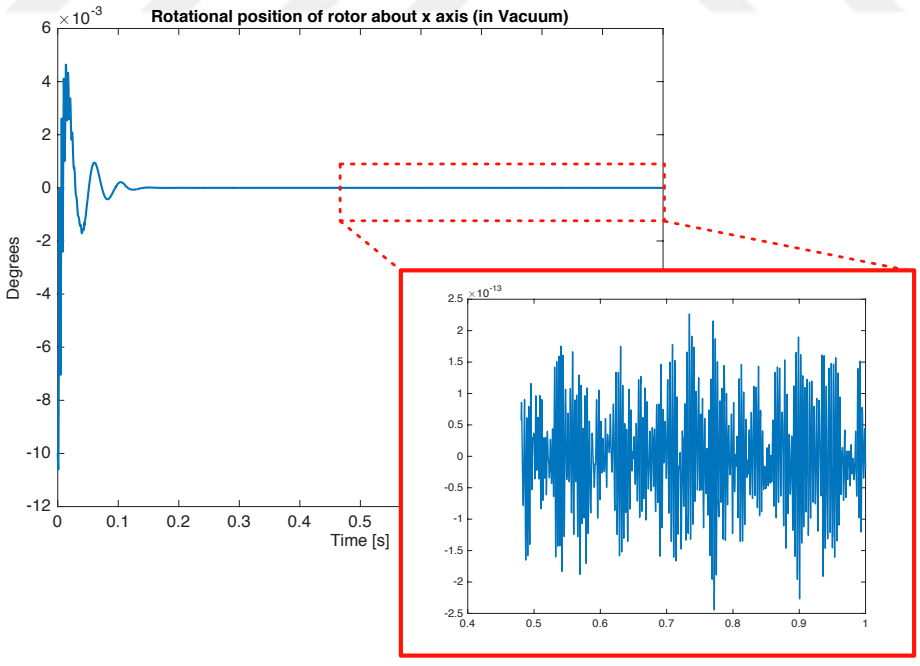

Figure 46 Response of rotor about x-axis, in vacuum

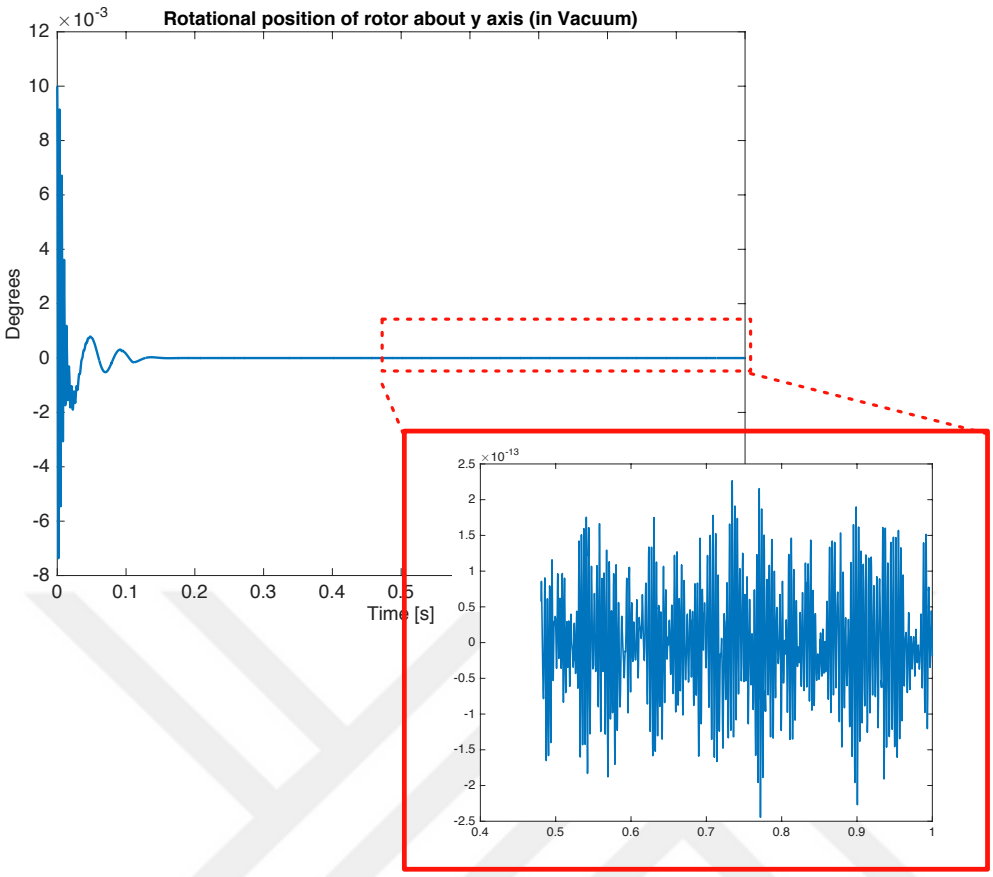

Figure 47 Response of rotor about y-axis, in vacuum

3.4 Noise on the System

Due to electronics components used for readout and controller circuits noise is generated on the proposed device. For the noise analysis, procedure outlined in [42] is used.

3.4.1.1 Noise due to Sense Electronics

As defined in section 2.3.4, readout circuit for capacitive detection consists of a TIA, an instrumentation amplifier, a demodulator and a passive RC low pass filter. Components used to implement that circuit are tabulated in Table 2 below.

Table 2 Components used in readout circuit

Circuit Element	Component
TIA	LF353
Instrumentation Amplifier	AD620
Demodulator	AD630
C_{TIA}	100 pF
R_{TIA}	10 MΩ
ω_c	100 kHz

As explained in [42], there are three mechanism which generated noise at TIA.

Firstly, OPAMP (LF353) produces a current noise and it is converted into voltage by the impedance of the TIA. In [43], equivalent input noise current is given as 0.01 $pA/Hz^{0.5}$, then resulting voltage noise is calculated as

$$V_{n1,LF353} = \frac{0.01 \cdot 10^{-9}\,\mathrm{A}/\sqrt{\mathrm{Hz}}}{\omega_c C_{TIA}} \tag{3.69}$$

Substituting numerical values of ω_c and C_{TIA};

$$V_{n1,LF353} = 1.592 \cdot 10^{-10}\,\mathrm{V}/\sqrt{\mathrm{Hz}} \tag{3.70}$$

Secondly, TIA produces noise due to voltage noise of the OPAMP Equivalent voltage noise of LF353 in [43] is given as 18 $nV/\ Hz^{0.5}$. This noise is amplified by the noise gain of the TIA. Noise gain of the TIA can be found by using Figure 48. [44]

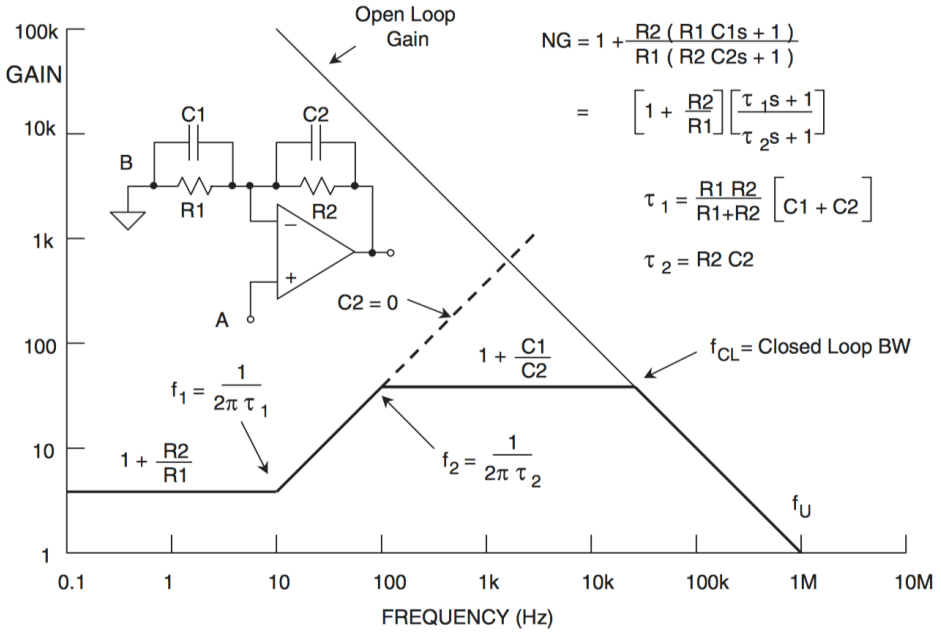

Figure 48 Generalized noise gain Bode plot of a TIA

In the above figure, transfer function for noise gain is given as

$$NG = 1 + \frac{R_2\left(R_1C_1s+1\right)}{R_1\left(R_2C_2s+1\right)} \tag{3.71}$$

R_1 term in above expression corresponds to resistance between rotor and bottom/top stator, for our device. Since there is no mechanical contact it can be taken as infinity. Therefore, noise gain can be approximated as 2. So equivalent voltage noise of TIA is;

$$V_{n2,LF353} = 2\left(18\,\text{nV}/\sqrt{\text{Hz}}\right) = 36\,\text{nV}/\sqrt{\text{Hz}} \tag{3.72}$$

Thirdly, shunt resistor used TIA generates a current noise and its converted into voltage thorough the gain of TIA.

$$V_{n3.LF353} = \sqrt{\frac{4k_BT}{R_{TIA}}}\frac{1}{\omega_c C_{TIA}} \tag{3.73}$$

where, k_B is Boltzman constant and T is the temperature. Recall that R_{TIA} is 10 MΩ, ω_c is 100 kHz and C_{TIA} is 100 pF. Substituting those values into equation (3.73)

$$V_{n3.LF353} = 1.28 \cdot 10^{-9}\ \mathrm{V}/\sqrt{\mathrm{Hz}} \tag{3.74}$$

Finally, total noise generated by TIA is

$$V_{n,LF353} = \sqrt{{V_{n1,LF353}}^2 + {V_{n2,LF353}}^2 + {V_{n3,LF353}}^2} = 25.03 \cdot 10^{-9}\ \mathrm{V}/\sqrt{\mathrm{Hz}} \tag{3.75}$$

After TIA stages, resulting signals are fed into an instrumentation amplifier (AD620). In [45], input voltage noise (RTI) is modeled as

$$V_{n,AD620} = \sqrt{{e_{ni}}^2 + \left(\frac{e_{no}}{G}\right)^2} \tag{3.76}$$

where, e_{ni}= 9 nV/Hz$^{0.5}$, e_{no}=72 nV/Hz$^{0.5}$ and G is gain. Then total noise at the output of instrumentation amplifier is given in (3.77) below.

$$V_{n,AD620out} = G\sqrt{2\left({V_{n,AD620}}^2 + {V_{n,LF353}}^2\right)} \tag{3.77}$$

Gain of instrumentation amplifier is 1. Substituting numerical values into equations (3.76) and (3.77), noise at the output of instrumentation amplifier is;

$$V_{n,AD620out} = 108.6 \cdot 10^{-9}\ \mathrm{V}/\sqrt{\mathrm{Hz}} \tag{3.78}$$

As explained in [42], when AD630 is used as a balanced demodulator, it can recover signal from 100 dB noise. Therefore, it is assumed that noise contribution of demodulator is assumed to be zero.

Finally, in [46] noise contribution of RC low pass filter is given as

$$V_{n,LP} = \sqrt{\frac{k_B T}{C_{LP}}} = 53.79 \cdot 10^{-9}\ \mathrm{V}/\sqrt{\mathrm{Hz}} \tag{3.79}$$

As a result total noise produced by reading circuit is

$$V_{n,sense} = \sqrt{V_{n,AD620out}{}^2 + V_{n,LP}{}^2} = 548.7 \cdot 10^{-9}\ \mathrm{V}/\sqrt{\mathrm{Hz}} \tag{3.80}$$

This equivalent voltage noise is converted to position equivalent noise by dividing its value with the scale factor of readout circuitry of each axis. Scale factors for each axis are calculated using equations (3.30), (3.51) and (3.67). Resulting scale factors and equivalent position noises are tabulated in Table 3 below.

Table 3 Noise on rotor due to sense electronics

Axis	Scale Factor	Equivalent Noise on Position
x, y	$610.22\,\mathrm{V/m}$	$177.9 \cdot 10^{-12}\ \mathrm{m}/\sqrt{\mathrm{Hz}}$
z	$1.90 \cdot 10^{4}\ \mathrm{V/m}$	$5.717 \cdot 10^{-12}\ \mathrm{m}/\sqrt{\mathrm{Hz}}$
ϕ, θ	$98.82\,\mathrm{V/m}$	$1.099 \cdot 10^{-9}\ \mathrm{rad}/\sqrt{\mathrm{Hz}}$

3.4.1.2 Noise due to Controller Electronics

All of the control electronics is implemented using OPAMPs, LF353. Since controllers and comparators operate at DC, main source of noise is flicker noise. In [43], 1/f noise corner frequency is given as 50 Hz and equivalent voltage noise floor is given as 25 nV/Hz$^{0.5}$, then total noise contribution of an OPAMP used as a P/I/D controller or a comparator is found as

$$V_{n,LF353c} = \sqrt{\left(25\frac{nV}{\sqrt{Hz}}\right)^2 + \left(25\frac{nV}{\sqrt{Hz}}\right)^2 \cdot 50\,Hz\,\frac{1}{f}} \tag{3.81}$$

where, f=1 Hz.

$$V_{n,cont} = V_{n,LF353n} + k \cdot V_{n,LF353n} \tag{3.82}$$

where, k is number of controllers used, i.e. k=1 if P-controller is used, k=3 if PID controller is used. In order to calculate maximum amount of the noise induced to the system lets take k=3, then

$$V_{n,cont} = 4 \cdot V_{n,LF353c} = 3.57 \cdot 10^{-7}\ \mathrm{V}/\sqrt{\mathrm{Hz}} \tag{3.83}$$

Around the nominal position, scale factor between voltage and force are found using equations (3.20), (3.42) and (3.58). Following that, those scale factors are multiplied with equivalent voltage noise found in (3.83) and equivalent noise on generated forces on rotor are found for each axis. Finally, dividing equivalent force noises by mass/inertia of the rotor gives equivalent noises on acceleration of the rotor for each axis. Results are tabulated in Table 4 below.

By integrating noise on acceleration two times it is converted to position noise. During that conversion noise is degraded by a factor of $1/\omega^2$. Therefore, noises generated on rotor positions by controller electronics are neglected.

Table 4 Noise on rotor due controller electronics

Axis	Scale Factor	Equivalent Noise on Force / Moment	Equivalent Noise on Acceleration
x,y	$4.086 \cdot 10^{-7}$ N/V	$1.459 \cdot 10^{-13}\ \mathrm{N}/\sqrt{\mathrm{Hz}}$	$2.462 \cdot 10^{-9}\ \mathrm{m/s^2}/\sqrt{\mathrm{Hz}}$
z	$7.708 \cdot 10^{-5}$ N/V	$2.752 \cdot 10^{-11}\ \mathrm{N}/\sqrt{\mathrm{Hz}}$	$4.643 \cdot 10^{-7}\ \mathrm{m/s^2}/\sqrt{\mathrm{Hz}}$
ϕ, θ	$1.261 \cdot 10^{-7}$ N/V	$4.502 \cdot 10^{-14}\ \mathrm{N}/\sqrt{\mathrm{Hz}}$	$2.473 \cdot 10^{-5}\ \mathrm{rad/s^2}/\sqrt{\mathrm{Hz}}$

3.5 Summary

In this chapter, system parameters used in controller design are calculated in Section 3.1. After that controllers for the lateral motion of rotor along x & y axes, for motion of rotor along z axis and for rotational motion of rotor about x & y axes are designed, in Section 3.2. Following that, robustness of designed controllers are represented on a Simulink model. Finally, noise generated due to sense and controller electronics are discussed.

CHAPTER 4

FABRICATION OF MEMS BASED LEVITATED PLATFORM

In this chapter, the fabrication of proposed device is represented. In the first section fabrication of stator is explained and layer configuration of the stator structure is discussed in detail. In the second section fabrication of rotor is given. Finally in the last section, this chapter is summarized.

4.1 Fabrication of Stator

Stator structures are manufactured from 6 layered printed circuit board (PCB). 3D view of the PCB and layer configuration is represented in Figure 49. On the first layer, all electrode structures and aligning ball positions are defined. Moreover, first layer is also used to interconnect the phase-1 and phase-2 rotational motion actuation electrodes to each other. In order to interconnect the phase-3 rotational motion electrodes sixth layer is used. Second and fourth layer is used as ground plane. All paths to carry the electrode signals (except carrier electrode), are drawn on third layer. Carrier electrode signal path is located n the fifth layer. Thanks to that layer configuration, it is desired to minimize the interactions of electrode signal with itself and environment. Manufactured stator structures are represented in Figure 50.

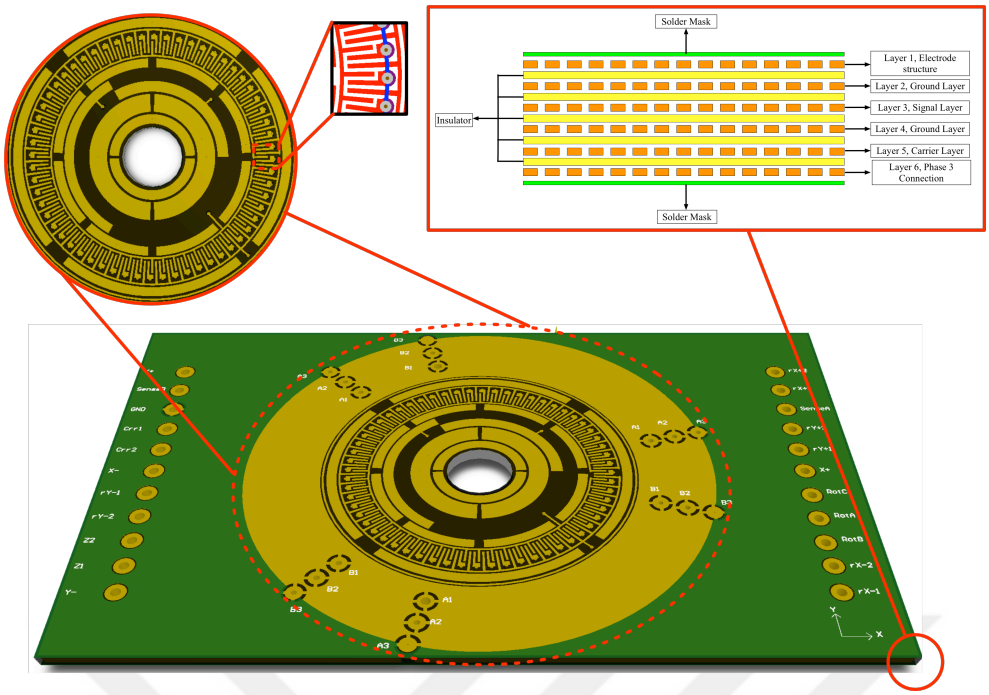

Figure 49 3D view of the stator PCB and layer configuration

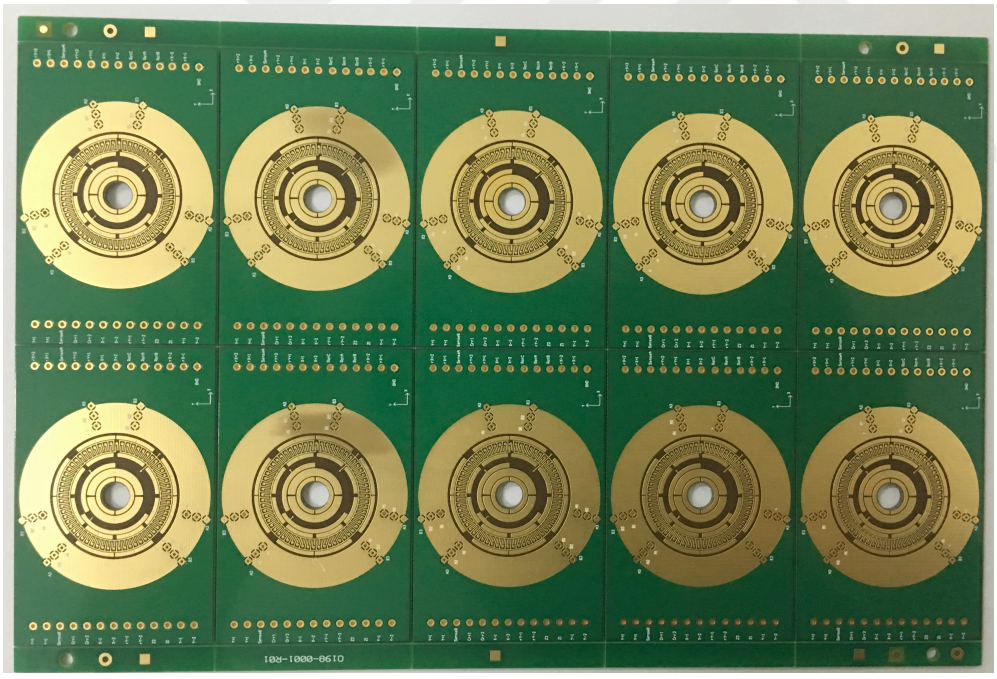

Figure 50 Manufactured stator structures

To align top and bottom stator structures to each other, bearing balls are used. Combination of ball diameter and aligning hole diameter determines the nominal gap between rotor and stators. Aligned top and bottom stators are represented in Figure 51 below.

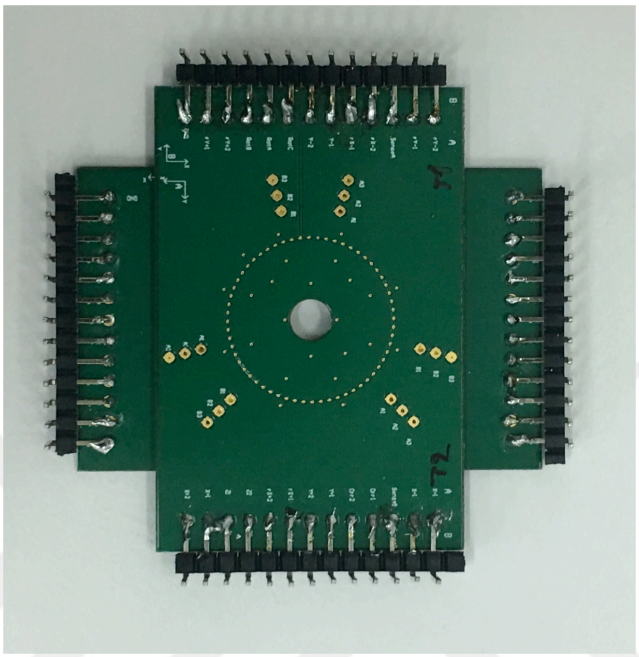

Figure 51 Aligned top and bottom stators

4.2 Fabrication of Rotor

Rotor is manufactured from micro machined silicon. To decrease the mass and inertia of the rotor, thickness of the rotor should be minimized. Therefore, for the manufacturing of the rotor structure, Silicon on Insulator (SOI) wafer is used. For the fabrication of rotor, oxide deposited on the handle layer of SOI wafer, firstly. Secondly, deposited oxide layer is patterned by Reactive Ion Etching (RIE). Following that, device layer of SOI wafer is patterned by Deep Reactive Ion Etching. Then buried oxide layer of SOI wafer is patterned by RIE. Finally, handle layer of SOI wafer is removed by DRIE and rotor structures are released. Fabrication scheme is represented in Figure 52 below. Manufactured rotor structures are given in Figure 53.

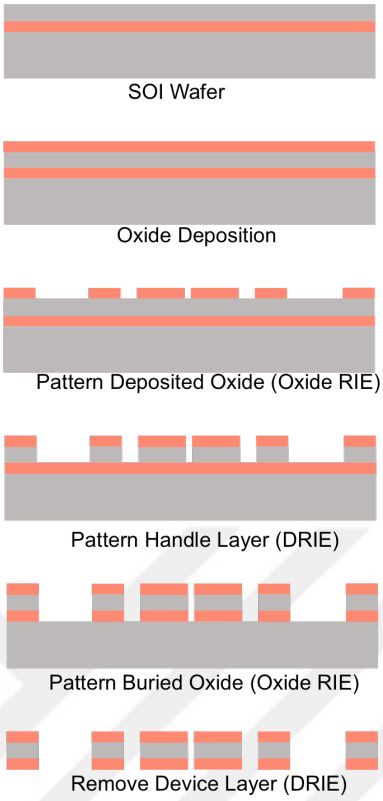

Figure 52 Fabrication of rotor

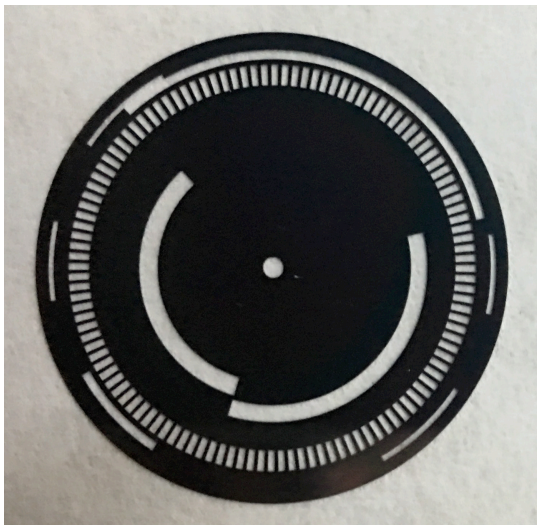

Figure 53 Manufactured rotor structure

4.3 Summary

In this chapter, the fabrication of proposed device is presented. Firstly, manufacturing of stator structure is discussed in detail. Moreover, alignment method of top and bottom stator is given. In the second section, fabrication steps of rotor are given and fabricated rotor structure is presented.

CHAPTER 5

CONCLUSION AND FUTURE WORK

This work presents a MEMS based levitated platform for laser scanner applications. Electrostatic detection and actuation are utilized for levitation of the platform. In the scope of that study, design, simulations and fabrication of the proposed device carried out and represented in the thesis. Results of this study and accomplishments are listed below:

- There are number of laser scanners presented in the literature for several applications. All of the scanners in the literature based on a mechanically suspended structures, which redirects a light source. Mechanical connection of those structures limits the maximum achievable scan range. This work represents a levitated platform for laser scanner applications. The main motivation behind the proposed structure is to achieve 360 degrees of scan range.

- Required electrode arrangement to generate vertical force is explained. Following that, utilization of this requirement in the design is represented along with the working principle of proposed device.

- Mathematical models for actuation and detection mechanisms for levitation are derived. For that purpose, firstly, capacitances generated between levitated platform (rotor) and stators are defined. Then mathematical expression, which gives values of those capacitances as a function of position of rotor along 5 axes are derived. After that those expressions are used to

determine generated force by each electrode located on stator. Finally, equations of motion of the rotor along 5 axes are represented, using force models. In order to find damping and stiffness acting on the rotor, squeeze and slide film damping models are utilized. After modeling motion of the rotor, capacitive detection models for each axis are discussed, with their read-out circuitry.

- In order to ensure stable levitation of the rotor, position of rotor along 5 axes need to be controlled. Therefore, closed loop controllers for each 5 axis are designed. For controller design, system parameters (mass, inertia, damping) are calculated. Following that, root locus design techniques are utilized for controller design. For root locus design procedure linear time invariant system equations are required. However, modeled equations are coupled and highly non-linear. Those equations are decoupled, assuming motion of the rotor is restricted all the remaining axes, other than axis of interest. Following that, decoupled expressions are linearized about the nominal position of rotor using the linear terms of its Taylor series expression.

- Damping and stiffness acting on the system, highly depends on ambient pressure. Therefore, behavior of the device both in air and in vacuum is analyzed. Controllers are designed for both operating conditions. After that preliminary of designed controllers and robustness of system is simulated using Matlab Simulink. In the simulations, some deviations are defined about rotor's nominal position as initial conditions. Air operated system subject to those initial conditions is stabilized in about 1.1 seconds, while vacuum operated system is stabilized in about 0.15 seconds.

- Electronics used for sensing and controller circuit induce noise on the system. Equivalent voltage noise is calculated and its effect on position of rotor along 5 axes are represented.

- Fabrication of the device is performed. Stator structures are manufactured from a 6 layer PCB. Rotor, on the other hand, is fabricated using a SOI wafer.

Rotor has a radius of 11300 μm and a thickness of 80 μm. Two stators are aligned with respect to each other by using bearing-balls with a diameter of 1 mm.

Apart from those achievements, in order to improve the performance of the device further, following points should be considered as future works.

- In the scope of that thesis, stability of proposed structure along 5 axes is examined by simulations. In further studies, performed simulations can be verified by experiments.

- Due to easiness of manufacturing, advantages of having a multilayered and structure and low cost of manufacturing Printed Circuit Board (PCB) is used as a stator structure. However, due to limitations on minimum feature size of PCB manufacturing, dimensions of stator structure so rotor cannot be decreased after a point. Having a larger sized rotor increases utilized power for levitation. Therefore, performance of proposed structure can be increased if stator structure is fabricated using MEMS fabrication techniques.

- Approximated squeezed film damping model can be improved by performing following studies;

    - Squeezed damping model utilized to model damping requires the oscillations of rotor about its nominal position as explained in Section 2.3.3.2 and it is assumed to be a certain value. This assumption can be improved/verified by analyzing the power spectral densities of time record rotor positions both in simulations and experiments so that approximated damping and stiffness values can be improved.

    - In the simulations equivalent damping and stiffness values are calculated for out of plane rotational motions. Damping and stiffness values for those axes can be improved by finite element models.

- Finally, in the damping models holes & slots on the rotor are ignored. Finite element simulations can be performed, which takes all the slots & holes into account to have better damping model can be performed.

- Implemented controllers along 5 axes can be optimized to have better transient response characteristics.

- In that research stability of rotor along 5 axes is studied with Simulink simulations. In the further studies, motion of the rotor on the remaining axis (rotation of the rotor about its normal) can be investigated by simulations and experiments.

- In the noise analysis it is observed that passive low pass filter is the main source of noise. In order to decrease the noise of electronics higher order low pass filters can be used instead of passive low pass filters.

REFERENCES

[1] R. R. Schaller, "Moore's law: past, present and future," *IEEE Spectrum,* vol. 34, no. 6, pp. 52-59, 1997.

[2] K. E. Petersen, "Silicon as a mechanical material," *Proceedings of the IEEE,* vol. 70, no. 5, pp. 420-457, 1982.

[3] C. Liu, *Foundation of MEMS*. England: Pearson, 2010.

[4] J. K. Fremerey and K. Boden, "Active permanent magnet suspensions for scientific instruments," *Journal of Physics E: Scientific Instruments,* vol. 11, no. 2, p. 106, 1978.

[5] L. Hu, H. Wang, W. Xie, and B. Wei, "Electrostatic levitation under the single-axis feedback control condition," *Science China Physics, Mechanics and Astronomy,* vol. 53, no. 8, pp. 1438-1444, 2010/08/01 2010.

[6] E. Bachalet, "Levitating Transmitting Apparatus," 1912.

[7] G. He, K. Chen, S. Tan, and W. Wang, "Electrical levitation for micromotors, microgyroscopes and microaccelerometers," *Sensors and Actuators A: Physical,* vol. 54, no. 1–3, pp. 741-745, 6// 1996.

[8] K. Michael, M. F. Mateen, and G. R. E. Alan, "Modelling and design of an electrostatically levitated disc for inertial sensing applications," *Journal of Micromechanics and Microengineering,* vol. 11, no. 4, p. 423, 2001.

[9] R. Houlihan and M. Kraft, "Modelling of an accelerometer based on a levitated proof mass," *Journal of Micromechanics and Microengineering,* vol. 12, no. 4, p. 495, 2002.

[10] R. Toda, N. Takeda, T. Murakoshi, S. Nakamura, and M. Esashi, "Electrostatically levitated spherical 3-axis accelerometer," in *Micro Electro Mechanical Systems, 2002. The Fifteenth IEEE International Conference on*, 2002, pp. 710-713.

[11] M. Takao, E. Yasuo, F. Keisuke, N. Sigeru, and E. Masayoshi, "Electrostatically Levitated Ring-Shaped Rotational-Gyro/Accelerometer," *Japanese Journal of Applied Physics,* vol. 42, no. 4S, p. 2468, 2003.

[12] T. Terasawa, T. Watanabe, and T. Murakoshi, "Electrostatically levitated ring-shaped rotational-gyro/accelerometer using all-digital OFDM detection with TAD," in *Sensors, 2012 IEEE*, 2012, pp. 1-4.

[13] C. B. Williams, C. Shearwood, P. H. Mellor, A. D. Mattingley, M. R. J. Gibbs, and R. B. Yates, "Initial fabrication of a micro-induction gyroscope," *Microelectronic Engineering,* vol. 30, no. 1–4, pp. 531-534, 1// 1996.

[14] C. B. Williams, C. Shearwood, P. H. Mellor, and R. B. Yates, "Modelling and testing of a frictionless levitated micromotor," *Sensors and Actuators A: Physical,* vol. 61, no. 1–3, pp. 469-473, 6// 1997.

[15] C. Shearwood, K. Y. Ho, C. B. Williams, and H. Gong, "Development of a levitated micromotor for application as a gyroscope," *Sensors and Actuators A: Physical,* vol. 83, no. 1–3, pp. 85-92, 5/22/ 2000.

[16] X. S. Wu, W. Y. Chen, X. L. Zhao, and W. P. Zhang, "Micromotor with electromagnetically levitated rotor using separated coils," *Electronics Letters,* vol. 40, no. 16, pp. 996-997, 2004.

[17] W. Xiaosheng, C. Wenyuan, Z. Xiaolin, and Z. Weiping, "Development of a micromachined rotating gyroscope with electromagnetically levitated rotor," *Journal of Micromechanics and Microengineering,* vol. 16, no. 10, p. 1993, 2006.

[18] K. Liu *et al.*, "An innovative micro-diamagnetic levitation system with coils applied in micro-gyroscope," *Microsystem Technologies,* vol. 16, no. 3, p. 431, 2009/11/12 2009.

[19] K. V. Poletkin, A. I. Chernomorsky, and C. Shearwood, "Proposal for Micromachined Accelerometer, Based on a Contactless Suspension With Zero Spring Constant," *IEEE Sensors Journal,* vol. 12, no. 7, pp. 2407-2413, 2012.

[20] K. Poletkin, Z. Lu, U. Wallrabe, and V. Badilita, "Hybrid electromagnetic and electrostatic micromachined suspension with adjustable dynamics," *Journal of Physics: Conference Series,* vol. 660, no. 1, p. 012005, 2015.

[21] W. Shao Ju, J. Jong Up, T. Higuchi, and J. Ju, "Electrostatic force analysis of electrostatic levitation system," in *SICE '95. Proceedings of the 34th SICE Annual Conference. International Session Papers*, 1995, pp. 1347-1352.

[22] W. Zhang, G. Meng, and H. Li, "Electrostatic micromotor and its reliability," *Microelectronics Reliability,* vol. 45, no. 7–8, pp. 1230-1242, 7// 2005.

[23] W. J. Bencze, M. E. Eglington, R. W. Brumley, and S. Buchman, "Precision electrostatic suspension system for the Gravity Probe B relativity mission's science gyroscopes," *Advances in Space Research,* vol. 39, no. 2, pp. 224-229, 2007/01/01/ 2007.

[24] J. Bernstein *et al.*, "Two axis-of-rotation mirror array using electromagnetic MEMS," in *The Sixteenth Annual International Conference on Micro Electro Mechanical Systems, 2003. MEMS-03 Kyoto. IEEE*, 2003, pp. 275-278.

[25] H. Miyajima *et al.*, "A MEMS electromagnetic optical scanner for a commercial confocal laser scanning microscope," *Journal of Microelectromechanical Systems,* vol. 12, no. 3, pp. 243-251, 2003.

[26] A. D. Yalcinkaya, H. Urey, D. Brown, T. Montague, and R. Sprague, "Two-axis electromagnetic microscanner for high resolution displays," *Journal of Microelectromechanical Systems,* vol. 15, no. 4, pp. 786-794, 2006.

[27] X. Mu *et al.*, "An electrostatic in-plane rotational MEMS micro-scanner," in *2012 International Conference on Optical MEMS and Nanophotonics*, 2012, pp. 240-241.

[28] M. Mita, T. Mizuno, M. Ataka, and H. Toshiyoshi, "A 2-axis MEMS scanner for the landing laser radar of the space explorer," in *2010 International Conference on Optical MEMS and Nanophotonics*, 2010, pp. 111-112.

[29] I. Aoyagi *et al.*, "2-axis MEMS scanner for a laser range finder," in *Optical MEMS and Nanophotonics (OMN), 2011 International Conference on*, 2011, pp. 39-40.

[30] U. Hofmann and J. Janes, "MEMS Mirror for Low Cost Laser Scanners," in *Advanced Microsystems for Automotive Applications 2011: Smart Systems for Electric, Safe and Networked Mobility*, G. Meyer and J. Valldorf, Eds. Berlin, Heidelberg: Springer Berlin Heidelberg, 2011, pp. 159-165.

[31] Q. A. A. Tanguy *et al.*, "A 2-axis electrothermal MEMS micro-scanner with torsional beam," in *2016 International Conference on Optical MEMS and Nanophotonics (OMN)*, 2016, pp. 1-2.

[32] C. Muyu, Y. Huijun, G. Shuai, X. Run, and S. Wenjiang, "An electromagnetically-driven MEMS micromirror for laser projection," in *10th IEEE International Conference on Nano/Micro Engineered and Molecular Systems*, 2015, pp. 605-607.

[33] N. Quack, J. B. Chou, and M. C. Wu, "Self-aligned VCSEL-microlens scanner with large scan range," in *Micro Electro Mechanical Systems (MEMS), 2012 IEEE 25th International Conference on*, 2012, pp. 656-659.

[34] U. Hofmann *et al.*, "Wafer-level vacuum packaged resonant micro-scanning mirrors for compact laser projection displays," 2008, vol. 6887, pp. 688706-688706-15.

[35] A. Torrents, K. Azgin, S. W. Godfrey, E. S. Topalli, T. Akin, and L. Valdevit, "MEMS resonant load cells for micro-mechanical test frames:

feasibility study and optimal design," *Journal of Micromechanics and Microengineering,* vol. 20, no. 12, p. 125004, 2010.

[36] W. E. Langlois, "ISOTHERMAL SQUEEZE FILMS," *Quarterly of Applied Mathematics,* vol. 20, no. 2, pp. 131-150, 1962.

[37] J. J. Blech, "On Isothermal Squeeze Films," *Journal of Lubrication Technology,* vol. 105, no. 4, pp. 615-620, 1983.

[38] S. Vemuri, "Behavioral Modeling of Viscous Damping in MEMS," MSc, Electrical & Computer Engineering, Carnegie Mellon, 2000.

[39] F. Han, Q. Wu, R. Zhang, and J. Dong, "Capacitive Sensor Interface for an Electrostatically Levitated Micromotor," *IEEE Transactions on Instrumentation and Measurement,* vol. 58, no. 10, pp. 3519-3526, 2009.

[40] J. C. Dixon, *The Shock Absorber Handbook*. John Wiley & Sons, 2007.

[41] C. L. P. R. D. Harbor, *Feedback Control Design*, 3 ed. Englewood Cliffs, NJ, USA: Prentice-Hall, 1996.

[42] E. Tatar, "Qadrature Error Compensation and Its Effects on the Performance of Fully Decoupled MEMS Gyroscopes," MSc, Electrical and Electronics Engineering, METU, Ankara, 2010.

[43] Texas Instruments LF353 Datasheet, Wide-Bandwidth JFET-Input Dual Operational Amplifier [Online]. Available: http://www.analog.com/media/en/technical-documentation/data-sheets/AD620.pdf

[44] W. Jung, *Op Amp Applications Handbook*. USA: Elsevier, 2005.

[45] Analog Devices AD620 Datasheet, Low Cost Low Power Instrumentational Amplifier [Online]. Available: http://www.analog.com/media/en/technical-documentation/data-sheets/AD620.pdf

[46] A. M. Niknejad, "Integrated Circuits for Communication, Lecture 11: Electrical Noise," ed, 2005.